

**NOVEL PROPERTIES AND EMERGENT  
COLLECTIVE PHENOMENA OF ACTIVE FLUIDS**

**A DISSERTATION  
SUBMITTED TO THE FACULTY OF THE GRADUATE SCHOOL  
OF THE UNIVERSITY OF MINNESOTA  
BY**

**ZHENGYANG LIU**

**IN PARTIAL FULFILLMENT OF THE REQUIREMENTS  
FOR THE DEGREE OF  
DOCTOR OF PHILOSOPHY**

**ADVISOR: XIANG CHENG, PH.D.**

**DEC, 2020**

© ZHENGYANG LIU 2020

ALL RIGHTS RESERVED

# Acknowledgements

I thank my advisor Prof. Xiang Cheng for the support and the guidance in the long journey of my PhD study.

I would also like to thank Prof. Chris Macosko, Prof. Daniel Blair, Prof. Sriram Ramaswamy, Prof. Gwynn Elfring, Prof. John Parkinson, Prof. Simon Rogers for their insightful discussions and encouragement. I am also grateful to Prof. Andrew Ng, from whom I have gained passion for research and life, even though I have never interacted with him in person.

My sincere thanks also go to my fellow labmates: Dr. Xiaolei Ma, Dr. Bo Zhang, Dr. Yi Peng, Dr. Jilong Wang, Dr. Shuo Guo, Dr. Kyle Welch, Dr. Leonardo Gordillo, Dr. Seunghwan Shin, Dr. Wei Zeng, Dr. Yi-Shu Tai, Dr. Maria McClintock, Dr. Yang Xu, Dr. Devranjan Samanta, Dr. Lian Bai, Dr. Truong Pham, Ou Yang, Ting-qi Sun, Yangming Kou, Yiming Qiao, Qiuge Zhang and Yuxiao Wu, for the best memories we have had in these years. I also thank three undergraduates who worked with me: Tianyi Lin, Zimu Ma and Sunyoung Hong.

I thank the NSF (Grant No. CBET-1702352 and CBET-2028652), DARPA (Grant No. YFA-D16AP00120) and the Packard Foundation for the financial support.

# **Dedication**

To my beloved family for supporting me over the years.

## Abstract

An active fluid denotes a suspension of particles, cells and macromolecules that are capable of transducing free energy into systematic motions. Converting energy at individual constituent scales, these systems are constantly driven out of equilibrium and display unusual phenomena, including a transition to a zero viscosity superfluid-like state and a transition to a collective moving turbulent state. These curious transitions are consequences of the self-propulsion of active particles, and are absent in classical complex fluids without spontaneous motions.

In this thesis, we present an experimental investigation on the rheology of active fluids under confinement. Specifically, we find the viscosity of bacterial suspensions is significantly reduced by confining walls. We show that this effect results from upstream swimming bacteria near the confining walls, which collectively exert stress on the fluids and push the fluids to flow. A phenomenological model is proposed which qualitatively captures the confinement effect on the viscosity of bacterial suspensions.

The collective motions in dense bacterial suspensions are investigated. In particular, we measure the critical conditions of the transition from disordered state to turbulent state in bacterial suspensions. We present the experimental results in a phase diagram, serving as a benchmark for existing and future theories. We put forward a heuristic model based on two-body hydrodynamic interactions, hoping to understand the transition in a more intuitive way and to stimulate theoretical advancement.

In addition, we present the first experimental study on the giant number fluctuation—a landmark of collectively moving active particles—in 3-dimensional bacterial suspensions. Our measurements are free from effect of frictional walls and thus allow quantitative comparison with previous theoretical and computational works. We also present

a detailed analysis on the flow fields generated by the swimming bacteria, and reveal a strong coupling between flow strength and giant number fluctuations spanning all length scales.

By elucidating the causes and consequences these phenomena, we not only expand the knowledge of active fluids, but also provide deeper understandings on the biological and ecological significance of living organism behavior. Our experiments deepen understanding of the self-organization processes in active fluids and lay the foundation of engineering machines composed of active constituents which mimics the properties of real living matter.

# Contents

<b>Acknowledgements</b>	<b>i</b>
<b>Dedication</b>	<b>ii</b>
<b>Abstract</b>	<b>iii</b>
<b>List of Tables</b>	<b>x</b>
<b>List of Figures</b>	<b>xi</b>
<b>1 Introduction</b>	<b>1</b>
1.1 Active Matter and Active Fluids . . . . .	2
1.2 Novel Properties . . . . .	4
1.2.1 Rheology . . . . .	5
1.2.2 Diffusion . . . . .	9
1.3 Collective Motion and Giant Number Fluctuations . . . . .	12
1.3.1 Collective Motion . . . . .	12
1.3.2 Giant Number Fluctuations . . . . .	16
<b>2 Experimental Background</b>	<b>22</b>
2.1 Motile Bacteria Sample Preparation . . . . .	23

2.1.1	Background Information . . . . .	24
2.1.2	Protocol . . . . .	24
2.2	Optical Microscopy . . . . .	29
2.2.1	Power <i>E. coli</i> with Illumination Light . . . . .	29
2.2.2	Adding Filters to Avoid Overexposure . . . . .	32
2.3	Image Analysis . . . . .	33
2.3.1	Anisotropic Particle Tracking . . . . .	33
2.3.2	Particle Image Velocimetry . . . . .	34
2.3.3	Spatial and Temporal Correlation Functions . . . . .	37
2.3.4	Energy Spectrum Calculation . . . . .	39
2.3.5	Other Image Analysis Tools . . . . .	40
2.4	Micro-fabrication and Microfluidic Viscometer . . . . .	40
2.4.1	Micro-fabrication . . . . .	40
2.4.2	Microfluidic Viscometer . . . . .	42
2.5	Light-controlled <i>E. coli</i> : Genetic Modification and Culturing . . . . .	43
<b>3</b>	<b>Rheology under Confinement</b>	<b>46</b>
3.1	Introduction . . . . .	46
3.2	Methods . . . . .	49
3.2.1	<i>E. coli</i> Suspensions . . . . .	49
3.2.2	Microfluidic Viscometer . . . . .	52
3.2.3	Image Acquisition and Analysis . . . . .	53
3.3	Results . . . . .	54
3.3.1	Confinement Effect . . . . .	54
3.3.2	Microscopic Dynamics . . . . .	57
3.4	Discussion and Conclusion . . . . .	62
3.4.1	Data Analysis . . . . .	62

3.4.2	Effect of Active Hydrodynamic and Diffusive Stresses . . . . .	65
3.4.3	Effect of Upstream Swimming Bacteria near Boundaries . . . . .	67
<b>4</b>	<b>The Emergence of Active Turbulence</b>	<b>73</b>
4.1	Introduction . . . . .	73
4.2	Methods . . . . .	78
4.2.1	Bacteria . . . . .	78
4.2.2	Sample Preparation and Video Microscopy . . . . .	79
4.2.3	Image Processing and Data Analysis . . . . .	81
4.3	Results . . . . .	82
4.3.1	Transition to Bacterial Turbulence . . . . .	83
4.3.2	3D Phase Diagram . . . . .	85
4.3.3	Transition Kinetics . . . . .	91
4.3.4	Microscopic View . . . . .	98
4.4	Discussion and Conclusion . . . . .	99
<b>5</b>	<b>Giant Number Fluctuations in 3-Dimensional Space</b>	<b>102</b>
5.1	Introduction . . . . .	102
5.2	Methods . . . . .	104
5.2.1	Sample Preparation, Imaging and Analysis . . . . .	104
5.2.2	The Relation between Pixel Intensity and Concentration . . . . .	104
5.2.3	GNF Calculations . . . . .	107
5.2.4	Normalization of GNF at Different Volume Fractions . . . . .	109
5.2.5	Correlation of Local Density Fluctuations and Kinetic Energies .	110
5.3	Results . . . . .	111
5.3.1	Density Fluctuations . . . . .	111
5.3.2	Energy Spectra . . . . .	116

5.3.3	Density-Flow Coupling . . . . .	119
5.4	Conclusion . . . . .	126
<b>6</b>	<b>Summary and Outlook</b>	<b>128</b>
6.1	Summary . . . . .	128
6.2	Outlook . . . . .	129
<b>Bibliography</b>		<b>131</b>
<b>Appendix A.</b>	<b>Light-controlled <i>Escherichia coli</i></b>	<b>157</b>
A.1	Plasmid Construction and Transformation . . . . .	157
A.1.1	Plasmid Construction . . . . .	157
A.1.2	Extraction and Purification . . . . .	158
A.1.3	Transformation . . . . .	159
A.2	DNA Sequences . . . . .	160
A.2.1	Proteorhodopsin (PR) Sequence . . . . .	160
A.2.2	pZE-PR Plasmid Sequence . . . . .	160
A.2.3	An Illustration of the pZE-PR Plasmid Structure . . . . .	163
<b>Appendix B.</b>	<b>Image Analysis Code</b>	<b>164</b>
B.1	Code Vectorization . . . . .	164
B.1.1	Vectorized Code for Spatial Correlation Function . . . . .	164
B.1.2	Non-vectorized Code for Spatial Correlation Function . . . . .	165
B.1.3	Performance Comparison . . . . .	166
B.2	Energy Spectrum Calculation . . . . .	167
B.3	Cross-Correlation Based Particle Detecting Method . . . . .	169
B.3.1	Working Principle . . . . .	170
B.3.2	Code . . . . .	170

B.4 Fourier Transform Based Orientation Analysis . . . . .	173
B.4.1 Working Principle . . . . .	173
B.4.2 Code . . . . .	174
B.4.3 Some Examples . . . . .	175
B.5 Density Fluctuation Calculations . . . . .	176

# List of Tables

1.1	$\alpha$ Values Reported by Previous Experiments. . . . .	20
2.1	Filters in the Illumination Light Path and Their Functions. . . . .	31
2.2	Strains, Plasmids and Primers . . . . .	44
A.1	PCR Recipe Using Phusion Polymerase . . . . .	158
A.2	Gibson Assembly Recipe . . . . .	158

# List of Figures

1.1	Examples of Living Matters and Active Fluids . . . . .	3
1.2	Rheology of Active Fluids . . . . .	6
1.3	Diffusion of Passive Tracers in an Active Bath . . . . .	10
1.4	Illustrations of Existing Models and Theories of Collective Motions . . . . .	13
1.5	Illustrations of Giant Number Fluctuations . . . . .	16
1.6	Experimental Realizations of Active Systems Showing Giant Number Fluctuations . . . . .	18
2.1	Model Swimmer <i>Escherichia coli</i> and Its Flow Field . . . . .	25
2.2	Graphical Motile <i>E. coli</i> Sample Preparation Protocol . . . . .	27
2.3	Nikon Ti-E Inverted Microscope and Its Filters . . . . .	30
2.4	Diffusion Filter Function Illustration . . . . .	32
2.5	Illustration of Ellipsoidal Particle Detection by Thresholding and Group Labeling . . . . .	35
2.6	PIV Working Principle Illustration . . . . .	36
2.7	Code Vectorization Illustration . . . . .	38
2.8	Microfluidic Viscometer Fabrication and Setup. . . . .	41
3.1	Microfluidic Viscometer. . . . .	50
3.2	Viscosity of Bacterial Suspensions under Different Degree of Confinement	55
3.3	Velocity Profiles of Fluid Flows and Bacteria at Different Channel Heights	59

3.4	Upstream Swimming Bacteria in a Microfluidic Viscometer . . . . .	60
3.5	Bacterial Density Distribution in Microfluidic Channels . . . . .	61
3.6	Scaling of Relative Viscosity of Bacterial Suspensions . . . . .	65
3.7	Boundary-layer Upstream Swimming Bacteria Model . . . . .	67
3.8	Compare Boundary-layer Model with Experimental Data . . . . .	69
4.1	Motility of Light-powered Bacteria . . . . .	77
4.2	Bacterial Turbulence . . . . .	82
4.3	The Velocity Correlation Length . . . . .	84
4.4	Transition to Bacterial Turbulence and the Phase Diagram of 3D Bacterial Flows . . . . .	86
4.5	Effect of Immobile Bacteria . . . . .	90
4.6	Transition Kinetics . . . . .	92
4.7	One-step and Two-step Transitions . . . . .	94
4.8	Energy Spectra through the Bacterial Turbulent Transition . . . . .	95
4.9	Microscopic View of the Turbulent Transition Deep Inside the Turbulent Phase . . . . .	97
5.1	Images of Bacterial Active Turbulence and Its Flow Fields . . . . .	105
5.2	Relation between Image Intensity and Concentration . . . . .	106
5.3	GNF Calculations . . . . .	107
5.4	Normalization of GNF at Different Volume Fractions . . . . .	110
5.5	Local Correlation between Density Fluctuations and Kinetic Energies .	112
5.6	Spatial and Temporal Correlation Functions in Active Turbulence . . .	114
5.7	Giant Number Fluctuations in Active Turbulence . . . . .	115
5.8	Energy Spectra in Active Turbulence . . . . .	117
5.9	The Coupling between GNF and Kinetic Energy Spectra . . . . .	120

5.10 Temporal Evolution of $\alpha$ , Flow Kinetic Energy $\langle \mathbf{v}^2 \rangle / 2$ and Fraction of Aligned Flow Region $M$ . . . . .	123
5.11 Evolution of GNF and Energy Spectra during the Turbulent Transition . . . . .	124
5.12 Density Flow Coupling during the Transition towards Active Turbulence . . . . .	125
A.1 An illustration of pZE-PR plasmid . . . . .	163
B.1 The Performance of Vectorized and Non-vectorized Code . . . . .	166
B.2 Cross-correlation Based Particle Detecting Method . . . . .	169
B.3 Fourier Transform Based Orientation Analysis Illustration . . . . .	173
B.4 Fourier Transform Based Orientation Analysis Examples . . . . .	176

# Chapter 1

## Introduction

- Chapter 1 briefly describes the history and significance of active fluid research.
- Chapter 2 presents the experimental techniques used in this thesis.
- Chapter 3 talks about one of the emergent properties: reduced viscosity. Portions of this chapter have been published in [1].
- Chapter 4 presents the study on the transition from disordered state to active turbulence in light-powered bacterial suspensions. This work is conducted with a close collaboration with Yi Peng and Xiang Cheng. Large portions of this chapter have been published in [2]. Yi Peng, Zhengyang Liu and Xiang Cheng conceived the experiment. Zhengyang Liu constructed the light-powered bacteria. Yi Peng performed the experiment. Zhengyang Liu and Yi Peng did the data analysis. All authors contribute to the model development and writing of the manuscript.
- Chapter 5 talks about another emergent property: giant number fluctuation. Portions of this chapter have been published in [3].
- Chapter 6 summarizes the contributions of this thesis and provides the outlook

on future research.

- Appendix A shows details of the construction of light-powered *Escherichia coli* (*E. coli*).
- Appendix B provides details of several particle tracking tools I developed.
- Appendix C shows details of photolithography.

## 1.1 Active Matter and Active Fluids

Active matter denotes a large group of active units which utilize ambient energy to achieve motions. Examples include flocking birds, schooling fish, herding beasts and even human crowds, down to actin filaments powered by motor proteins, bacteria and chemical reaction driven particles [4–10]. The concept roots from a broader class of matter: soft matter, which includes polymers, surfactants and colloidal grains and shares common properties such as complexity and flexibility [11]. Like soft matter, active matter is also complex due to the interactions between large numbers of constituents. What makes them more complex is the self-propulsion of each individual constituent, which endows them with more intriguing and counter-intuitive properties, challenging our understandings [12].

Active fluids, sometimes referred to as active gels, are suspensions of active agents such as cells, particles and biological macromolecules that are capable of utilizing chemical energy to sustain their self-propulsion. They are a subset of active matter, and the "fluids" in the name suggests the important role of the viscous hydrodynamic interaction and stress, in contrast to dry active matter [7]. The first glimmering of active fluids dates back to 1969, when Finlayson and Scriven found that motion could spontaneously set in a previously still material without the intervention of outside forces,

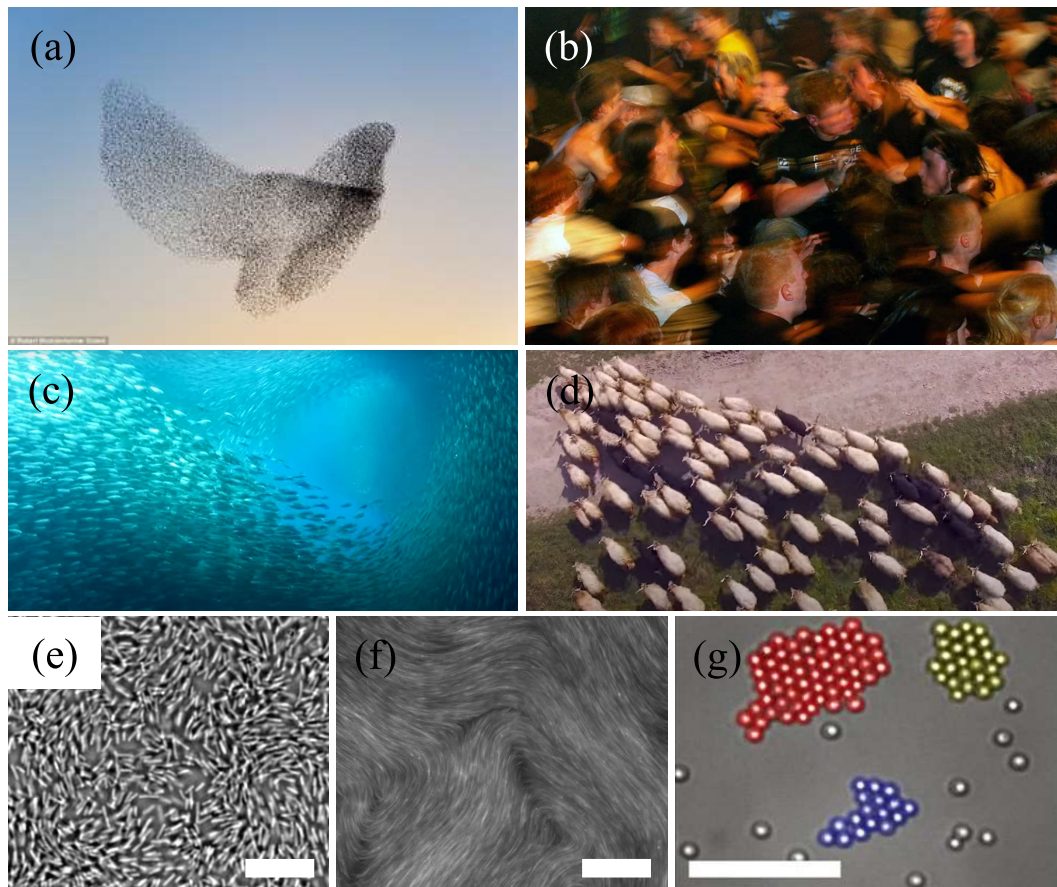


**Figure 1.1: Examples of living matters and active fluids.** (a) Flocking birds, (b) people in a mosh pit at heavy metal converts, (c) schooling fish, (d) herding sheep, (e) swarming bacteria (f) microtubule and (g) clustering active Janus particles. Scalebars in (e) and (g) are  $10 \mu\text{m}$ . Scalebar in (f) is  $200 \mu\text{m}$ . Images courtesy of Robert Wolstenhome (a), biographic (c, d). (b) is reprinted from Ref. [13] with permission from the American Physical Society. (f) is reprinted from Ref. [14] with permission from Springer Nature. (g) is reprinted from Ref. [15] with permission from the American Association for the Advancement of Science.

due to composition-dependent stress [16]. However, the study on active fluids did not bloom, until 26 year later, when the seminal paper on modeling collective flocks came out [17]. From then on, physicists are getting unprecedentedly interested in biological phenomena, leading to the emergence of a new field of study - active fluids.

Early accomplishments in the research of active fluids include two successful theoretical predictions on the abnormal rheology and the spontaneous active turbulence [18,19], which were then demonstrated in quite a few experiments [20–25]. From these beginnings, the field has been enjoying a vibrant interplay between experiment and theory, and more complex environment and geometrical constraints have been investigated [26]. As of now, the study of active fluids has provided us with a good qualitative understanding of some biological processes, such as how active turbulence enhances nutrient transport.

There are two promising directions in active fluids. One is to get quantitative understanding of the novel properties. These works will not only provide more accurate predictions on new systems, but also guide the engineering of artificial robots that can perform tasks in complex environment, such as drug delivery. Another direction is to invite chemistry and biology to collaborate on this highly interdisciplinary subject. A complete understanding of the behavior and properties of living systems will require the knowledge of biochemical signaling, which opens the door of an ambitious mission: elucidating tissue dynamics and developmental biology [7,27]. The works that are to be described in Sec. 3, 4 and 5 are along the first direction: seeking more quantitative understanding of rheology and active turbulence of active fluids.

## 1.2 Novel Properties

Active fluids exhibit novel properties such as reduced viscosity and enhanced diffusion [5]. The reduced viscosity is induced by the force exerted by the swimming mechanisms

of the active agents, such as bacteria and algae [28]. And the enhanced diffusion is attributed to the interaction - steric collision or hydrodynamic perturbation - between tracer particles and swimmers [29–37]. In this section, the existing works regarding rheology and diffusion in active fluids are reviewed, and motivations for investigating the rheology of bacterial suspensions under confinement (Chap. 3) will be discussed.

### 1.2.1 Rheology

Viscosity of a fluid can be understood as its resistance to flow. When flowing, fluid elements move relative to others, resulting in energy dissipation due to friction. The more energy is required, the more “viscous” the fluid is known to be. A suspension of passive particles is always more viscous than its suspending fluid, a fact that was first formulated by Einstein in 1906 [40]. Recently, the study of active fluids revealed that active particles modify the viscosity of their suspending fluids in a different and interesting way.

In 2004, Hatwalne et al. predicted that micro-swimmers, depending on their self-propelling mechanisms, can modify the suspension viscosity in different ways [18]. Most common micro-swimmers, such as unicellular microorganisms, can be classified into two types: pushers and pullers, based on the far field flow they generate. Figure 1.2b illustrates the most common pushers and pullers in nature: bacterium and algae. If one puts an elongated rod-like bacterium in a simple shear flow, as illustrated in Fig. 1.2a, the preferred orientation of the bacterium is along the extensile flow [41]. Such an orientation makes the flow generated by the swimming bacterium coincide with the imposed shear flow, and thus compensating the viscous dissipation of energy, which effectively reduces the viscosity. In contrast, in the case of puller swimmers, such an orientation opposes the directions of swimming induced flow and imposed shear flow, which enhances the viscosity.

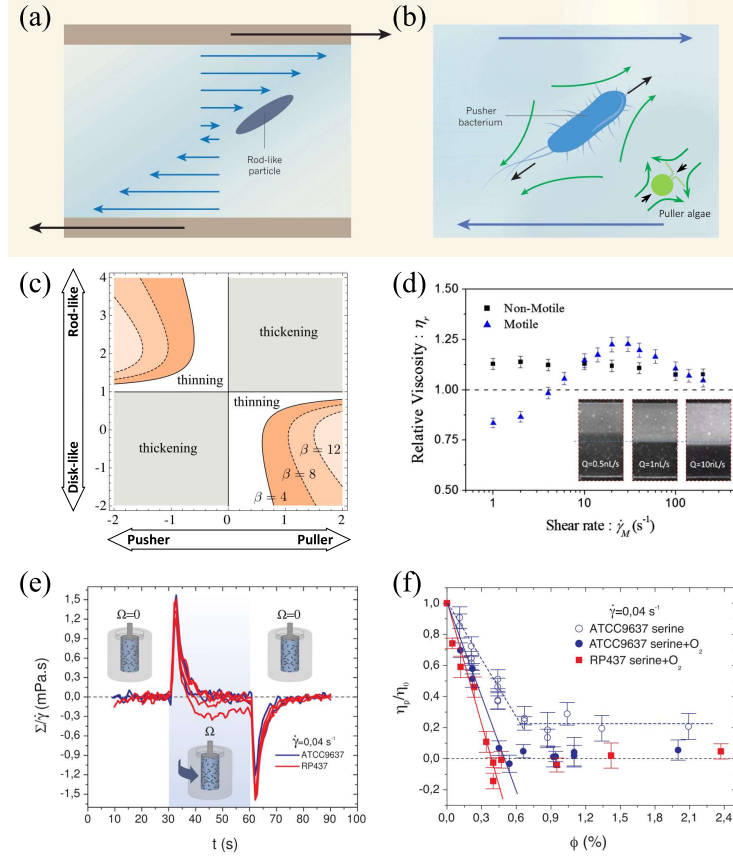


**Figure 1.2: Rheology of active fluids.** (a) The preferred orientation of the bacterium is along the extensile flow. (b) The most common pushers and pullers in nature: bacterium and algae, and their corresponding far field flow. (c) Rheological effect phase diagram of swimmer shape and swimming mechanism. (d) Non-Newtonian behavior of *E. coli* suspensions. (e) Stress response of *E. coli* suspensions in a modified Couette concentric cylinder rheometer. (f) Viscosity of *E. coli* suspensions at various volume fractions. (a) and (b) are reprinted from Ref. [38] with permission from Springer Nature. (c) is reprinted from Ref. [39] with permission from the American Physical Society. (d) is reprinted from Ref. [24] with permission from the American Physical Society. (e) and (f) are reprinted from Ref. [25] with permission from the American Physical Society.

Their prediction was confirmed by numerical solutions of the theory [39, 42] and experiments [23–25]. Cates et al. reached at the same conclusions as Hatwalne et al. did: while contractile gels exhibit a divergence of apparent viscosity, extensile gels show a zero-viscosity phase. Giomi et al., on top of these results, emphasized the important role of particle shape. They showed, in their numerical study, an rheological equivalence between rod-like pusher swimmers and disk-like puller swimmers (see Fig. 1.2c). In particular, they predicted a thickening effect of spherical puller swimmers (corresponds to the 0 shape parameter in Fig. 1.2c). This prediction was later on challenged by another theory in the framework of swim stress, which predicts a viscosity reduction of a spherical pusher swimmer suspension [43]. Due to the difficulty of synthesizing large amounts of artificial swimmers, this debate has not been resolved yet. However, with the rapid development of synthesizing techniques [15, 44], it is getting more promising that we will resolve it, and formulate a more complete understanding on how active swimmers modify the rheology.

Experimental confirmation of these predictions posed challenges on traditional rheometries due to the tiny shear stress that is required to be measured. As a result, new rheometries are needed [38]. In 2009, Sokolov and Aranson came up with an innovative way of measuring the such tiny stress [23]. By moving a probe in a suspension of *Bacillus subtilis* bacteria, a pusher type swimmer, they generated a large vortex. By studying the decay of the vortex, they got a measure of the viscosity. For the first time, they experimentally confirmed that pusher swimmers reduced the viscosity (see their results in Fig. 1.2d). In 2013, Gachelin et al. adopted a microfluidic viscometer to measure the viscosity of suspensions of *E. coli* bacteria, another pusher type swimmer [24]. They confirmed again the viscosity reduction. A more remarkable finding is the non-Newtonian behavior: the viscosity was reduced at low shear rate, but was

enhanced at high shear rate. This observation suggested that it is the competition between bacterium intrinsic shear rate and the imposed flow shear rate that determines how the viscosity is modified. In 2015, Lopez et al. published arguably the most important experimental work on the rheology of active fluids, which showed that the apparent viscosity of an *E. coli* suspension can be reduced to zero if the swimming activity is sufficiently high [25]. The authors modified an old-fashioned Couette concentric cylinders, where the outer cylinder was set to rotate at a fixed rate and the torque on the inner cylinder was measured. The high sensitivity was achieved by using a string that was highly sensitive to torque to hang the inner cylinder, so that a stress, as small as that generated by bacterial suspensions, can be detected (see their rheometer and results in Fig. 1.2e-f). The authors termed their zero-viscosity suspensions “superfluids”.

Despite the great progress on the rheology of active fluids made so far, there remains complexity that is not readily understood. Confinement, or more generally boundary conditions or geometry, is one of the leading factors that contributes to this complexity. The behavior of active particles can be altered greatly by confinement. In 2005, Voituriez et al. showed theoretically that a spontaneous flow transition from a homogeneous immobile state could happen in active polar gel under confinement [45]. Such spontaneous flow transition was confirmed in both numerical and experimental studies [46–48]. The complexity introduced by geometry was also manifested by the experiments where a single bacterial vortex was stabilized by confinement [49–51] and where asymmetric gears were powered by swimming bacteria [52, 53]. The effect of confinement on the rheology of active fluids was first studied theoretically based on the kinetic theory [54] and a generalized Navier-Stokes model [55]. In this thesis, I will present the first experimental study on active fluid rheology using bacterial suspensions (Chap. 3). The fact that our experimental results agreed with neither theory manifested the complexity and the lack of understanding of active fluids. Together with the experimental results, we

provided a heuristic model that qualitatively captured the rheological properties and hope to stimulate further theoretical studies on this matter.

### 1.2.2 Diffusion

The diffusion of passive particles in active fluids, such as nutrients and signaling molecules, are significantly enhanced. Such enhancement has been shown to have great biological and ecological importance [29,32,37], as well as to provide a useful tool of probing novel properties of active fluids [57]. Unlike the study of rheology, which was initiated by theoretical prediction, the study of enhanced diffusion started from an experiment.

In 2000, Wu and Libchaber studied the diffusion of spherical polystyrene particles in a bath of actively swimming *E. coli* [29] (see Fig. 1.3a for their experimental system). They characterized the diffusion of the tracer particles by measuring their means squared displacement (MSD) (see Fig. 1.3b for typical MSD data), and reported two findings: 1) the MSD exhibits a superdiffusive regime at short time, which is followed by a diffusive regime at longer time; 2) the effective temperature, backed up from effective diffusion coefficient using Stokes-Einstein equation, is several order of magnitude larger than room temperature. Their qualitative findings were confirmed by computational [58,59], theoretical [60] and other experimental studies [33,34,37,61,62]. A remarkable progress towards quantitative understanding was made by Mino et al., who experimentally identified that the enhancement of diffusivity is proportional to the “activity flux” (defined as concentration multiplied by the mean velocity of swimmers). This model was further developed to capture the experimental result more accurately and to account for more complex conditions [32,63,64].

Although a lot of progress has been made on understanding diffusion isotropic particles (spheres) in an active bath, how anisotropic particles diffuse remained largely

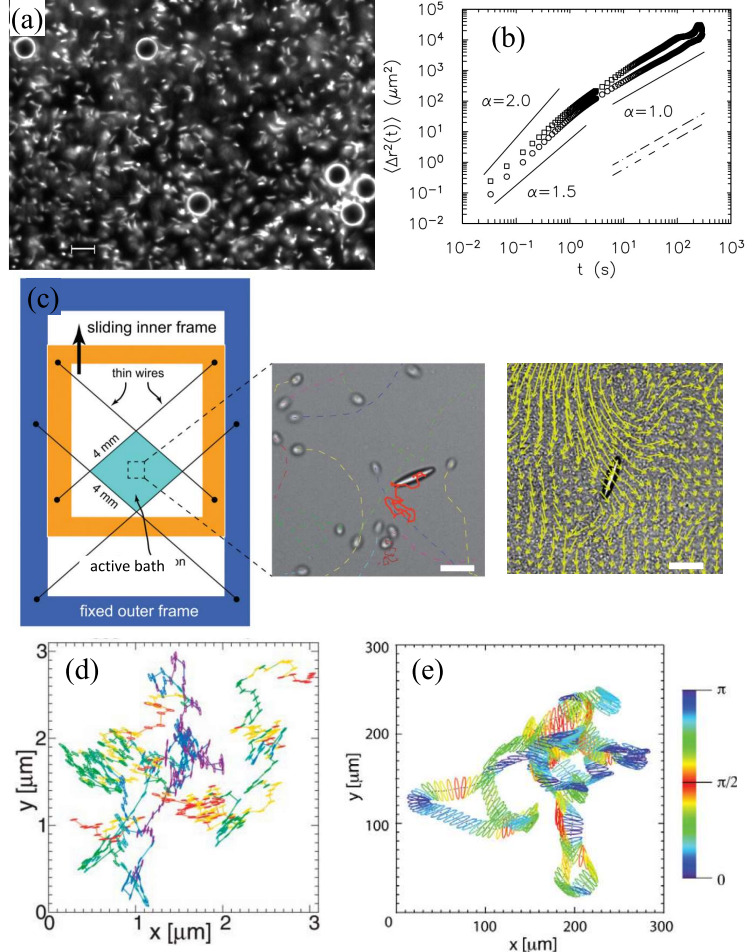


**Figure 1.3: Diffusion of passive tracers in an active bath.** (a)  $10 \mu\text{m}$  diameter PS particles suspended in a bath of *E. coli*. (b) Mean squared displacement (MSD) of tracer particles as a function of lag time. (c) Free-standing film setup adopted by Peng et al. and Yang et al. (left) [30, 35]. A microscopic image of ellipsoidal PS particle suspending in *C. reinhardtii* (middle) and *E. coli* (right) baths. Scale bar:  $20 \mu\text{m}$ . (d) and (e) present both the translational and orientational trajectories of ellipsoids diffusion in water and *E. coli* bath, respectively. (a) and (b) are reprinted from Ref. [29] with permission from the American Physical Society. (c) is reprinted from Ref. [35] with permission from the American Physical Society. (d) is reprinted from Ref. [56] with permission from the American Association for the Advancement of Science. (e) is reprinted from Ref. [30] with permission from the American Physical Society.

unexplored. Yet, the diffusion of anisotropic particles has both fundamental and practical significance. On the one hand, it was shown that the Brownian motion (i.e. in a passive bath) of anisotropic particles exhibited a subtle interplay between orientational and translational motions [56]. Previous studies preferred to consider an active bath equivalent to a high temperature passive bath [29], and it was shown to be a good equivalence for isotropic particles. A fundamentally interesting question to ask is: does active bath also alters the interplay between orientational and translational motions? The answer is yes, and we will see that this interplay is specific to swimming mechanisms. On the other hand, few particles or molecules in nature are perfectly isotropic. Generalizing the enhanced diffusion to anisotropic particles will have significant impact on applying this knowledge to real world problems. In 2016, Peng et al. studied the diffusion of polystyrene ellipsoids in a quasi-2D free-standing soap film of *E. coli* bath (see setup schematic in Fig. 1.3c) [30]. In contrast to the pure Brownian motion, where ellipsoids preferred to diffuse along their major axes [56], they found that an active bath forced the ellipsoids to move primarily along the minor axes (see Fig. 1.3d-e for a comparison). This phenomenon was explained by considering the far-field dipole flow of a single *E. coli* bacterium. An interesting prediction naturally arises: in a bath of puller swimmers, whose far-field flow is opposite to that of pushers, the diffusion of ellipsoidal tracers should be primarily along the major axes. This prediction was later on proved experimentally by Yang et al. [35] in a green algae *C. reinhardtii* bath and I was involved in this work. Due to the fact that my contribution was relatively small to this work, I will not provide more details about it in my thesis. However, readers interested are encouraged to find out more in our original paper [35].

## 1.3 Collective Motion and Giant Number Fluctuations

Collective motion is defined as an emergent directed movement in a large number of animals or particles, which are capable of moving on their own. In the seminal paper by Reynolds published in 1987, he tried to use a simulation approach, rather than scripting the paths beforehand, to generate vivid motions of animals in computer graphics [65]. This idea has soon evoked enormous research interest of physicists because a seemingly universal animal behavior was found in animals across different length scales: up to large animals as birds and fish, and down to small insects and micro organisms.

In this section, we first review recent progresses on understanding the collective motions in various living and non-living systems. Our research on “imaging the emergence of active turbulence” will be motivated (detailed in Chap. 4). Then, I will describe an important consequence of the collective phenomena: giant number fluctuations (GNF), which is regarded as a landmark phenomenon of collectively moving particles. I will motivate our research on “giant number fluctuations in 3-dimensional bacterial suspensions” in this section, and the details of this research will be shown in Chap. 5.

### 1.3.1 Collective Motion

The research on collective motion dates back to the 1980s, when flocking birds, schooling fish, herding beasts and even human crowds (Fig. 1.1a-d) were regarded as an orientationally ordered phase of living matter, in analogy with ferromagnetic spins [13, 17, 65, 67–69]. Besides macroscopic systems mentioned above, smaller and more laboratory accessible model systems have joined this family and have been studied extensively. As examples, actin filaments and bacteria exhibit turbulence-like swirling patterns, and synthetic active colloids form dynamic clusters (Fig. 1.1e-g) [15, 21, 70–74].

While being fascinated by the patterns formed by collectively moving animals or particles, researchers are trying to come up with rules, models and theories to explain

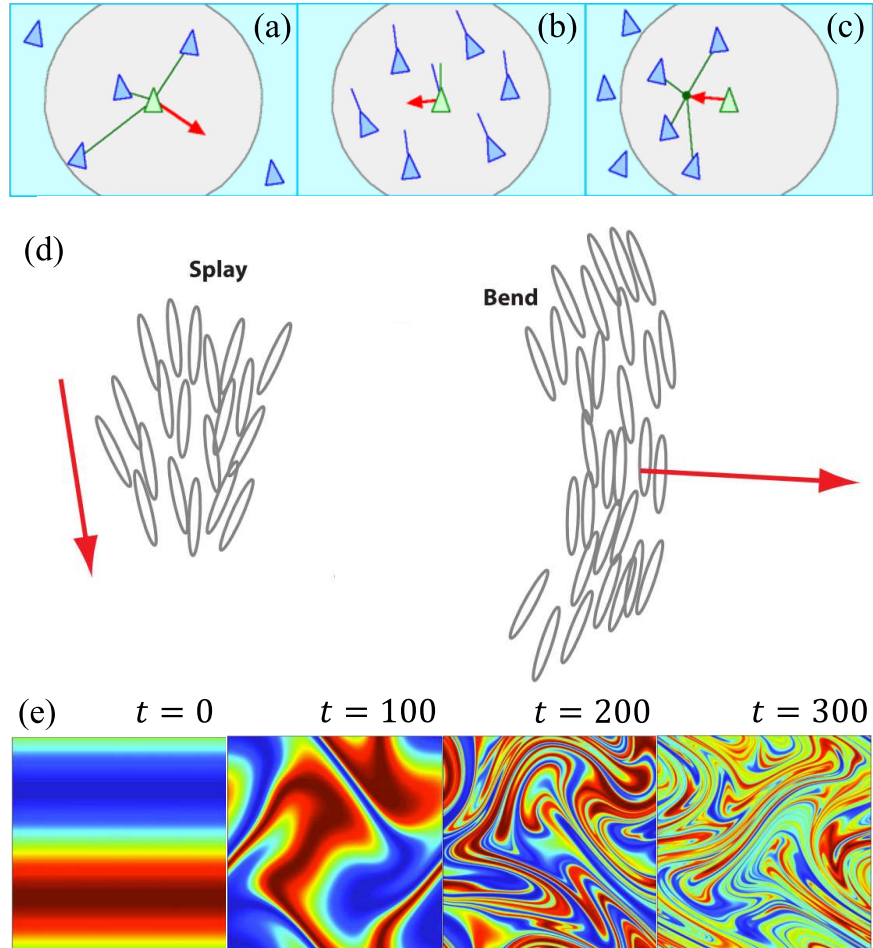


**Figure 1.4: Illustrations of existing models and theories of collective motions.** (a)-(c) Reynolds' “boids” model obeying the rules of separation (a), alignment (b) and cohesion (c). (d) Nematic self-propelled particle model, displaying splay (left) and bend (right) instability. (e) Simulation of efficient fluid mixing driven by active pusher swimmers. (a), (b) and (c) are reproduced from Ref. [65]. (d) is reprinted from Ref. [5] with permission from the Annual Reviews, Inc.. (e) is reprinted from Ref. [66] with permission from AIP Publishing.

and predict this process. There is a vast literature trying to understand collective motions in different systems from various approaches. To get an idea of how extensively it has been studied, Ref [65] by Reynolds has been cited more than 10,000 times so far. I will briefly review the attempts to model collective motion, which are most relevant to our research that will be detailed in the following chapters. A more comprehensive review on the studies of collective motions can be found in the review paper by Vicsek [6]. In 1987, Reynolds came up with arguably the first set of rules to capture the features of collective motions, based on a simple self-propelled particle model. Three rules were set into the system: separation, alignment and cohesion, as illustrated in Fig. 1.4a-c, where the blue and green triangles are the actively moving particles in his simulation, called “boids” [65]. In 1995, Vicsek modified Reynolds’ model by replacing the separation and cohesion rule with a random perturbation in the velocity of each particle, while keeping the alignment rule, which dictates one particle to always point to the same direction as its neighbors [17]. Due to the simpler and more robust rules compared to Reynolds’ model, Vicsek’s model was able to simulate huge flocks. In later studies, the Vicsek Model has become a standard model where properties of collective motions are explored [75–79]. Despite the success of discrete and finite system simulation in understanding 2D collective motions, it was challenging to study long range, long time and higher dimensional dynamics using such approach. In 1995, Toner and Tu wrote down a continuum equation of motion for a “large universality class of models” such as the Vicsek Model based on symmetry and conservation arguments [80]. In 2002, Simha and Ramaswamy made the first attempt to address hydrodynamic effect in self-propelled particle suspensions [19]. Within the framework of liquid crystal physics, they formulated an equation of motion with hydrodynamic terms to account for the “flow-alignment” effect [41]. The inclusion of hydrodynamic effects turned out to be very important, because it directly accounted for phenomena in bacterial suspensions,

the largest group of prokaryotic organisms and the most studied model active system. Their theory captures several aspects of bacterial suspensions well, including the emergence of active turbulence and giant number fluctuations as a consequence of the bend instability of an ordered state (illustrated in Fig. 1.4d). In 2008, Saintillan and Shelly adapted kinetic theories, which were previously used to study polymers, to study the suspensions of self-propelled particles [66,81]. Their theory generalized the predictions by Simha and Ramaswamy by predicting that, in addition to ordered state, a disordered state is also unstable and can evolve into a turbulent state. Moreover, they made interesting investigations on the nonlinear effects, such as pattern formation and efficient fluid mixing. Figure 1.4e shows one instance of their simulation on the evolution of fluid mixing driven by active pusher swimmers. There are other attempts to model the collective motion and its consequences that I haven't included. For a more comprehensive review of both theoretical and experimental advances, see the review papers [5,7,82].

As of today, these universal patterns can be qualitatively reproduced by simple models with collision rules and noise. And quantitative description is developing with more observations available, which is bound to have impactful applications, including understanding the reaction of panic crowd and predicting the migration of fish schools [6].

In my research, bacterial suspensions are the model system. In such system, the collective motion is usually manifested by the emergence of “active turbulence”, where vigorously swimming bacteria are stirring the fluid and generating vortex- and jet-like patterns, reminiscent of high Reynolds number turbulence [2,20,21,23,70,74,83,84]. The onset of large scale collective motions in bacterial suspensions has been regarded as a disorder-order phase transition, where critical conditions at which the transition should happen have been predicted by various theoretical works [7,82,85,86]. In contrast to the abundance of theoretical predictions, definitive experiments that can quantitatively

verify them are still lacking [82, 86]. To fill this gap, I worked closely with my colleague Dr. Yi Peng on systematically measuring the critical conditions of this transition. The result will be presented in Chap. 4.

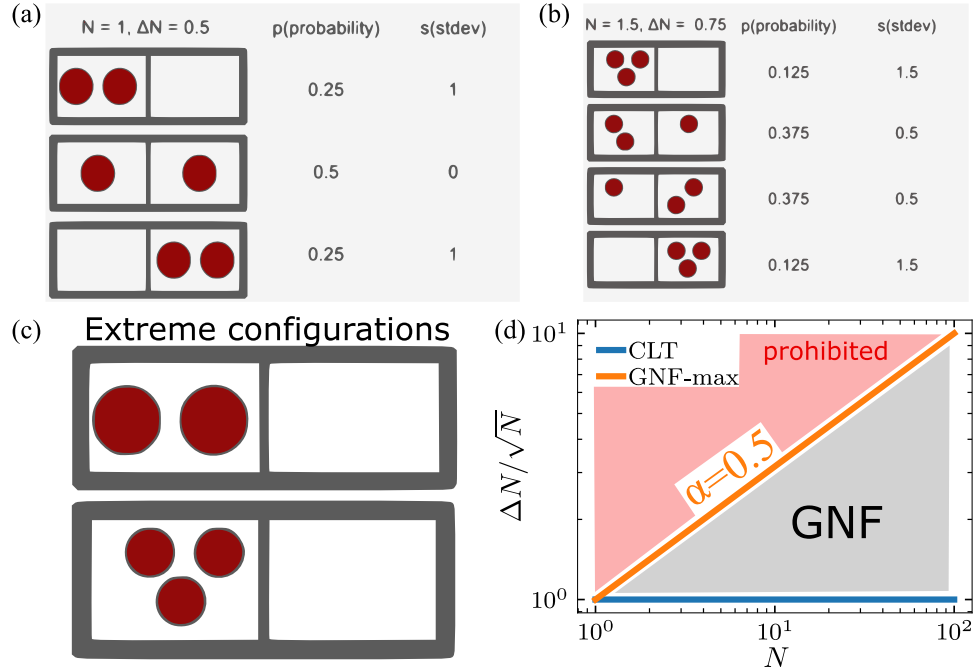


Figure 1.5: **Illustrations of giant number fluctuations.** (a) and (b) illustrate a 2-particle system and a 3-particle system, along with the probabilities and the standard deviations of each configuration. (c) The most extreme configuration of 2-particle and 3-particle systems. (d) Number fluctuation curves, where standard deviation of number of particles rescaled by the square root of mean number  $\Delta N/\sqrt{N}$  is plotted against the mean number  $N$ . The scaling exponent of these curves, denoted as  $\alpha$ , measures the magnitude of GNF.

### 1.3.2 Giant Number Fluctuations

Active particles displays transient large scale inhomogeneity even in a *statistically homogeneous and stationary state*. Such a phenomenon is referred to as *giant number fluctuations* (GNF). Formally, it is defined as the anomalously strong dependence of the

variance of the number of particles on the mean number. GNF was predicted by a number of early theoretical works [5, 19, 66, 80, 81, 87–89], and was confirmed by observations in computational models [76, 78, 79, 90–92] and experimental realizations [15, 67, 93–99]. Over the past two decades, GNF has been shown to be universal across multiple length scales and is now being regarded as a landmark of collectively moving active particle systems. Despite the many studies on this universal phenomenon, a quantitative understanding is still lacking. Specifically, the scaling exponent of the variance of the number of particles on the mean number has not been measured in a definite way. In this section, I will review the attempts that have been made to fill these gaps and motivate our research on GNF, which will be described in detail in Chap. 5.

A particle system in thermal equilibrium obeys central limit theorem, which states that when the size of a system gets very large, the fluctuation of particle number is negligible. More quantitatively, the number fluctuations represented by the standard deviation  $\Delta N$  scales with the square root mean number  $N^{0.5}$ . From a statistical mechanics point of view, the configuration of a particle system in equilibrium can be determined by randomly assigning states to each particle and find the most probable configuration. Figure 1.5a-b shows all the possible configurations of a 2-particle system and a 3-particle system, with corresponding probability of each configuration shown on the side. Each particle has only two possible states: “left” and “right”. If we keep increasing the particle number  $N$  and calculate the ensemble average of the standard deviation  $\Delta N$ , the resulting number fluctuation curve ( $\Delta N/\sqrt{N}$  vs.  $N$ ) will be a flat line, as shown by the blue line in Fig. 1.5d. This curve describes the number fluctuations in equilibrium systems.

In contrast, an active particle suspension is constantly driven out of equilibrium by the energy flux transduced by the micro-swimmers. As a result, active systems deviate from the central limit theorem, with  $\Delta N$  scales faster than  $\sqrt{N}$ . Consider the most

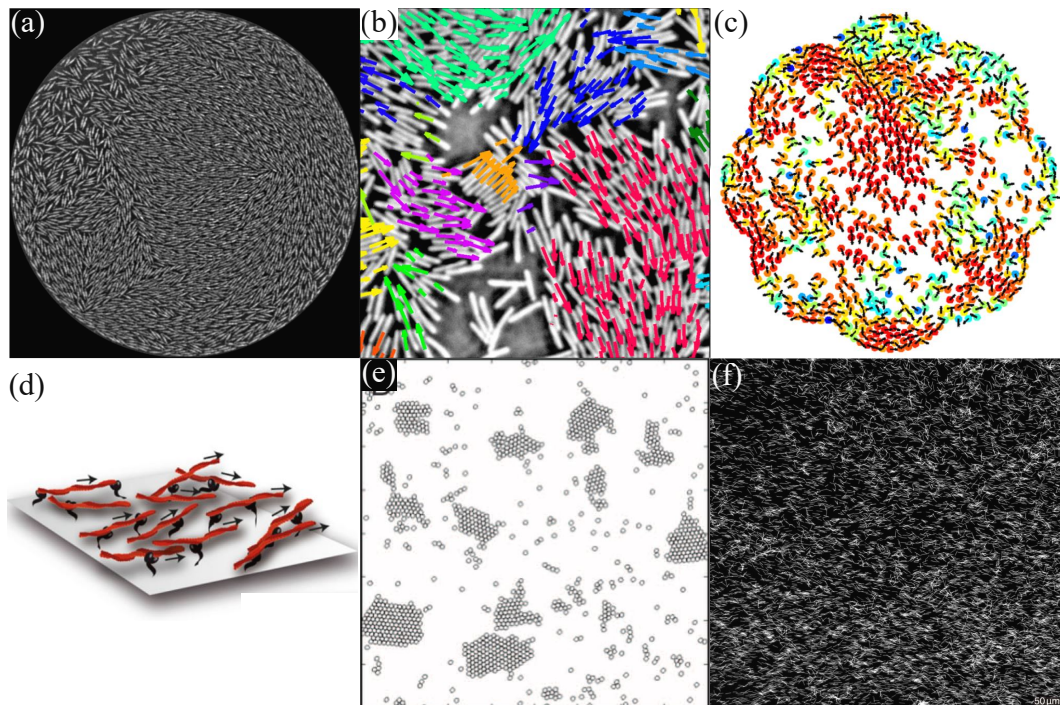


**Figure 1.6: Experimental realizations of active systems showing giant number fluctuations.** (a) Granular rods driven by a vibrating surface underneath them. (b) Swarming *B. subtilis* bacteria on semi-solid media. (c) Vibrated disks. (d) Actin filaments powered by motor proteins. (e) Janus particles powered by chemical reactions. (f) Swimming *E. coli* confined in quasi-2D glass chambers. (a) is reprinted from Ref. [67] with permission from the American Association for the Advancement of Science. (b) is reprinted from Ref. [94] with permission from the NAS. (c) is reprinted from Ref. [95] with permission from the American Physical Society. (d) is reprinted from Ref. [96] with permission from the NAS. (e) is reprinted from Ref. [15] with permission from the American Association for the Advancement of Science. (f) is reprinted from Ref. [98] with permission from the American Physical Society.

extreme case in the “left-right” system, where the probability of all particles have the same state is 1, as shown in Fig. 1.5c. If we plot the number fluctuation curve ( $\Delta N/\sqrt{N}$  vs.  $N$ ) for such a system, the curve will show a scaling exponent 0.5, as shown by the orange line in Fig. 1.5d. We define the excess scaling exponent as the measure of the magnitude of GNF, and use  $\alpha$  to denote it. In a typical active system exhibiting GNF, we have  $\Delta N \sim N^{0.5+\alpha}$  where  $0.5 \geq \alpha > 0$ , as indicated by the gray region (GNF) in Fig. 1.5d.

Many experimental attempts has been made to measure  $\alpha$ . In 2007, Narayan et al. did the first experiment focusing on GNF with shaking granular rods, which the authors termed a ”fluidized monolayer of rods” (Fig. 1.6a) [67]. The  $\alpha$  measured by them was as large as 0.5, the largest possible value of  $\alpha$ . And they also observed a much slower decay of the temporal autocorrelation of the density fluctuations, which directly confirmed the theoretical predictions made by Ramaswamy et al. [89]. Similar experiments, where macroscopic granules were driven by a vibrating surface, have also been conducted by Kudrolli et al. [100] and Deseigne et al. (Fig. 1.6c) [95]. These authors reported  $\alpha$  to be 0.16 and 0.22, respectively. Quantitative assessment of GNF in biological systems was first done in 2010 by Zhang et al. on swarming *B. subtilis* bacteria on semi-solid agar media (Fig. 1.6b) [94]. The claimed to have identified GNF in a biological system and reported the  $\alpha$  to be around 0.25. Their work was followed by more microscopic measurements, in both biological and synthetic active systems [15, 96–99]. Some of the systems studied in these works are also shown in Fig. 1.6, including actin filaments powered by motor proteins (Fig. 1.6d), Janus particles powered by chemical reactions (Fig. 1.6e) and swimming *E. coli* bacteria (Fig. 1.6f). The  $\alpha$  values reported by these works range from 0.13 to 0.5. Table. 1.1 shows all the  $\alpha$  values reported by the experiments described above.

By summarizing these experimental results, we realize that the  $\alpha$  values measured

Author	Year	Dimensionality	$\alpha$	System
Narayan et al.	2007	2-D	0.5	granular rods on vibrating surface
Kudrolli et al.	2008	2-D	0.16	granular rods on vibrating surface
Deseigne et al.	2010	2-D	0.22	granular disks on vibrating surface
Zhang et al.	2010	2-D	0.25	swarming <i>B. subtilis</i> bacteria on semi-solid agar media
Schaller et al.	2013	2-D	0.3	actin filaments powered by motor proteins
Palacci et al.	2013	2-D	0.38	Janus particles powered by chemical reactions
Kawaguchi et al.	2017	2-D	0.25	neural progenitor cells
Nishiguchi et al.	2017	2-D	0.13	swimming <i>E. coli</i> bacteria
Karani et al.	2019	2-D	0.35	Quincke particles powered by electric fields

Table 1.1:  $\alpha$  Values Reported by Previous Experiments.

from different systems show significant discrepancies. While  $\alpha$  can only take values from 0 to 0.5, the reported values have already ranged from 0.13 to 0.5, which spans almost the whole range of possible values. Although it is very encouraging to have observed a predicted phenomenon in many different systems across multiple length scales, further advancement of the understandings of this seemingly universal phenomenon relies strongly on more definite measurements. All the previous experiments were conducted in 2-dimensional systems, which were unavoidably affected by frictional walls. Therefore, we conceived a measurement of GNF in a 3-dimensional system, which is free from frictional walls and can provide a more definite value of  $\alpha$ .

Collectively moving particles form remarkable macroscopic patterns in dense suspensions in forms of complex vortices and jets. Such patterns resemble the classic high Reynolds number turbulence, and has been referred to as meso-scale turbulence

or active turbulence [21]. Due to this analogy, the quantity that has been widely used in traditional turbulence study—energy spectra—has been borrowed to investigate the flow structures of active turbulence [2, 84, 92, 101–106]. Saintillan et al. computationally studied the energy spectra of 2-dimensional suspensions of rod-like active particles at various volume fractions, and found that at large wavenumber  $k$ , all volume fraction samples showed a universal scaling exponent -4. Such universal behavior broke down at large length scales, when  $k$  is small [92]. Using a mean-field theory, Giomi obtained the energy spectra of 2-dimensional active nematics, and found that they decay with the wavenumber  $k$  as  $k^{-4}$ , inconsistency with the numerical result obtained by Saintillan et al. [102]. These results are suggesting an important distinction between the classic turbulence and active turbulence. As suggested by Bratanov et al., who investigated numerically and analytically a continuum description of active turbulence involving a cubic nonlinearity, active fluids is defining a new class of turbulent flows due to the self-organization of active particles [101]. Although this distinction has been predicted by a number of theories and simulations, a systematic measurement of energy spectra in active turbulence is lacking. Moreover, we notice that both energy spectra and GNF describe the scale-dependent properties of an active system. Such analogy indicates a connection between the two quantities. In Chap. 5, I present a systematic study on both GNF and energy spectra in active suspensions of various volume fractions. I will show that a close connection between GNF and energy spectra indeed exists, which hints the microscopic origin of GNF.

## Chapter 2

# Experimental Background

In this chapter, experimental techniques that are used in my research will be described briefly as a practical guide for those who want to test or perform some parts of the experiments in this thesis. The following aspects will be covered:

- *Escherichia coli* (*E. coli*) bacterial suspensions are the model system throughout the whole thesis, so I will start talking about the preparation of motile bacterial sample in Sec. 2.1.
- Optical microscopy along with digital imaging has been the key approach for investigating how the microscopic dynamics lead to macroscopic property difference. The standard operations of imaging equipments have been documented by the equipment manufacturer already. In Sec. 2.2, I describe some practical challenges I have encountered when performing the experiments in this thesis and how I overcame them.
- The imaging approach we adopt naturally demands automated image analysis tools. In Sec. 2.3, I will describe the image analysis techniques I used.
- When investigating the rheology of bacterial suspensions, we adopted a homemade

microfluidic viscometer device. Details of the fabrication are shown in Sec. 2.4.

- A light-powered *E. coli* strain is used in the giant number fluctuations study and the emergence of active turbulence study (Chap. 4 and Chap. 5). This special strain was obtained by transforming a wild-type strain with an exogenous plasmid which encodes a light-harvesting membrane protein. The discovery and working principles of the light-powering feature has been well documented by earlier works [107–111]. Following these works, I constructed a plasmid containing the gene and successfully transformed the wild-type *E. coli* strain. In Sec. 2.5, I will present the details on the materials and procedures I used to construct the mutant as a practical guide to those who need to further modify or trouble shoot the strain I made.

## 2.1 Motile Bacteria Sample Preparation

Peritrichous *E. coli* bacteria have been widely used as model micro-swimmers for active fluid studies [112, 113]. By bundling and unbundling their flagella, they achieve a so called “run-and-tumble” motion, allowing them to more efficiently explore their surrounding environment and to search for supplies. Figure 2.1a shows a simplified model of a swimming *E. coli* bacterium model with a 2  $\mu\text{m}$  rod-shape body and a helical-shape flagellum of around 8  $\mu\text{m}$ . When swimming, all the flagella bundle together behind the cell and propel it forward [114]. Figure 2.1b and c show the bundled state and unbundled state of the flagella, respectively. A swimming *E. coli* bacterium can generate nontrivial fluid flow, which can lead to hydrodynamic attraction to boundaries, alignment with other bacteria and other consequences [115]. It had long been assumed in theoretical works that the effective flow generated by microswimmers like *E. coli* is dipolar, with one force pushing forward from the head and another force pushing backward from the

flagella [19,66,81,116]. This assumption was then experimentally verified by Drescher et al. in 2011 [117], by reconstructing the flow field from many tracer particle trajectories. Figure 2.1d and e show the flow field they measured and the best-fit force dipole flow. As I will show later, the swimming-induced flow plays a key role in the novel properties and collective motions in the bacterial active fluids.

In this section, the standard *E. coli* culturing and sample preparation protocol is shown.

### 2.1.1 Background Information

**Bacterial strains** We primarily work on two *E. coli* strains: AW804 and BW25113. AW804 is light-sensitive. BW25113 is a wild type strain carrying a plasmid encoding green fluorescence protein, thus it is used when fluorescence or confocal microscopy is needed. Both strains have ampicillin resistance marker and thus require supplementing ampicillin to culturing media.

**Antibiotics** Bacteria are ubiquitous in the environment and can easily contaminate our bacterial culture. In order to ensure the fidelity of the culture, we add antibiotic resistance markers to the bacteria we want to grow and meanwhile add antibiotics to the medium. The antibiotics inhibit the growth of contaminating species and allow our desired bacteria to grow normally.

**Medium** Various types of media (terrific broth, Luria broth, 2XYT and M9, etc.) are commonly used for bacterial culture. We use terrific broth. The recipe can be found in the protocol section.

### 2.1.2 Protocol

1. Prepare a 2-ml *E. coli* overnight culture.

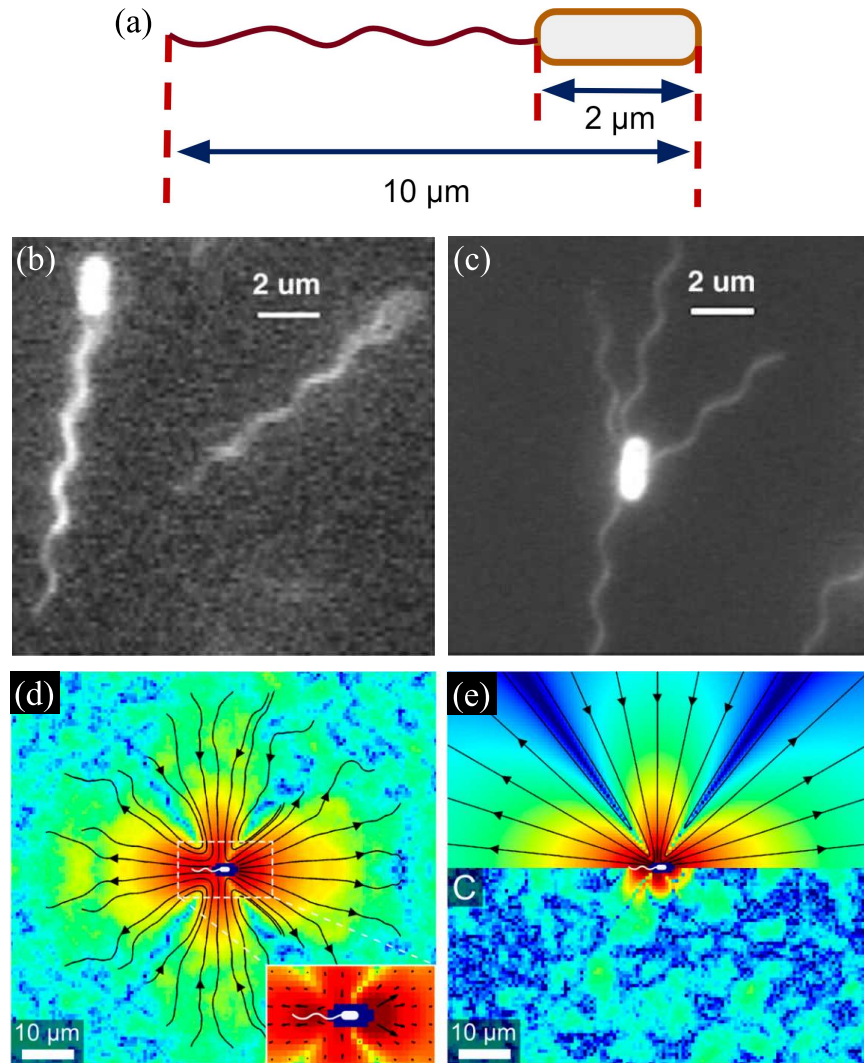


**Figure 2.1: Model swimmer *Escherichia coli* and its flow field.** (a) A schematic of a swimming *E. coli* bacterium. (b) Fluorescence microscopic image of swimming *E. coli* with bundled flagella. (c) Fluorescence microscopic image of tumbling *E. coli* with unbundled flagella. (d) Flow field around a swimming *E. coli*, measured with suspending microspheres. (e) Best-fit force dipole flow for the flow field shown in (d). Image sources: (b) and (c) are reprinted from Ref. [118] with permission from the American Society for Microbiology. (d) and (e) are reprinted from Ref. [117] with permission from the NAS.

(a) Prepare liquid terrific broth (TB). For example, to make 1 L TB, weigh out the following into a 1 L glass bottle:

- 23.6 g Yeast extract (Sigma-Aldrich)
- 11.8 g Tryptone plus (Sigma-Aldrich)
- 4 ml Glycerol (Thermo Fisher Scientific)
- Add dI water to 1 L

Loosely close the cap on the bottle (do NOT close all the way or the bottle may explode!) and then loosely cover the top of the bottle with autoclave tape (stick cap and bottle body together to avoid cap popping off). Autoclave and allow to cool to room temperature. Now screw on the top of the bottle and store the TB at room temperature.

- (b) Using a sterile 10 ml pipette, transfer 2 ml TB to a sterile glass test tube.
- (c) Using a sterile pipette, add 2 microliter (0.1% v/v) antibiotic solution to the TB in test tube.
- (d) Using a sterile pipette tip, pick a small chunk from our bacterial frozen stock (stored in the -80 °C freezer in 251) and carefully transfer the small chunk into the liquid TB + antibiotic.
- (e) Loosely cover the culture with sterile cap that is not air tight.
- (f) Incubate bacterial culture at 37 °C for 12-18 h in a shaking incubator.
- (g) After incubation, check growth, which is characterized by a cloudy haze in the media. This is the overnight culture.

2. Dilute overnight culture and harvest motile bacteria at mid-late log phase.

- (a) Using a sterile 10 ml pipette, transfer 3 ml TB to a sterile glass test tube.

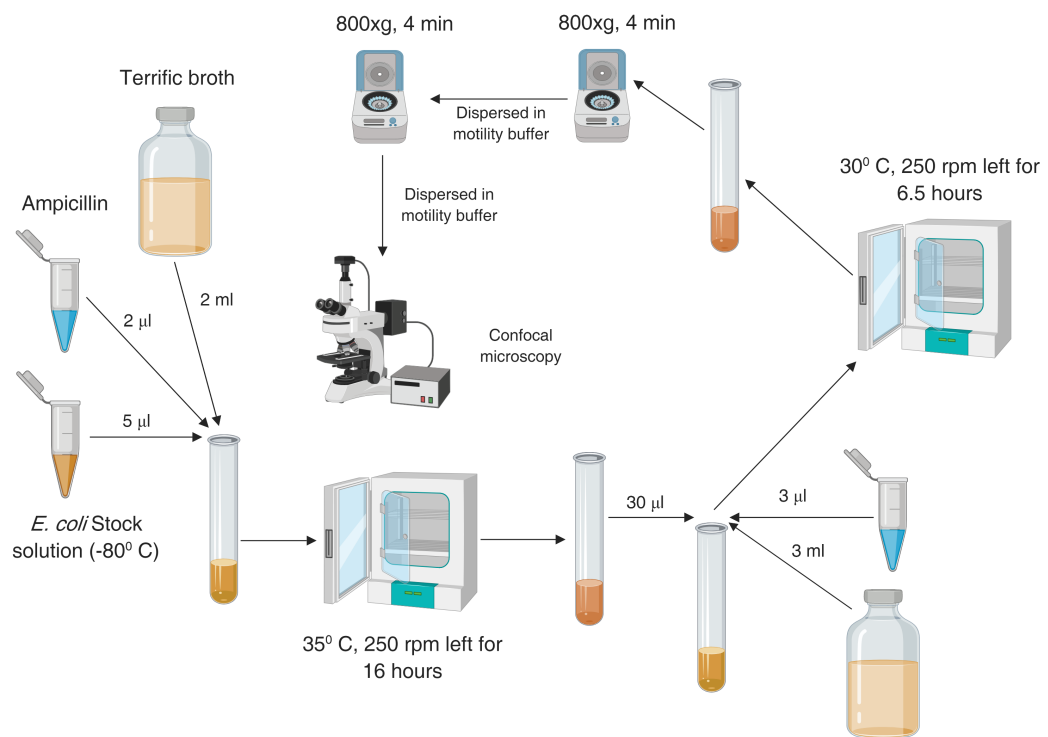


Figure 2.2: **Graphical motile *E. coli* sample preparation protocol.** Image courtesy of Shashank Kamdar.

- (b) Using a sterile pipette, add 2 microliter (0.1% v/v) antibiotic solution to the TB in test tube.
- (c) Transfer 30 microliter (1% v/v) overnight culture into the liquid TB + antibiotic.
- (d) Incubate bacterial culture at 30 °C for 6-6.5 h in a shaking incubator.
- (e) After incubation, check for growth, which is characterized by a cloudy haze in the media. This is the log phase bacteria.
3. Centrifuge for better motility and higher concentration bacterial sample.
- (a) Prepare motility buffer (MB), the following recipe is from Ref. [30].
- 0.01 M potassium phosphate (combine monobasic and dibasic solutions, Sigma-Aldrich)
  - $10^{-4}$  M EDTA (Sigma-Aldrich)
  - 0.002% weight fraction Tween 20 (Sigma-Aldrich)
  - Adjust pH to 7.0
- (b) Take out the log phase bacteria from the shaking incubator, centrifuge for 5 min at 800 rcf.
- (c) Discard the supernatant quickly and transfer the left-over liquid to a new centrifuge tube.
- (d) Add 500-1000 ul MB (or water) to resuspend the bottom pellet (avoid bottom pellet) and centrifuge for a second time (5 min, 800 rcf).
- (e) Discard the supernatant and let the tubes sit for two minutes. The remaining left-over liquid should be now filled with the active *E. coli*. Take the left-over solution in another capsule and use it for experiments.

- (f) To measure the concentration, transfer 10 microliter of the suspension into a 1 ml plastic cuvette (0.5 cm) and dilute 100 times (by adding 990 microliter water). Put the cuvette in the spectrophotometer (Eppendorf) and use the OD600 program. The resulting number times 100 will be the number density of your suspension in the unit of  $n_0$  ( $8 \times 10^8$  cells/ml).

## 2.2 Optical Microscopy

In this section, I will describe how I overcome practical challenges when applying optical microscopy on bacterial suspensions. Note that I will be describing some specific issues I encountered in my research. For beginners, the standard manuals are always the best reference [119].

### 2.2.1 Power *E. coli* with Illumination Light

In the studies of the giant number fluctuations and the emergence of active turbulence, I used a light-powered *E. coli* mutant, which changes its swimming speed according to the amount of light it receives (details of the light-powered *E. coli* mutant can be found in Sec. 2.5).

I use the illumination light of the microscope as the power source of the bacteria, instead of using another light source, based on two considerations: 1) an additional light source shining on the sample will lead to additional unexpected light going into the objective, which often leads to bad image quality, 2) it is hard to construct a spatially uniform light, especially when it has to come in an angle not perpendicular to the specimen. Therefore, I use the illumination light of the microscope to power the *E. coli*.

The light-powered *E. coli* mutant requires quite a high light intensity to move fast enough. Such a high intensity cannot be achieved in the normal microscopy conditions,

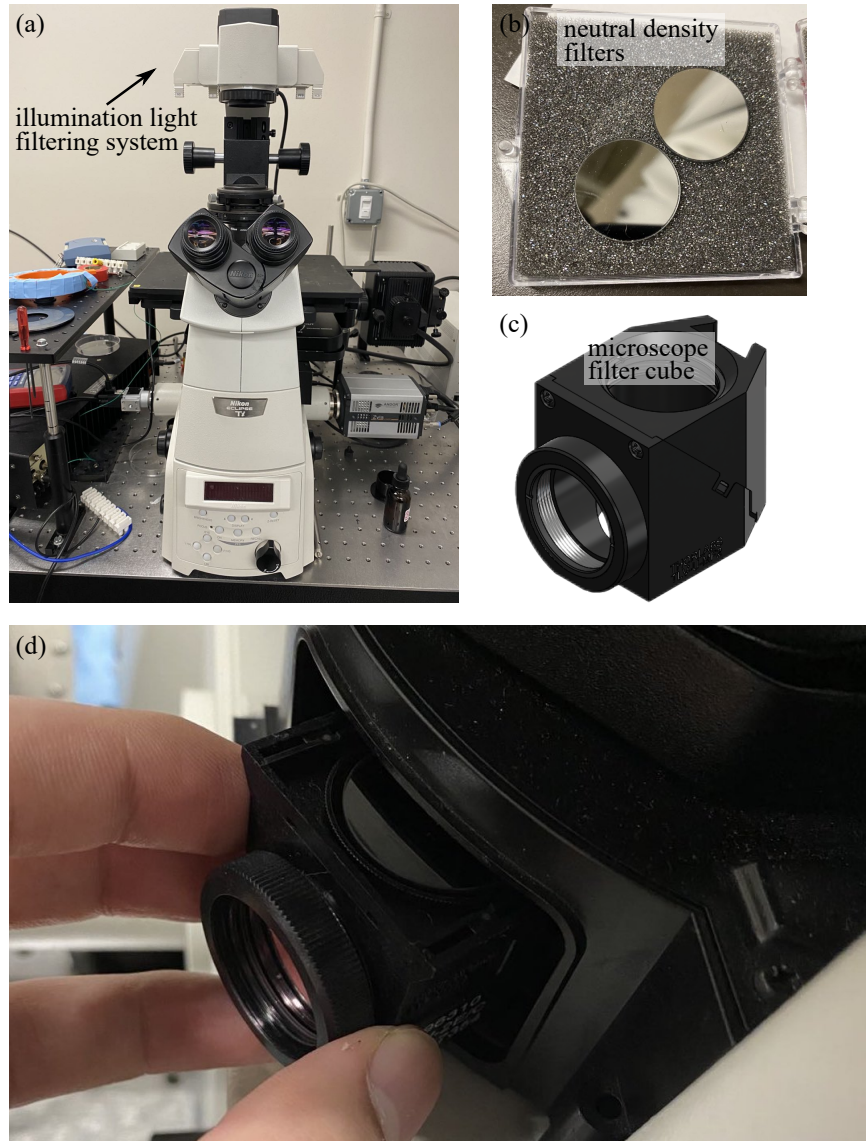


Figure 2.3: **Nikon Ti-E inverted microscope and its filters.** (a) Nikon Ti-E inverted microscope model and the illumination light path filters. (b) Neutral density filters. (c) Microscope filter block under objective. (d) Adding additional ND filter under objective.

where four light filters are applied for different purposes. Figure 2.3a show the Nikon Ti-E inverted microscope and the illumination light filtering system with the four light filters designated as ND, D, NCB and PFS. The functions of the filters are listed in Table. 2.1:

<b>ND</b>	Neutral density filter: adjust the brightness for normal microscopy or photomicroscopy
<b>D</b>	Diffusion filter: made of frosted glass and will diffuse light, used for equalizing the illumination
<b>NCB</b>	Neutral color balance: corrects the color temperature for normal microscopy or filming by daylight type color. Note: this filter is essential for optimal color reproducibility when taking color images, and it should be kept out of the optical path when filming in black and white.
<b>PFS</b>	Perfect focusing system: a hardware solution to combat axial focus fluctuations in real time during long-term imaging investigations. Note - this filter should be kept out if one does not intend to use the perfect focusing system.

Table 2.1: Filters in the illumination light path and their functions.

Removing some of those filters can make the illumination light strong enough to power the bacteria. According to the functions of the filters, the only necessary filter is the diffusion filter, given that one is not doing color imaging and is not using perfect focusing system, as it is in my experiment. Figure 2.4a shows an image taken without the diffusion filter (D). Without diffusing the illumination light, the resulting image is clearly inhomogeneous in a large range, with a bright center and a dark bottom area. By putting the diffusion filter in the illumination light path, one can make the illumination light much more uniform, as shown in Fig. 2.4b. All the other filters (ND, NCB, PFS) are effectively reducing the overall intensity. Putting in or out these filters only results in globally dimmer or brighter images, without changing the detailed patterns in the image. Thus, these three filters are optional in my experiment. Since powering the light-powered *E. coli* requires a very high light intensity, only the diffusion filter should

be kept in the illumination light path.

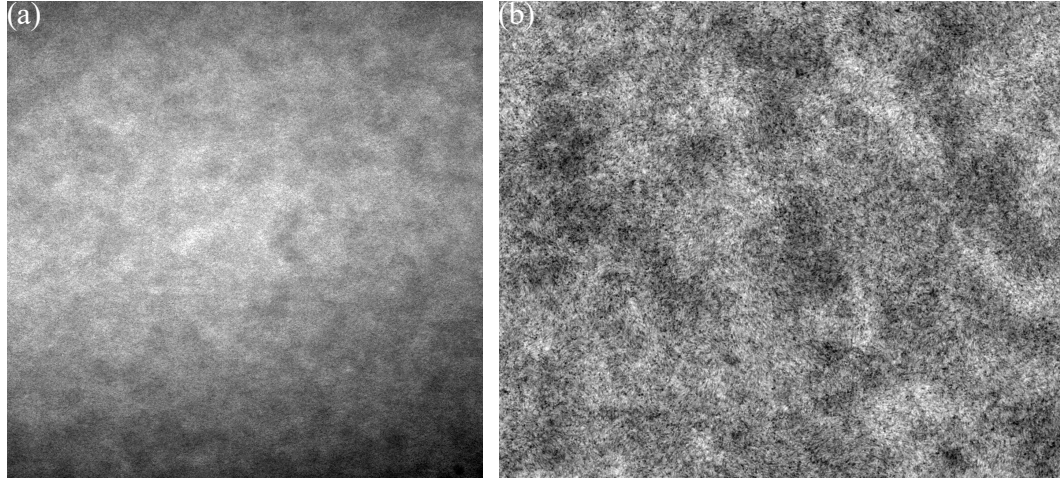


Figure 2.4: Image with (a) and without (b) the diffusion filter (D).

### 2.2.2 Adding Filters to Avoid Overexposure

In order to power the bacteria, the illumination light intensity needs to be set high. However, such high intensity causes a problem: the light is so strong that the camera is overexposed and does not record any meaningful signal. To avoid the overexposure, I add neutral density filters (Fig. 2.3b) between the specimen and the camera, so that I can keep the light intensity on the bacteria, and mean while make the light goes to the camera dimmer.

Fig. 2.3d shows how I placed the filters between the specimen and the camera. I took out one of the filter cube (Fig. 2.3c) from the turret under the objective, which is originally used for fluorescence microscopy. Then I put a piece of neutral density filter on top of the cube and put the cube back to the turret. This additional filter allows for the imaging under strong illumination light.

## 2.3 Image Analysis

With the fast developments of digital imaging, human are enabled to investigate many processes, ranging from astronomical object motions to microorganism behavior, in unprecedented detail [120]. While it is getting easier than ever to acquire large amount of images, a demand for automated image analysis has also become unprecedented [121–123].

In my research, particle tracking velocimetry (PTV) and particle image velocimetry (PIV) are the most frequently used automated image analysis methods. In this section, the working principles of both methods will be discussed, and examples will be given. Other image analysis techniques, such as the spatial (temporal) correlation function calculation and the energy spectrum calculation will also be discussed.

### 2.3.1 Anisotropic Particle Tracking

PTV has been one of the most useful automated image analysis tools in the study of colloids and microorganisms. Over the last 20 years, it has developed significantly and many algorithms, toolkits and all-in-one software have been implemented and applied in a variety of image analysis tasks. Despite the abundance of particle tracking tools, no agreement has been made on which one in the vast collection of tools works best. Much effort has been devoted to answer this question by comparing the performance of different tools [120,124–130]. In these studies, though different algorithms show different performance, no single algorithm outperforms all the others in all scenarios.

A challenge I encountered when working on the diffusion project was the detecting of the ellipsoidal particles surrounded by moving microorganisms (bacteria and algae). A local maxima finding method was applied previously to detect the center of an ellipsoidal particle [56]. Combined with intensity fitting around the center in different directions, the orientation of the particle can also be obtained. The same method, however, does

not work well for my image because of the presence of microorganisms, which give rise to many more local maxima in the image (a typical image is shown in Fig. 2.5a). To overcome this challenge, I adapted a thresholding and connected group labeling based method from Ref. [131–133]. The method has the following steps:

- threshold the grayscale image (Fig. 2.5a) to a binary image (Fig. 2.5b)
- find connected white regions (`skimage.measure.label` in Python)
- find the best-fit ellipse of each white connected regions found in the last step, as indicated by the red ellipses in Fig. 2.5c (`skimage.measure.regionprops` in Python)
- filter the parameters of the ellipses with appropriate criteria, so that only the desired ellipse is found, as indicated by the red ellipse in Fig. 2.5d

Fig. 2.5 only illustrates the essential idea of the method. When applying the method, some necessary image preprocessing, including linear, nonlinear and frequency filters need to be used to make sure the desired features stand out, and the undesired noises are suppressed. The preprocessing techniques have been reviewed in Ref. [123, 124]. This method was used to obtain the trajectories of ellipsoidal particles in algal suspensions, which was then used to calculate the diffusivity for my first collaborative project, reported in Ref. [35].

### 2.3.2 Particle Image Velocimetry

PIV is a method of visualizing flow using based on images. It is used to obtain instantaneous fluid velocity fields by comparing positions of tracer particles in the fluids in consecutive image frames. The tracer particles are assumed to follow the flow faithfully all the time, and this assumption is in general valid when particle size is small.

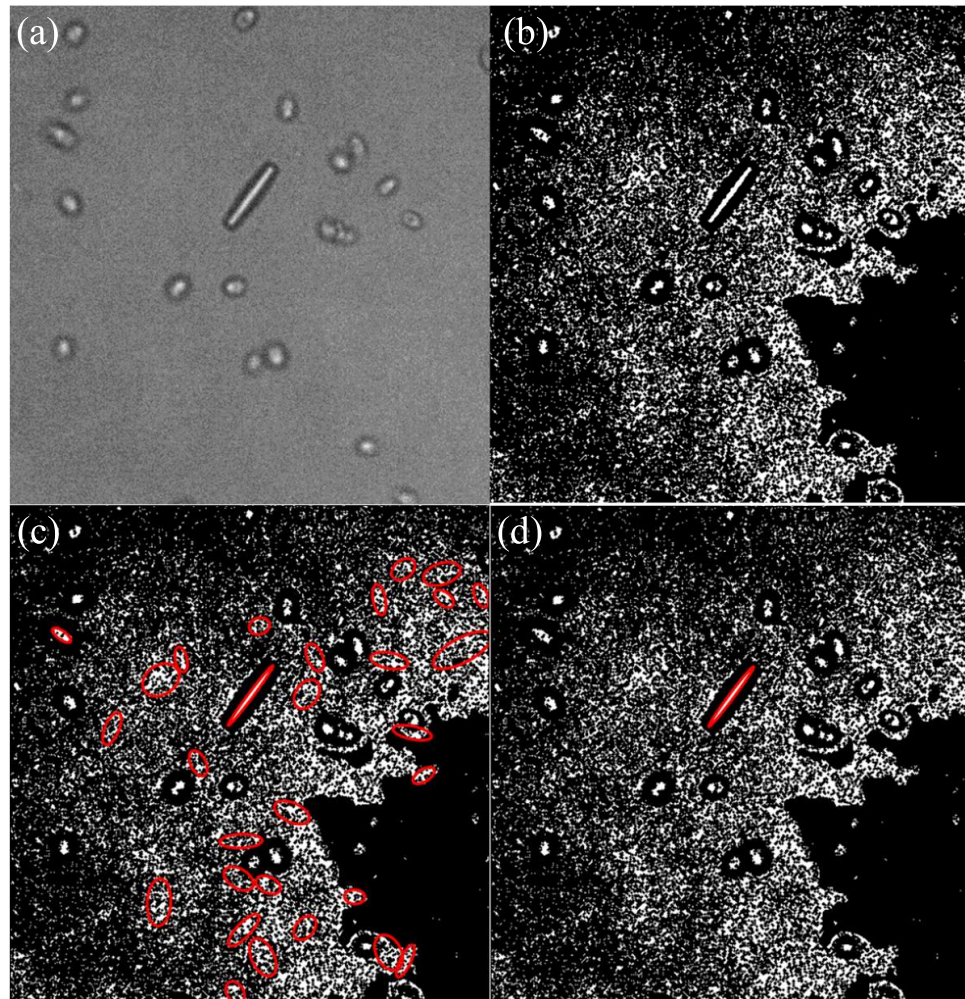
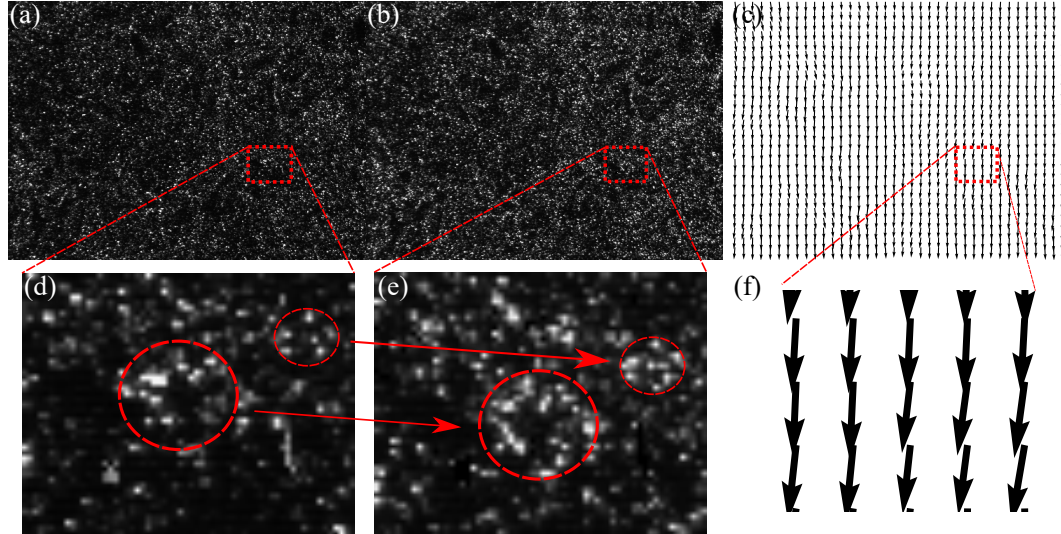


Figure 2.5: **Illustration of ellipsoidal particle detection by thresholding and group labeling.** (a) The raw image: an ellipsoidal polystyrene particle surrounded by swimming algae in a suspension. (b) Binarized raw image. (c) Detection result of connected white regions. (d) Final result after appropriate filtering.

The degree of how faithful the tracers follow the flow is quantified by Stokes number, which compares the intrinsic relaxation time scale and the characteristic time scale of the flow.



**Figure 2.6: PIV working principle illustration.** (a) and (b) are images of fluid flows seeded with tracer particles. (c) is the instantaneous velocity field in (a) and (b), obtained from PIV. (d) and (e) are zoom-in's of the two images in a small window. Circles indicates similar image features in (d) and (e). (f) is a zoom-in of velocity field.

The comparison between two image frames is done by dividing the images in to small interrogation windows and computing the correlations of the two images in these windows, which essentially looks for the similar features between the two images. This procedure is illustrated in Fig. 2.6.

Figure 2.6a and b are two example images and Fig. 2.6c shows the instantaneous flow field obtained from PIV analysis. The result suggests that there is a global flow going to the bottom of the images. Though it is not so obvious in the original images, if we zoom in to a small region, as shown in Fig. 2.6d and e, the similar features (indicated by red circles) get obvious and we therefore expect the flow going to the bottom of the

images, as shown in Fig. 2.6f.

Invented in the 1970s, PIV has been developed into a mature flow velocimetry technique today. Several implementations of the algorithm are present in different programming frameworks, such as Matlab, Mathematica and Python. In this work, we use an open source PIV toolkit *OpenPIV* written in Python, which is maintained by Liberzon and co-workers [134, 135].

### 2.3.3 Spatial and Temporal Correlation Functions

Spatial (temporal) correlation functions describe how variables, such as velocity and density, at different positions (time) are related. It measures the order in a system. These functions are used in the study of giant number fluctuations to measure the characteristic length and time in bacterial suspensions of different volume fractions (Chap. 5).

The correlation functions have been defined clearly in statistical mechanics and mathematics. For example, the spatial correlation function of number density  $n(\mathbf{r})$ ,  $C_n(\mathbf{R})$  is

$$C_n(\mathbf{R}) = \frac{\langle n(\mathbf{r}) \cdot n(\mathbf{r} + \mathbf{R}) \rangle - \langle n(\mathbf{r}) \rangle \langle n(\mathbf{r} + \mathbf{R}) \rangle}{\sigma_{n(\mathbf{r})}^2} \quad (2.1)$$

where  $\langle A \rangle$  denotes the spatial average of  $A$ , and  $\sigma_A$  denotes the standard deviation of  $A$ .

Although the definition is clear, the programming implementation can be quite different in efficiency. When implementing these correlation functions, I learned an important trick—code vectorization—which can speed up the computation of correlation functions up to 50 times. The enhancement of performance gets more pronounced when the input data is larger. Therefore, I would like to document this knowledge here.

The calculation of the correlation function in Eq. 2.1 requires going over the whole space twice: for each point  $\mathbf{r}$  in the space, all possible distance  $\mathbf{R}$  needs to be examined.

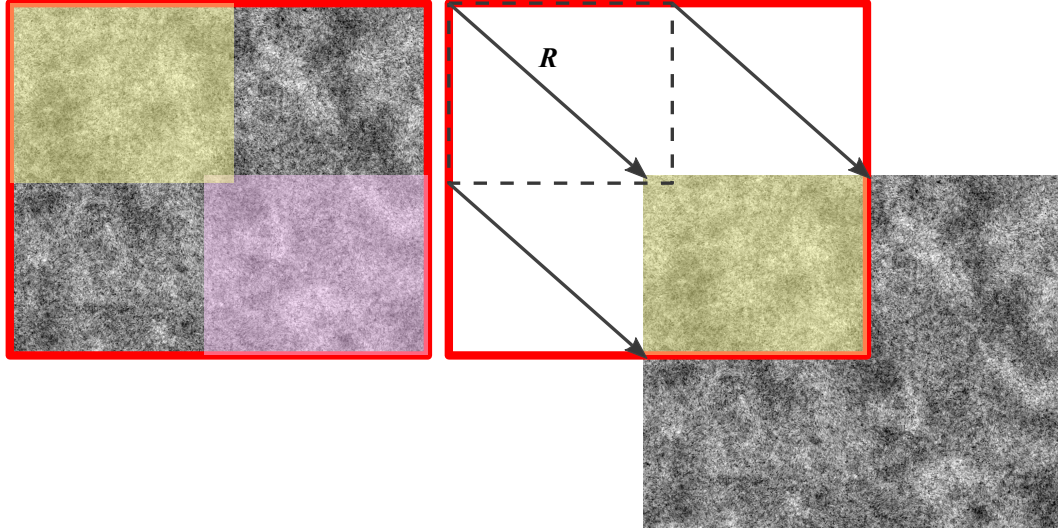


Figure 2.7: **Code vectorization illustration.** The correlation function at a certain distance  $\mathbf{R}$ ,  $C(\mathbf{R})$  can be calculated without using a `for` loop. Two subspaces are identified from the whole space, as indicated by purple and yellow shaded regions, which are  $\mathbf{R}$  away from each other.  $C(\mathbf{R})$  can be calculated by taking the product of these two subspaces and then taking the mean of this product.

In two dimensional space, this procedure leads to four `for` loops. The basic idea of code vectorization is to avoid the extensive use of `for` loops. In this specific case, for every possible distance  $\mathbf{R}$ , the correlation can be calculated without using a `for` loop, by directly calculating the product of two subspaces and the taking average, as illustrated in Fig. 2.7. Two subspaces are identified from the whole space, which are  $\mathbf{R}$  away from each other, as indicated by purple and yellow shaded regions. Note that matrix product calculation is well optimized in almost all programming languages and is much faster than looping over every element in a matrix. Using this trick, only two `for` loops are necessary, which go over all possible distances  $\mathbf{R}$ . The Python implementations of spatial and temporal correlation functions, as well as a speed comparison between non-vectorized and vectorized programs, can be found in Appendix. B.1.

### 2.3.4 Energy Spectrum Calculation

As discussed in Sec. 1.3.2, energy spectra have been widely used for studying the flow structure of classic turbulent flows, by revealing the kinetic energy distributions over different length scales. Here, we show the details in the method of calculating energy spectra of the flow in bacterial suspensions at various volume fractions, using the velocity fields obtained from PIV analysis. This calculation will be used in Chap. 4 and Chap. 5.

The energy spectra of bacterial suspensions are calculated as the following

$$E(k_x, k_y) = \frac{\langle u_k(k_x, k_y)u_k^*(k_x, k_y) + v_k(k_x, k_y)v_k^*(k_x, k_y) \rangle}{2A} \quad (2.2)$$

where  $E$  is the energy density in  $k$  space,  $u_k$  and  $v_k$  are  $k$  space velocity fields,  $A$  is the real space area of the system and  $*$  denotes the complex conjugate. The  $\langle \cdot \rangle$  denotes an average over multiple images from different times.

The fourier transform of real space velocity  $u_k$  and  $v_k$  are computed as the following:

- apply the built-in Fast Fourier Transform (FFT) function of Python `numpy.fft` package to the discrete velocity field  $v(x, y)$  (from PIV) to get  $V_k(k_x, k_y)$
- since the FFT is defined as

$$V_k = \sum_{m=0}^{n-1} v_m \exp(-2\pi i \frac{mk}{n})$$

missing the  $dx$  counterpart in the continuous Fourier transform, we additionally multiply  $d_{step}^2$  to  $V_k(k_x, k_y)$  to get the wavenumber domain velocity  $v_k(k_x, k_y)$

- the wavenumber field  $k$  corresponding to  $v_k(k_x, k_y)$  is obtained by applying the `numpy.fft.freq` function. Since the definition of FFT introduces a prefactor  $2\pi$  to the wavenumber, an additional  $2\pi$  is also multiplied to  $k$

The calculation described above is implemented in a Python code, which can be found in Appendix.B.2.

### 2.3.5 Other Image Analysis Tools

- Particle tracking based on image cross-correlation (Appendix.B.3)
- Orientation tracking based on Fast Fourier Transform (FFT) (Appendix.B.4)
- Density fluctuation calculations (Appendix.B.5)

## 2.4 Micro-fabrication and Microfluidic Viscometer

### 2.4.1 Micro-fabrication

We used a standard micro-fabrication technique, soft lithography, to produce the microfluidic viscometer we used in the rheology project (Chap. 3) [136]. Such a fabrication usually involves the following steps: experimental design, pattern design, mask fabrication, master fabrication and elastomeric stamp fabrication. After deciding on using the Y-shaped channel viscometer (Fig. 2.8a) [24], I did the pattern design and the staff at Minnesota Nano Center (MNC) had the mask fabricated for me. With the mask, I fabricated the masters of the Y-shaped channel viscometer for various channel heights using the MNC facilities. Then the masters were used for fabricating elastomeric stamps, using Sylgard 184 Silicone Elastomer Kit (Dow Inc.).

To produce masters for the various channel heights, different photoresists need to be used. I chose the SU-8 3000 series photoresists due to their good adhesion property and reduced coating stress, as well as their ready availability in the MNC labs. SU-8 3025 was used for channel heights from 25 to 50  $\mu\text{m}$ . SU-8 3050 was used for channel heights from 50 to 128  $\mu\text{m}$ . Following the procedures described in the photoresist manual, which

includes substrate preparation, spin coating, soft bake, exposure, post exposure bake and develop, a photoresist patterned silicon wafer can be produced (Fig. 2.8b).

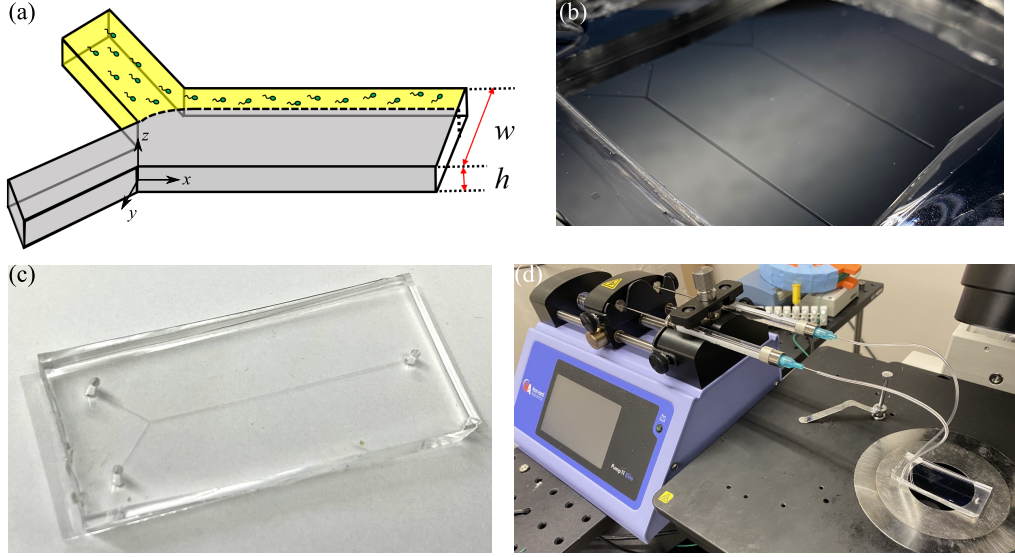


**Figure 2.8: Microfluidic viscometer fabrication and setup.** (a) A sketch of the Y-shaped channel microfluidic viscometer. The length and width of the two arms are 1 cm and  $300 \mu\text{m}$ , respectively. The length and width of the main channel are 4 cm and  $600 \mu\text{m}$ , respectively. The height of the channel  $h$  ranges from  $25 \mu\text{m}$  to  $128 \mu\text{m}$ . (b) Master mold of the channel. (c) PDMS channel. (d) Viscometer connected to a syringe pump by plastic tubes, placed on Nikon inverted microscope specimen stage.

The elastomeric stamp is fabricated by pouring the Sylgard 184 Silicone Elastomer Kit, which contains a base and a crosslinker in a volume ratio 10:1, onto the photoresist masters. After curing for 3 hours at  $70^\circ\text{C}$ , the pattern of the master mold was perfectly replicated on the solidified elastomer. Finally, a piece of coverslip was stuck on the patterned side of the elastomer by plasma cleaning the surfaces of both. The microfluidic channel is shown in Fig. 2.8c. The length and width of the two arms are 1 cm and  $300 \mu\text{m}$ , respectively. The length and width of the main channel are 4 cm and  $600 \mu\text{m}$ , respectively. The height of the channel  $h$  ranges from  $25 \mu\text{m}$  to  $128 \mu\text{m}$ . Two cylindrical

holes were punched at the ends of the two arms so that fluids can be pumped in.

### 2.4.2 Microfluidic Viscometer

To use the elastomeric stamp as a microfluidic viscometer, we connected it with a precision syringe pump (Harvard Apparatus, Elite 11) through elastic tubes, as shown in Fig. 2.8. The two syringes contained two different fluids: one was the bacterial suspension with viscosity to be measured, and the other was a reference fluid with known viscosity, typically water. The two fluids were pumped into the viscometer at the same volumetric flow rate  $Q$ .

The working principle of the viscometer is that thicker fluids flow slower than thinner ones. More formally, if we examine a fluid with viscosity  $\eta$ , driven by a pressure gradient  $dp/dx$  to flow in the  $x$ -direction between two parallel no-slip boundaries at  $z = \pm h/2$ , as shown in Fig. 2.8a. At low Reynolds number limit, the flow rate regime of interest, the flow is governed by Navier-Stokes equation

$$0 = -\frac{dP}{dx} + \eta \frac{d^2 u_x}{dz^2} \quad (2.3)$$

The resulting flow is parabolic in  $x$ - $z$  plane and is approximately constant in  $y$ -direction, and can be described by Eq. 2.4

$$u_x(z) = \frac{1}{2\eta} \frac{dP}{dx} \left( \frac{y^2}{h^2} - \frac{1}{4} \right) \quad (2.4)$$

For two different fluids with viscosities  $\eta_1$  and  $\eta_2$ , the mean flow velocity in  $x$ -direction  $\langle u_1 \rangle$  and  $\langle u_2 \rangle$  are related to each other by

$$\frac{\langle u_1 \rangle}{\langle u_2 \rangle} = \frac{\eta_2}{\eta_1} \quad (2.5)$$

noting that the flow rate  $Q = \langle u \rangle dh$ , where  $d$  is the width ( $y$ -direction) of the flow, we can substitute the velocities  $\langle u_1 \rangle$  and  $\langle u_2 \rangle$  in Eq. 2.5 to get

$$\frac{d_1}{d_2} = \frac{\eta_1}{\eta_2} \quad (2.6)$$

Eq. 2.6 is the working equation of the microfluidic viscometer. By imaging and measuring the width  $d_1$  and  $d_2$  of the two fluids in the channel, and combining the known viscosity of the reference fluid  $\eta_2$ , we can measure  $\eta_1$ .

## 2.5 Light-controlled *E. coli*: Genetic Modification and Culturing

Controlling the swimming speed of swimmers can enormously expand the capability of experimental active fluid investigations. Our lab used to exploit a “negative phototaxis” property of a mutant *E. coli* strain to control its swimming speed. The mutant strain carries a *hemH* gene knockout, so that it accumulates protoporphyrin IX. When exposed to blue light, protoporphyrin IX catalyzes the production of H<sub>2</sub>O<sub>2</sub>, which causes the “negative chemotaxis” tumbling response of the *E. coli* mutant [137]. Although this mutant strain enables us to reduce the swimming speed, the recovery of swimming speed remains challenging due to the excessive production and accumulation of toxic H<sub>2</sub>O<sub>2</sub>. Hence, some important experiments, such as the study of the onset of active turbulence, which will be detailed in Chap. 4, cannot be done with this strain.

An alternative mechanism that can be exploited to control bacterial swimming speed is to introduce a light-driven proton pump protein, proteorhodopsin (PR), to *E. coli*. PR protein has been found in marine micro-organisms [107, 109], and has recently been successfully expressed in *E. coli* [110]. In contrast to the *hemH* knockout mutant, PR is much less harmful and provides better recovery of swimming speed. Therefore, I

transformed the wildtype *E. coli* K-12 strain BW25113 (Ref. [138]) with a plasmid pZE-PR containing the gene that encoded the PR protein. The sequence of the PR gene was found in Ref. [109] and was synthesized by Eurofins Scientific. The plasmid was constructed by the standard protocol consisting of PCR, enzymatic digestion and ligation. The PCR was carried out with Phusion High-Fidelity DNA polymerase (New England BioLabs) according to the manufacturer's instructions. Both the plasmid vector pZE and the PR gene were digested with Acc651-Xba1, and were subsequently ligated. XL10-Gold *E. coli* strain was used for cloning the plasmid. Finally, the wildtype strain BW25113 was transformed with the plasmid by electro-poration and the light-controlled *E. coli* mutant strain was constructed. The details of bacterial strains, plasmids and primers used in this work are listed in Table. 2.2.

name	Relevant genotype or sequence	Reference
<i>Strains</i>		
BW25113	$rrnB_{T14}$ $\Delta lacZ_{WJ16} hsdR514 \Delta$ $araBAD_{AH33}$ $\Delta rhaBAD_{LD78}$	[138]
XL10-Gold	Tet <sup>R</sup> $\Delta(mcrA)183$ $\Delta(mcrCB-hsaSMR-mrr)173endAls$ $supE44$ $thi-l$ $recAl$	Stratagene
<i>Plasmids</i>		
pZE-PR	ColE1 origin, Amp <sup>R</sup> , P <sub>L</sub> lacO <sub>1</sub> : PR	This work
<i>Primers</i>		
PR-Acc651-F	CCCGGGGGTACCATGAAGTT GTTGTTGATCTTGGGAT	
PR-Xba1-R	CCCGGGTCTAGATTATGCG TTCGATGACTCTTCACG	

Table 2.2: Strains, plasmids and primers.

The chromophore retinal molecule is essential for the PR protein to function as a proton pump. The retinal is isomerized upon illumination, and in this way it drives the proton transportation across cell membrane [108]. *E. coli* does not synthesize such

molecules. In order to activate the function of PR in *E. coli*, we need to supplement the culturing media of *E. coli* with retinal, in the form of ethanol solution of all-trans-retinal (Sigma-Aldrich). Typically, a 10 mM all-trans-retinal solution is prepared as a stock solution. When supplementing the culturing media, 1/1000 volume of retinal solution is used to achieve a final concentration 10  $\mu$ M. To trigger the expression of PR gene under a  $P_{Llac}$  operon, we also need to supplement the culturing media with another chemical Isopropyl  $\beta$ -D-1-thiogalactopyranoside (IPTG, Sigma-Aldrich) at a final concentration 1 mM. Therefore, when culturing the light-controlled *E. coli*, an additional step needs to be added to the standard protocol (described in Sec. 2.1.2) between step 2(c) and 2(d). Typically, 3 hours after step 2(c), retinal and IPTG are supplemented to the culturing media.

## Chapter 3

# Rheology of Bacterial Suspensions under Confinement\*

### 3.1 Introduction

An active fluid is a suspension of self-propelled particles in fluid media with examples including a wide range of biological and physical systems ranging from swimming microorganisms [113] to suspensions of synthetic colloidal swimmers [15, 44, 139] and to ATP-driven cytoskeletons [72, 73]. With the ability of converting ambient or internal free energy to mechanical work at microscopic scales, active fluids can maintain a nonequilibrium steady state with uniform free energy input and display features drastically different from those of passive colloidal suspensions [7, 9, 82, 86, 115]. Many nonequilibrium properties of active fluids such as the emergence of collective motions [21, 83, 140, 141], giant number fluctuations [67, 94], and enhanced diffusion of passive particles [29, 30, 32, 35, 63] have been extensively studied in recent years. Among all these novel properties, the rheological response of active fluids presents arguably

---

\*Reproduced in part with permission from (Zhengyang Liu, Kechun Zhang and Xiang Cheng, “Rheology of bacterial suspensions under confinement”, *Rheologica Acta*, Springer).

the most surprising phenomena, challenging our understanding of the flow of complex fluids [28]. By measuring the decay of large vortices and the torque on a rotating probe, Sokolov and Aranson first experimentally showed that the viscosity of bacterial suspensions in a freestanding film can reduce by a factor of seven compared with the suspending fluid without bacteria [23]. Gachelin and co-workers used a Y-shaped microfluidic channel—a technique we will adopt below in our study—to measure the viscosity of bulk bacterial suspensions [24]. They showed that the viscosity of bacterial suspensions can be significantly lower than that of the suspending fluid. More recently, measurements by Lopez et al. using a conventional bulk rotational Couette rheometer demonstrated zero or even a negative apparent viscosity in bulk bacterial suspensions at low shear rates [25]. In contrast to pusher swimmers such as bacteria, suspensions of algae, an example of puller swimmers, show a noticeable viscosity enhancement compared with suspensions of immobile algae at the same concentrations [22].

Several mechanisms have been proposed to explain the unusual rheology of active fluids (see Ref. [28] and references therein). The most widely circulated theory considers the coupling between the orientation of elongated bacteria modified by external shear and the intrinsic force dipoles exerted by bacteria on the suspending fluid. Orientated along the extensional quadrant of an imposed shear flow, a bacterium exerts a force dipole on the fluid, which induces a disturbance flow opposite to that induced by a passive elongated particle of the same shape. Such an effect, first explained by Hatwalne et al. [18], leads to a reduction of the resistance of pusher suspensions to shear and the decrease of suspension viscosity. Incorporating further orientational dynamics of bacteria, continuum kinetic theories have been constructed based on the above picture, which quantitatively explained the rheology of dilute bacterial suspensions [54, 142–146]. Hydrodynamic models have also been developed along a similar line [39, 42, 55], which successfully predicted the existence of bacterial superfluids with a zero apparent viscosity

[38]. A second viscosity-reduction mechanism has recently been proposed by Takatori and Brady [43, 147, 148]. They considered the coupling between the shear flow and the swimming and rotational motion of active particles, which gives rise to an anisotropic active diffusivity in analogy of Taylor dispersion. The resulting diffusive stress stretches the fluid along the extensional direction of shear, similar to the effect of the force dipole induced by individual pusher swimmers, which leads to viscosity reduction even for spherical swimmers. Lastly, experiments on suspensions of bacteria and microtubules suggested that elongated active particles align near a system boundary and form a smectic layer along confining walls in self-driven flows [47, 48, 51]. This boundary layer collectively propels the fluid in the bulk and results in a self-sustained directional flow with a zero or negative apparent viscosity.

While the rheology of bulk bacterial suspensions has been measured [24, 25], the effect of confinement on the rheology of bacterial suspensions has not been explored experimentally. The study of the rheology of confined bacterial suspensions is important from both fundamental and practical perspectives. First, the study shall provide crucial information for verifying different models. In particular, the boundary-layer mechanism suggests that the unusual rheology of active fluids originates from the boundary and, therefore, should strongly depend on system sizes. In comparison, both the kinetic theory and the diffusive stretching theory apply for bulk suspensions. Confinement may modify the rheology of active fluids in these theories indirectly via effects such as the change of particle orientations and density distributions near confining walls [54] Second, various interesting collective dynamics including spontaneous directional flows [47, 48, 51] and stable bacterial vortices [50, 51, 149] have been found in confined active fluids. The consequence of these new phases on the rheology of active fluids is still unclear. Finally, confinement is frequently encountered in natural context of microbial systems, e.g. sperm cells in reproductive tracts and microorganisms in soil and biofilms [150, 151].

Thus, the study on the rheology of confined bacterial suspensions will also help to understand bacterial transport in confined geometries.

Here, using *Escherichia coli* (*E. coli*) as our model active swimmers, we experimentally study the rheology of active fluids in microfluidic channels under different degrees of confinement. Our study reveals a strong confinement effect on dilute bacterial suspensions: the apparent viscosity of suspensions reduces by a factor of three when the confinement scale decreases from 60 down to 25  $\mu\text{m}$ . We demonstrate that the effect of confinement is directly linked to the motility of bacteria. Furthermore, we also probe the microscopic dynamics of sheared bacterial suspensions such as the velocity profiles of suspension flows and the variation of bacterial density within confined channels. These microscopic measurements allow us to construct a simple model based on the boundary-layer mechanism, which qualitatively explains the experimental observations. Thus, our study provides not only systematic experimental results on the rheology of confined bacterial suspensions but also evidence on the effect of the boundary layer on the rheology of active fluids.

## 3.2 Methods

### 3.2.1 *E. coli* Suspensions

In our experiments, we use a fluorescently tagged *E. coli* K-12 strain (BW25113) as our microswimmers, which carry the PKK PdnA-GFP plasmid. These fluorescent cells allow us to image suspension flows with fluorescence and confocal microscopy. To prepare a motile *E. coli* suspension, bacteria are first cultured overnight at 37 °C in a terrific broth (TB) culture medium (tryptone 11.8 g/L, yeast extract 23.6 g/L, and glycerol 4 ml/L) supplemented with a 0.1% (v/v) selective antibiotic (ampicillin 100 mg/L). A small volume of the overnight culture is then diluted in a fresh TB culture

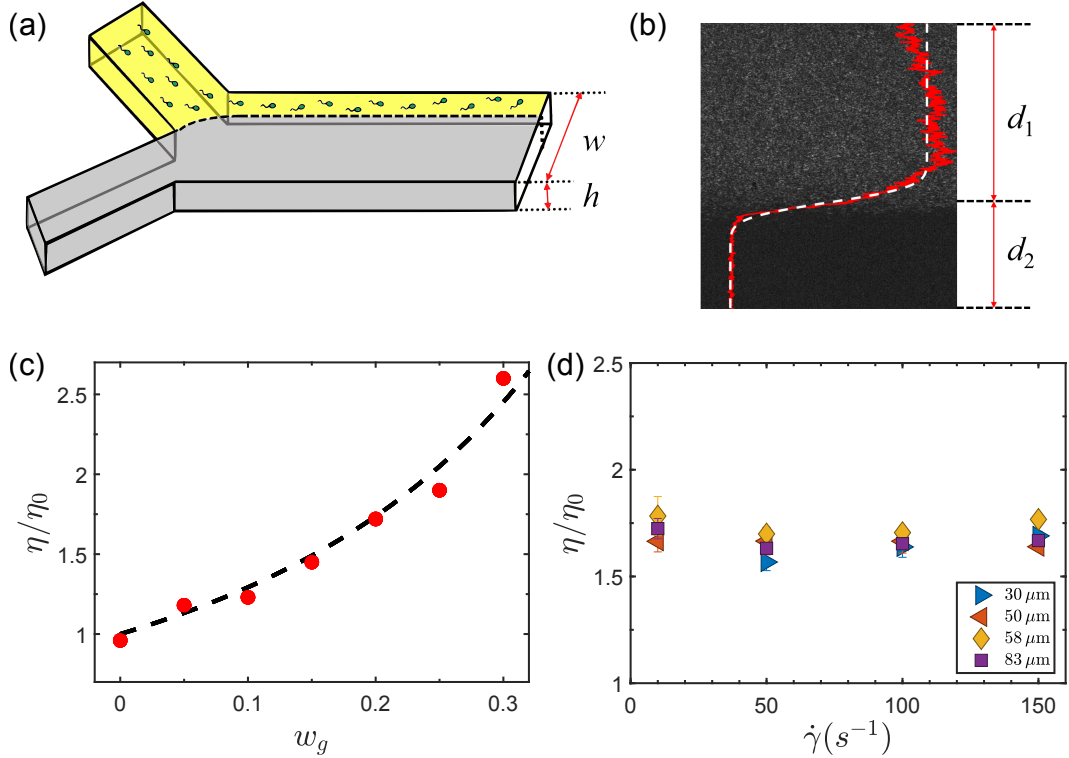


Figure 3.1: **Microfluidic viscometer.** (a) Schematic of the Y-shaped microfluidic channel. (b) Image of two fluids in the channel. The upper region is a bacterial suspension with width  $d_1$ , whereas the lower region is the suspending fluid with width  $d_2$ . The red line shows the intensity profile across the channel. The white dashed line is the error function fitting. (c) Viscosity of water-glycerol mixtures at different glycerol weight fractions,  $w_g$ . Shear rate  $\dot{\gamma} = 100 s^{-1}$ . The dashed line is the literature value. (d) Viscosity of a water-glycerol mixture (20 w% glycerol) as a function of shear rates at different channel heights  $h$ . The literature value of the viscosity of the mixture is 1.74 mPa s at 20 °C.  $h$  is indicated in the figure.

medium (1:100) and grown at 30 °C in a shaker at 220 rpm for 6.5 h. The culture is finally washed with a motility buffer via centrifuging (5 min, 800 g) and set to a desired concentration of  $n = 1.6 \times 10^{10}$  cells/ml. At this dilute concentration, bacteria do not show strong collective swarming [141]. For an isolated wild-type *E. coli*, it executes the so-called run-and-tumble motion [152]. In the “run” phase, the cell is propelled forward by a flagellar bundle at a constant speed  $v \approx 22 \mu\text{m}/\text{s}$ . The straight “run” is punctuated by a sudden and rapid “tumble” at a rate  $f$  on the order of 1 Hz, which randomizes the orientation of the cell. The run length of bacteria is thus given by  $L = v/f$ . For the wild-type bacteria, we have  $L = 33.1 \pm 8.1 \mu\text{m}$ .

For control experiments, we also culture a mutant strain of *E. coli*, which exhibits only tumbling motions without run. The tumbler strain we use is RP1616 ( $\Delta cheZ$ ), which is a derivative from RP437, a strain commonly used in chemotaxis study [153] (Parkinson 1978). Phospho-CheY and CheZ are the two primary enzymatic complexes governing bacterial chemotactic behaviors. Phospho-CheY enhances the clockwise rotation of the flagellar motors that enables the tumbling of bacteria. CheZ promotes the dephosphorylation rate of phospho-CheY to make the bacteria stop tumbling and transition into the “run” phase. Thus, the function of CheZ ensures that bacterial tumbling is short and the locomotor responses to changes in chemicals are rapid. By knocking out *cheZ*, we slow down the dephosphorylation rate of phospho-CheY, which leads to the accumulation of phospho-CheY in bacteria. The excessive phospho-CheY makes the bacteria keep tumbling instead of performing a run-and-tumble motion. The culturing procedure of tumblers is the same as the one for the swimmers described above. Lastly, we test the rheology of the dead bacteria as control. Bacteria are neutralized by adding 10 mM sodium azide in the suspensions.

### 3.2.2 Microfluidic Viscometer

We use a microfluidic viscometer for viscosity measurement. The same technique has been used in studying the rheology of bulk bacterial suspensions [24]. As sketched in Fig. 3.1a, the viscometer consists of a symmetric Y-shape microfluidic channel with height  $h$  and width  $w$  in the main channel. In order to investigate the effect of confinement, we fabricate channels of different  $h$  ranging from 25 up to 128  $\mu\text{m}$ , whereas  $w$  is fixed at 600  $\mu\text{m}$ . The two side branches have the same height  $h$  but half of the width of the main channel  $w/2$ . Under these conditions, the flow in the main channel satisfies the Hele-Shaw approximation [154], where shear gradients along the height direction ( $y$ ) dominate the flow. We define a coordinate system in the main channel as follows:  $x$  is along the flow direction,  $y$  is along the height direction with dominant shear gradients, and  $z$  is the vorticity direction along the width of the channel. The origin of the coordinate is set at the center of the channel with  $y \in [-h/2, h/2]$  and  $z \in [-w/2, w/2]$ .

In a typical experiment, we inject a bacterial suspension of unknown viscosity and the suspending fluid of known viscosity into the microfluidic channel through the two side branches separately at the same flow rate using a syringe pump (Harvard Apparatus, 11 Elite) and two 100- $\mu\text{l}$  syringes (Scientific Glass Equipment). The interface between the two fluids stabilizes downstream of the merging point of the two branches in the main channel with the width of the two fluids at  $d_1$  and  $d_2$ , respectively. Since the bacteria constantly migrate across the interface from the suspension into the suspending fluid, the interface gradually smooths out along the flow. We measure  $d_1$  and  $d_2$  at the position where the interface is stable and sharp, typically 500 to 1000  $\mu\text{m}$  downstream of the merging point (Fig. 3.1b). It can be shown that the viscosity ratio of the two miscible fluids in the channel,  $\eta_1/\eta_2$ , is equal to the width ratio  $d_1/d_2$  [155, 156]. We test the accuracy of the viscometer at different  $h$  by measuring the viscosity of water-glycerol mixtures. The results from the microfluidic viscometer quantitatively agree with the

known viscosity of the mixtures and are independent of the channel height in the range of our experiments (Fig. 3.1c and d).

In this study, we take the nominal wall shear rate  $\dot{\gamma} \equiv 6Q/(d_1 h^2)$  as a characteristic shear rate on bacterial suspensions, where  $Q$  is the control flow rate. The formula is exact when the velocity profiles of suspensions are parabolic following the Hagen-Poiseuille law. The average of the magnitude of shear rates in the channel is then  $\dot{\gamma}/2$ . For non-parabolic profiles, the formula can be simply treated as a definition of the characteristic shear rate in the channel. For each channel height  $h$ , we decrease  $Q$  from 100 to 1  $\mu\text{l/h}$  to examine the rheological response of bacterial suspensions at different  $\dot{\gamma}$ . At an even lower  $Q$ , the interface between the suspensions and the suspending fluid becomes unstable and displays nonplanar longitudinal variations, which prevents us from measuring the width ratio of the two fluids accurately. Such instability may indicate nonzero normal stress differences in bacterial suspensions [143, 157, 158].

### 3.2.3 Image Acquisition and Analysis

Florescence microscopy is used to take movies of the microfluidic flows at the center of the channel at  $y = 0$ . Movies are acquired at 30 frames per second (fps) with a sCMOS camera (Andor, Zyla) through an inverted microscope (Nikon, Ti-E) using a 10X objective. Raw images are first processed by a variance filter to enhance the contrast between bacterial suspensions and the suspending fluid (Fig. 3.1b). For each image, we calculate the sum of the pixel intensity in each row and then obtain an intensity profile of the image along the width of the channel ( $z$ ) (Fig. 3.1b, red curve). By fitting the intensity profile with an error function (Fig. 3.1b, white curve), we identify the position of the interface between the two fluids as the reflection point of the error function. This image analysis routine is implemented using a custom Matlab program.

To obtain the flow profiles of suspensions at different  $h$  and  $\dot{\gamma}$ , we add fluorescent

polystyrene (PS) colloids of  $1\text{ }\mu\text{m}$  in diameter into bacterial suspensions. At  $0.001\text{ v\%}$  in the final mixture, the concentration of PS particles is so low that the presence of the particles should not affect the flow of bacterial suspensions. We use fast confocal microscopy to measure suspension flows at different heights above the bottom wall of microfluidic channels away from the side walls. At each height, a movie of  $10\text{--}20\text{ s}$  is taken at  $100\text{ fps}$  using a  $60\text{X}$  objective. The velocity of fluid flows at a certain  $y$ ,  $V(y)$ , is extracted by tracking the motion of colloids in the imaging plane using particle tracking velocimetry (PTV). In addition, we also measure the average velocity of bacteria,  $V_{bac}(y)$ , via particle imaging velocimetry (PIV), where bacteria, instead of colloids, are used as tracer particles. Both the velocity profile of fluid flows and the velocity profile of bacteria along  $y$  can then be compiled from a series of measurements at different heights. The measurements on  $V(y)$  and  $V_{bac}(y)$  yield not only the flow profile of suspensions but also the relative motions between bacteria and the suspending fluid. The disturbance flow  $V_d(y)$  defined below can be obtained as  $V_d(y) = V(y) - V_{bac}(y)$ .

The number of bacteria at each height can also be estimated from these movies through direct counting, which allows us to calculate 2D bacterial density  $n$ .

### 3.3 Results

#### 3.3.1 Confinement Effect

Figure 3.2a shows the relative viscosity of bacterial suspensions,  $\eta/\eta_0$ , as a function of shear rates for channels of different heights. Here,  $\eta$  is the viscosity of bacterial suspensions and  $\eta_0$  is the viscosity of the suspending fluid. For channels with  $h > 60\text{ }\mu\text{m}$ , the flow curves of different heights collapse into a master curve, giving the rheological response of bulk bacterial suspensions. At low shear rates, suspensions show strong shear thickening. When  $\dot{\gamma} < 10\text{ s}^{-1}$ , the viscosity of bacterial suspensions is below that

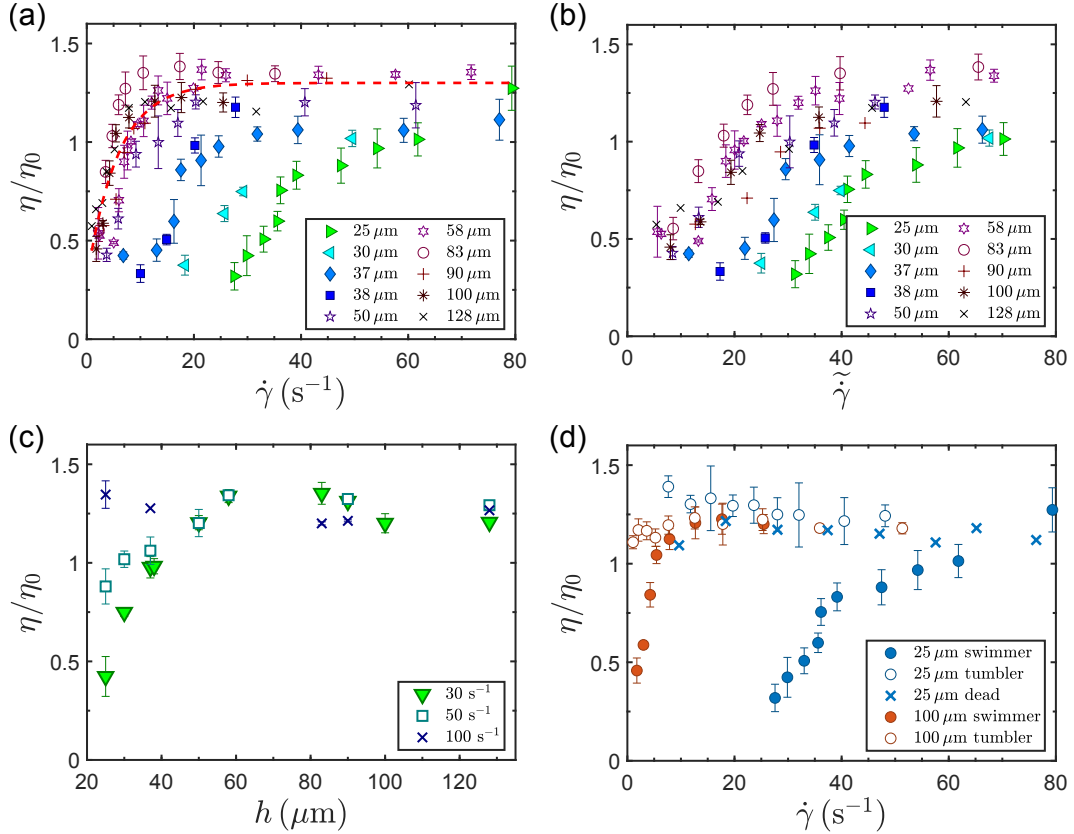


**Figure 3.2: Viscosity of bacterial suspensions under different degree of confinement.** (a)  $\eta/\eta_0$  as a function of shear rates,  $\dot{\gamma}$ , in channels of different heights,  $h$ .  $h$  is indicated in the figure. The dashed line is a fitting for the bulk samples with  $\eta/\eta_0 = 1.3 - \exp(-0.24\dot{\gamma})$ . (b)  $\eta/\eta_0$  as a function of dimensionless shear rates,  $\tilde{\dot{\gamma}}$ , in channels of different  $h$ .  $\tilde{\dot{\gamma}} \equiv \dot{\gamma}h/v$ , where bacterial swimming speed  $v = 22 \mu\text{m}/\text{s}$ . (c)  $\eta/\eta_0$  as a function of  $h$  at different  $\dot{\gamma}$ , which are indicated in the figure. (d)  $\eta/\eta_0$  of suspensions of active swimmers, tumblers, and dead bacteria. Two different heights  $h = 25 \mu\text{m}$  and  $100 \mu\text{m}$  are used.

of the suspending fluid, a defining feature of the rheology of pusher suspensions. At the lowest shear rate of our experiments  $\dot{\gamma} = 1 \text{ s}^{-1}$ , the viscosity is about half of the viscosity of the suspending fluid, quantitatively agreeing with previous experiments [24]. However, for channels with  $h < 60 \mu\text{m}$ , the flow curves separate from each other at low shear rates, indicating a strong confinement effect at a small  $h$ . At high shear rates, the relative viscosity at different heights approaches to a plateau independent of  $h$ . This absence of the confinement effect at high shear rates suggests that the effect is linked to bacterial motility. In the limit of high shear rates, the active stress arising from the hydrodynamic stresslet and the diffusive stress is negligible compared with the passive stress induced by the rigid elongated body of *E. coli* on the fluid [28, 43]. Thus, the viscosity of active suspensions in the limit of high shear rates should be the same as that of suspensions of passive elongated particles of the same shape, which does not show an obvious confinement effect. We also observe weak shear thinning in this regime, presumably arising from the shear-induced alignment of elongated particles [159]. The degree of shear thinning, however, is weaker than that reported in the previous study [24].

We have attempted to rescale the relative viscosity by normalizing the shear rate by the characteristic run-time of bacteria, which determines the diffusive stress of active particles [43]. The dimensionless shear rate  $\tilde{\dot{\gamma}}$  is defined as  $\tilde{\dot{\gamma}} \equiv \dot{\gamma}/f$ , where  $f$  is the tumbling frequency of bacteria. For bulk samples with  $h > 60 \mu\text{m}$ ,  $f \approx 0.5 \text{ Hz}$  is an intrinsic property of bacteria and therefore a constant. Since the relative viscosity has already collapsed together when plotting against  $\dot{\gamma}$ , adding a constant prefactor should not change the quality of data collapsing. For confined samples, the tumbling frequency of bacteria is determined by the system size. In a simple picture,  $f$  should be replaced by  $v/h$ . Although different data sets show better collapse when plotted against  $\tilde{\dot{\gamma}}$ , they are still well separated (Fig. 3.2b). The result suggests that other factor(s) in addition

to the reorientation of bacteria need to be considered in order to fully interpret our experiments on strongly confined samples.

The confinement effect is even better illustrated in Fig. 3.2c, where the relative viscosity of bacterial suspensions as a function of channel heights is directly plotted at three different shear rates. At the lowest shear rate, the viscosity increases by a factor of three when the confinement length increases from 25 to 60  $\mu\text{m}$ . Above  $h \approx 60 \mu\text{m}$  comparable with the run length of bacteria, the viscosity plateaus and becomes independent of  $h$ . At the moderate shear rate, the increasing trend is less pronounced. At the highest shear rate, the height dependence completely vanishes. To further demonstrate that the confinement effect arises from bacterial motility, we also conduct control experiments comparing the viscosity of suspensions of active swimmers, tumblers, and immobile bacteria. The viscosities of the three types of suspensions are examined in both bulk and confined systems. Figure 3.2d shows that the viscosity of active swimmers exhibits strong shear thickening in both bulk and confined channels, whereas the viscosity of tumblers and immobile bacteria weakly depends on shear rates. As expected, the viscosity reduction originates from the motility of bacteria. More importantly, the confinement effect disappears for suspensions of tumblers and immobile bacteria. The flow curves at  $h = 100 \mu\text{m}$  and  $25 \mu\text{m}$  are quantitatively the same within experimental errors. Hence, we confirm that the motility of bacteria is the direct cause of the confinement effect.

### 3.3.2 Microscopic Dynamics

Hydrodynamic interactions between bacteria and external shear flows can profoundly modify the swimming behaviors of bacteria, leading to interesting phenomena such as rheotaxis [160], heterogeneous bacterial distributions [161], and upstream swimming along confining walls [162–165]. These microscopic bacterial dynamics may strongly

affect the macroscopic rheology of bacterial suspensions. Hence, we also investigate the microdynamics of bacterial suspensions at microscopic scales in microfluidic channels of different heights.

### Velocity Profiles

First, we measure the velocity profiles of bacterial suspensions along  $y$  in microfluidic channels of different heights at low shear rates (Fig.3.3), where the confinement effect is most pronounced. Near the center of the channels, the velocity profiles of fluid flows,  $V(y)$ , are parabolic, consistent with the Hagen-Poiseuille law. However, near the bottom and top walls, the velocity of fluid flows measured from passive colloidal tracers noticeably deviates from the parabolic profile and is significantly higher than the velocity of bacteria,  $V_{bac}(y)$ . Thus, there exists a boundary layer near the confining walls, where bacteria swim against the background flow and exhibit strong relative motions. The thickness of these boundary layers, where strong relative motions of bacteria can be observed, is about  $5 \mu\text{m}$ , independent of  $h$ . Thus, as  $h$  decreases, the boundary layer plays a more important role in suspension flows. Interestingly, the velocity profiles of bacteria,  $V_{bac}(y)$ , remain parabolic for different  $h$ , satisfying the no-slip condition at the walls. Such a feature is crucial for *E. coli* in natural environments, where they need to maintain their locations in the lower intestine of their hosts against expelling flows.

### Upstream Swimming Bacteria

The difference in the velocity profiles of fluid flows and bacteria indicates the existence of boundary layers near the confining walls consisting of upstream swimming bacteria against imposed shear flows, an observation in agreement with previous experiments [162, 165] and simulations [163, 164, 166, 167]. To illustrate the phenomenon directly, Fig. 3.4a shows the trajectories of colloidal and bacterial tracers near the bottom wall.

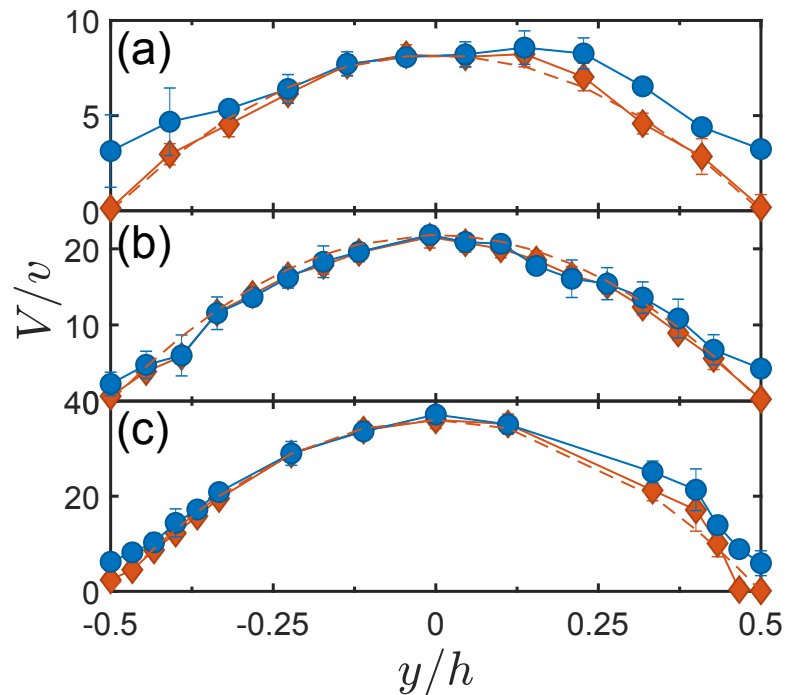


**Figure 3.3: Velocity profiles of fluid flows and bacteria at different channel heights.** The blue disks are the velocity profiles of fluid flows measured from passive colloidal tracers. The orange diamonds are the velocity profiles of bacteria measured from bacteria. (a)  $h = 30 \mu\text{m}$  and  $\dot{\gamma} = 25 \text{ s}^{-1}$ , (b)  $h = 50 \mu\text{m}$  and  $\dot{\gamma} = 36 \text{ s}^{-1}$ , (c)  $h = 83 \mu\text{m}$  and  $\dot{\gamma} = 38 \text{ s}^{-1}$ . The dashed lines are the fittings of parabolic profiles. Velocity is normalized by bacterial velocity  $v = 22 \mu\text{m/s}$ .

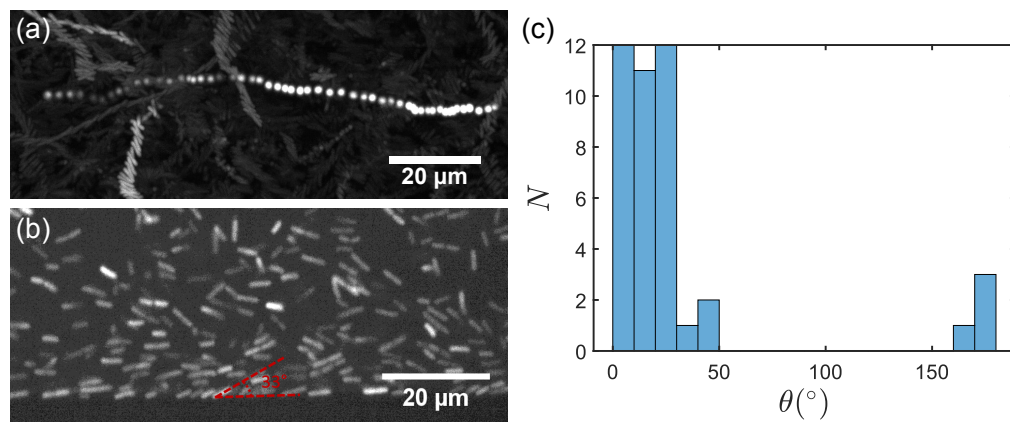


Figure 3.4: **Upstream swimming bacteria in a microfluidic viscometer.** (a) Trajectories of a passive colloidal tracer and bacteria. The maximal intensity of 54 frames over a time interval of 17.5 s is projected onto a single image to show the trajectories. While the spherical passive tracer is transported by the fluid flow, many bacteria swim against the flow and exhibit only transverse motions. The channel height  $h = 30 \mu\text{m}$ . The shear rate  $\dot{\gamma} = 24 \text{ s}^{-1}$ . (b) Bacteria near the side wall, locating at the bottom of the image. The channel height  $h = 50 \mu\text{m}$ . The shear rate  $\dot{\gamma} = 7.8 \text{ s}^{-1}$ . The direction of the flow is indicated in the images. The orientation of a single bacterium at  $\theta = 33^\circ$  is indicated. (c) Distribution of the orientation of bacteria next to the side wall. The total number of bacteria counted is 42.

The relative motions between bacteria and the background fluid can be clearly identified. The orientation of bacteria against the bottom and top walls can be estimated from the images showing the bacteria near the side walls (Fig. 3.4b). We plot the distribution of the orientation angle of bacteria against the side walls (Fig. 3.4c), which strongly biases toward acute angles with the mean at 20°.

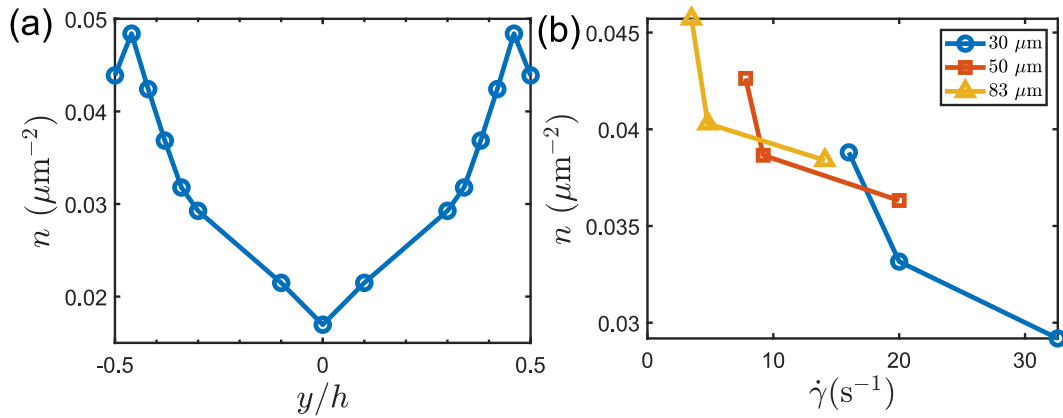


Figure 3.5: **Bacterial density distribution in microfluidic channels.** (a) Bacterial density across a channel of height  $h = 50 \mu m$ . The shear rate is  $\dot{\gamma} = 7.8 s^{-1}$ . (b) Bacterial density at the bottom wall as a function of  $\dot{\gamma}$ . Different symbols are from channels of different heights,  $h$ , which are indicated in the figure.

### Bacterial Density Distributions

Finally, we also measure the number density of bacteria in microfluidic channels. Figure 3.5a shows the density distribution of bacterial suspensions along  $y$  at a low shear rate. In consistency with previous experiments [162, 168, 169], we find that bacteria accumulate near the confining walls, an effect arising from the coupling between self-propulsion and steric interactions [167]. Hydrodynamic interactions between bacteria and solid surfaces also enhance the accumulation [168]. Furthermore, Fig. 3.5b shows bacterial concentrations at the bottom confining wall as a function of shear rates. The

concentration decreases with increasing shear rates, leading to more uniform density profiles at high shear rates [167].

## 3.4 Discussion and Conclusion

### 3.4.1 Data Analysis

We perform a simple data analysis to better illustrate the origin of the unusual rheology of bacterial suspensions under confinement. First, we shall recapitulate the calculation for the viscosity ratio of the two miscible fluids in a bulk Y-shaped microfluidic channel. Within the Hele-Shaw approximation, the average velocities of fluid 1 and fluid 2 over the channel height  $y$  are given by [154]

$$\langle V_j \rangle = -\frac{1}{12} \frac{h^2}{\eta_j} \frac{\partial P}{\partial x} \quad (3.1)$$

where  $\partial P/\partial x$  is the pressure gradient driving the flow, which is the same in the two branches.  $j$  can be either 1 or 2, denoting different fluids 1 and 2.  $\eta_1$  and  $\eta_2$  are the viscosity of fluid 1 and fluid 2, respectively. Thus,

$$\langle V_1 \rangle \eta_1 = \langle V_2 \rangle \eta_2 \quad (3.2)$$

In addition, the flow rates of the two fluids are the same,

$$\langle V_1 \rangle d_1 h = \langle V_2 \rangle d_2 h \quad (3.3)$$

Combining Eqs. 3.2 and 3.3, we obtain the desired relation for the viscometer

$$\frac{d_1}{d_2} = \frac{\eta_1}{\eta_2}$$

In our experiments, fluid 1 is a bacterial suspension with an unknown viscosity of  $\eta$ . As the reference fluid, fluid 2 is the suspending fluid with a known viscosity  $\eta_0$ . The relative viscosity of the bacterial suspension is thus [24]

$$\frac{\eta}{\eta_0} = \frac{d_1}{d_2} \quad (3.4)$$

where  $d_1$  is the width of the bacterial suspension and  $d_2$  is the width of the suspending fluid. For a confined bacterial suspension, there should be an extra contribution to the fluid flow arising from the coupling between bacterial motility and the confining surfaces of the channel. We assume this extra disturbance flow linearly superposes to the pressure-driven Poiseuille flow at low Reynolds numbers:

$$\langle V \rangle = -\frac{1}{12} \frac{h^2}{\eta_b} \frac{\partial P}{\partial x} + \langle V_d \rangle \quad (3.5)$$

Here,  $\langle V_d \rangle$  is the average strength of the boundary-driven disturbance flow.  $\eta_b$  is the viscosity of bulk bacterial suspensions without the influence of system boundary. Numerically, we obtain  $\eta_b$  by fitting our experiments on bulk samples with  $h > 60 \mu\text{m}$  using an exponential function, which gives  $\eta_b/\eta_0 = 1.3 - \exp(-0.24\dot{\gamma})$  (Fig. 3.2a). In bulk samples, the disturbance flow from the boundary is negligible with  $\langle V_d \rangle \approx 0$ . The non-trivial rheology results from the active hydrodynamic stresslets and diffusive stresses [43, 54]. We shall focus on the confined systems in our analysis below, where boundary-driven disturbance flows dominate. Note that since the characteristic shear rate at which shear thickening occurs in bulk samples is  $1/0.24 \approx 4 \text{ s}^{-1}$  smaller than the lowest shear rate we can achieve in confined channels when  $h < 60 \mu\text{m}$  (Fig. 3.2a), the shear thickening effect of bulk samples should not strongly affect our analysis of  $\langle V_d \rangle$  below. Quantitatively similar results on  $\langle V_d \rangle$  are indeed obtained if we fix  $\eta_b/\eta_0 = 1.3$  in Eq. 3.5, i.e., the high-shear-rate plateau of the relative viscosity. With the assumption

of Eq. 3.5 as well as the average velocity of the suspending fluid, which is Newtonian following

$$\langle V_0 \rangle = -\frac{1}{12} \frac{h^2}{\eta_0} \frac{\partial P}{\partial x} \quad (3.6)$$

we have

$$\langle V \rangle = \frac{\eta_0}{\eta_b} \langle V_0 \rangle + \langle V_d \rangle \quad (3.7)$$

Furthermore, the flow rates in the two fluids should be the same as before,

$$\langle V \rangle d_1 h = \langle V_0 \rangle d_2 h$$

which leads to

$$\langle V \rangle = \frac{\eta_0 d_1}{\eta_b d_2} \langle V_0 \rangle + \langle V_d \rangle$$

Experimentally, the relative viscosity,  $\eta/\eta_0$ , is measured via the width ratio of the two fluids. Hence, by definition,

$$\frac{\eta}{\eta_0} \equiv \frac{d_1}{d_2} = \frac{\eta_b}{\eta_0} \left[ 1 - \frac{\langle V_d \rangle}{\langle V \rangle} \right] \quad (3.8)$$

Finally, applying the definition of the characteristic shear rate,

$$\dot{\gamma} \equiv \frac{6Q}{d_1 h^2} = \frac{6\langle V \rangle}{h}$$

we have

$$\frac{\eta}{\eta_0} = \frac{\eta_b}{\eta_0} \left[ 1 - \frac{6\langle V_d \rangle}{h \dot{\gamma}} \right] \quad (3.9)$$

We fit our experimental results using the above equation, where  $\eta_b/\eta_0$  is given by the exponential function for bulk samples as discussed above.  $\langle V_d \rangle$  is taken as a fitting parameter, which we assume is independent of  $\dot{\gamma}$ . We find that  $\langle V_d \rangle$  decreases with

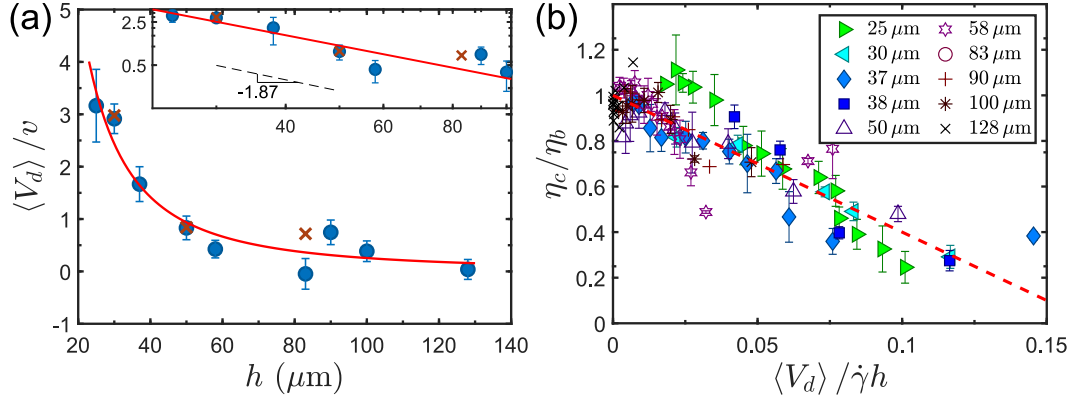


Figure 3.6: **Scaling of relative viscosity.** (a) The average velocity of the boundary-driven disturbance flows,  $\langle V_d \rangle$ , as a function of the channel height,  $h$ . Blue disks are from the fitting of Eq. 3.9. Red crosses are from the direct velocity-profile measurements (Fig. 3.3).  $\langle V_d \rangle$  is normalized by the swimming speed of bacteria  $v = 22 \mu\text{m/s}$ . The solid red line is a power-law fitting,  $\langle V_d \rangle \sim h^{-1.87}$ . Inset shows the same data in a log-log plot. (b) Viscosity ratio,  $\eta/\eta_b$ , as a function of inverse dimensionless shear rates,  $\langle V_d \rangle/h\dot{\gamma}$ .  $h$  is indicated in the plot. The dashed line indicates  $y = 1 - 6x$ , the prediction of Eq. 3.9.

increasing  $h$  and shows an approximate power law scaling,  $\langle V_d \rangle \sim h^{-\alpha}$ , with  $\alpha = -1.9 \pm 0.6$  (Fig. 3.6a).  $\langle V_d \rangle$  obtained from the fitting quantitatively agrees with direct measurements based on the velocity profiles (Fig. 3.3), where the disturbance flow can be extracted by subtracting the parabolic bacterial flow from the total fluid flow,  $V_d(y) = V(y) - V_{bac}(y)$ . Using  $\langle V_d \rangle$ , a good collapse of data can be achieved by plotting the viscosity ratio  $\eta/\eta_b$  versus the inverse dimensionless shear rate  $\langle V_d \rangle/h\dot{\gamma}$  (Fig. 3.6b). A linear trend predicted by Eq. 3.9 can be clearly identified. We shall discuss the possible origin of  $\langle V_d \rangle$  below.

### 3.4.2 Effect of Active Hydrodynamic and Diffusive Stresses

Using a kinetic theory with active hydrodynamic stresslets, Alonso-Matilla and co-workers studied the effect of confinement on the rheology of bacterial suspensions [54].

Since bacterial density is higher near the confining walls (Fig. 3.5a), as the system size reduces, the regions with higher bacterial density near the walls start to overlap near the center of microfluidic channels. As a result, relatively fewer bacteria are subject to the high shear near the walls, mitigating the effect of shear alignment and viscosity reduction. Hence, the viscosity of confined bacterial suspensions was predicted to be higher than that of bulk suspensions at the same shear rate, which is opposite to our experimental observations.

The effect of diffusive stresses in confined systems is more complicated. The hydrodynamic stress from active stresslet scales as  $\sigma^H \sim n\zeta va$ , which therefore does not directly depend on the confinement except via bacterial density  $n$  as discussed above. Here,  $\zeta$  is the drag coefficient and  $a$  is the characteristic size of the bacteria. In comparison, the diffusive stress scales as  $\sigma^S \sim n\zeta vL$ , where  $L$  is the run length of bacteria [43]. In confined systems, bacterial run length is determined by the size of a system. In a simple picture,  $L$  should be replaced by the size of system  $h$  as  $\sigma^S \sim n\zeta vh$ , which gives rise to a direct system-size dependence. The magnitude of  $\sigma^S$  decreases with increasing confinement. Whether the viscosity of bacterial suspensions increases or decreases with  $h$  depends on the sign of  $\sigma^S$ . In the low Peclet number (Pe) limit where the diffusive stress dominates,  $\sigma^S$  is negative. As a result, when  $h$  decreases, the magnitude of  $\sigma^S$  decreases and the viscosity of suspensions increases with the decreasing  $h$ , opposite to our experiments. However, for intermediate Pe that is more relevant to our experiments,  $\sigma^S$  becomes positive (see Fig. 2 of Ref. [43]), which leads to the reduction of viscosity in confined systems, consistent with our experiments. Nevertheless, for suspensions of spherical particles, where the analytical solution of the viscosity is available (Eq. 5 of Ref. [43]), the decrease of viscosity is less than a factor of 1.1 when we decrease  $h$  from 50 to 25  $\mu\text{m}$  even at the optimal shear rates of  $2.1 \text{ s}^{-1}$  that leads to the largest viscosity reduction. In comparison, the viscosity decreases by more than a factor of 3 over the

same range of  $h$  in our experiments. Although the analytical solution for suspensions of active ellipsoids appropriate for the bacteria is not available, numerical solutions show that the magnitude of  $\sigma^S$  of active ellipsoids is smaller than that of active spheres [43]. Hence, we expect that the effect of the confinement-induced viscosity reduction is even weaker for suspensions of active ellipsoids. This conclusion is supported by the failure of our attempt to collapse data using a dimensionless shear rate with the characteristic run-time of bacteria (Fig. 3.2b). Thus, other factor(s) need to be considered to fully explain the experimental observations.

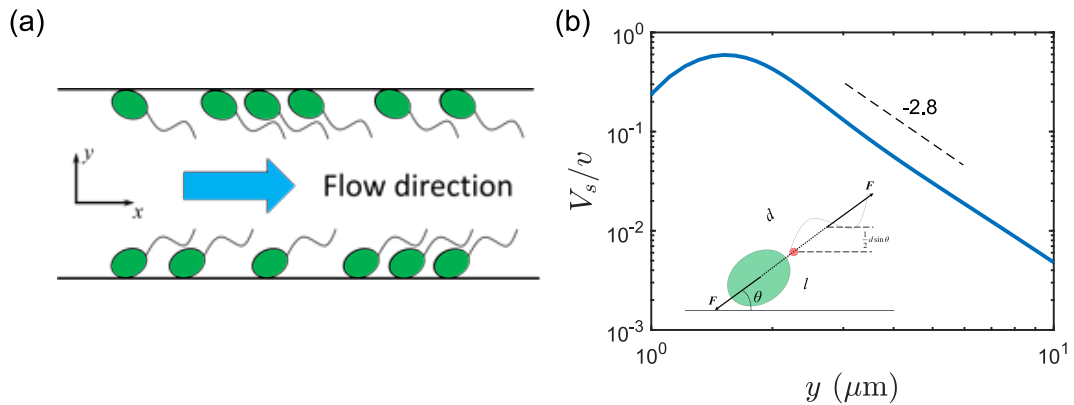


Figure 3.7: **Boundary-layer upstream swimming bacteria model.** (a) Schematic of boundary-layer upstream swimming bacteria model. (b) Velocity induced by a single dipole,  $V_s$ , as a function of the distance to a flat wall,  $l$ . The dashed line indicates a power-law scaling  $V_s \sim l^{-2.8}$ . The inset shows the force dipole of a single bacterium next to the wall with all relevant parameters defined in the main text. The pink disk indicates the center of the force dipole, whereas the blue disks indicate the locations of the upper and lower Stokeslets.

### 3.4.3 Effect of Upstream Swimming Bacteria near Boundaries

A possible origin of  $\langle V_d \rangle$  is the boundary layer of upstream swimming bacteria. To estimate their effect, we numerically calculate  $\langle V_d \rangle$  by assuming a smectic layer of upstream swimming bacteria in a 2D channel with a line density  $n$  randomly distributed along the

top and bottom walls (Fig. 3.7a). Since a bacterium is force-free at low Reynolds numbers, the far-field disturbance flow induced by the bacterium is a hydrodynamic dipolar flow. The flow of a single force dipole near the walls can be constructed by superposition of two Stokeslets of strength  $F$  at position  $\mathbf{r}_0 + \mathbf{u}d/2$  and  $\mathbf{r}_0 - \mathbf{u}d/2$ , respectively, where  $\mathbf{r}_0 = (x_0, y_0)$  is the center of the force dipole (Fig. 3.7b inset). We fix  $y_0$  at 1  $\mu\text{m}$  away from the walls in our calculation. The classical solution of a Stokeslet near a wall is used in this construction [170], so that the disturbance flow satisfies both the no-penetration and the no-slip boundary conditions at the closest wall.  $d = 2.2 \mu\text{m}$  is the distance between the two Stokeslets in a force dipole obtained from experiments [117].  $\mathbf{u}$  indicates the direction of the force dipole, which forms an acute angle  $\theta$  against the imposed shear flow. We choose  $\theta = 20^\circ$ , the mean angle of bacterial orientation from our experimental observations. Other acute angles lead to qualitatively similar results.  $F$  is related to bacterial swimming speed  $v$  through  $F = \zeta v$  with  $F \approx 0.43 \text{ pN}$  for *E. coli* [117]. The disturbance flow is translationally invariant along  $x$  for infinite large systems. In our calculation, we set the system size to be 1 mm in  $x$ , much larger than the average spacing between dipoles. The disturbance flow is then obtained near the center of the system. Specifically, we compute the x-component disturbance flow,  $V_d(y)$ , at a fixed  $x$  defined as  $x = 0$ . All the results are averaged over 100 different random configurations. To avoid the singularity at  $x = 0$ , we exclude those configurations where the locations of the Stokeslets fall in  $x \in [-10 \text{ nm}, 10 \text{ nm}]$ . A cutoff,  $l_c$ , in  $y$  can be further chosen based on  $\int_{-h/2}^{-h/2+l_c} V_d(y) dy = 0$ , below which the near-field bacterial flow is important and the dipole-flow approximation of our simple model breaks down.  $l_c \sim 1.4 \mu\text{m}$ , slightly higher than the location of the upper Stokeslet.

For a single bacterium near the wall, the disturbance flow decays as  $V_s \sim l^{-2.8}$ , faster than the decay of a dipolar flow in bulk, where  $l$  is the distance away from

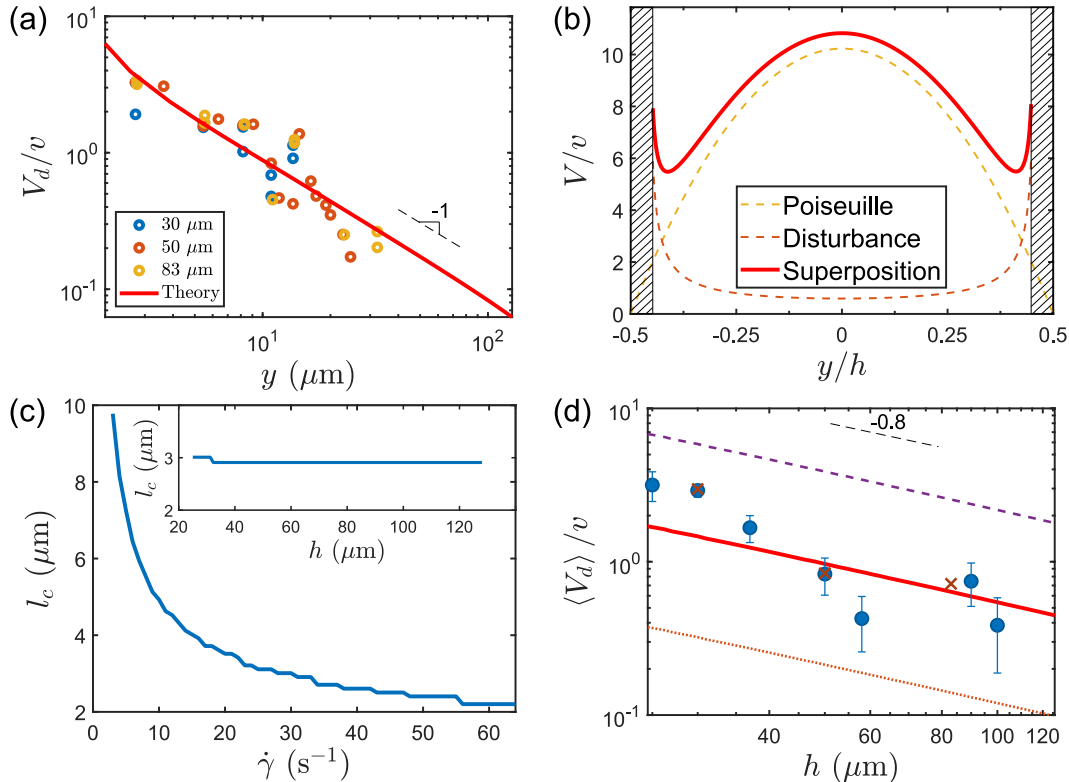


Figure 3.8: **Compare boundary-layer model with experimental data.** (a) Velocity profile induced by a line of randomly distributed dipoles at dipolar line density  $n = 2 \mu\text{m}^{-1}$ . Symbols are from experiments at different channel heights, which are indicated in the figure. The dashed line indicates a power-law scaling  $V_d \sim l^{-1}$ . (b) Velocity profiles in a channel of height  $h = 30 \mu\text{m}$  and shear rate  $\dot{\gamma} = 30 \text{s}^{-1}$ . The brown dashed line is the disturbance velocity profile,  $V_d(y)$ . The yellow dashed line is the parabolic Poiseuille flow. The red solid line is the superposed velocity profile,  $V(y)$ . The shaded regions are within the cutoff  $l_c$ . (c) Thickness of the boundary layer,  $l_b$ , versus  $\dot{\gamma}$  with  $h = 30 \mu\text{m}$  and  $n = 2 \mu\text{m}^{-1}$ . Inset:  $l_c$  as function of  $h$  with  $\dot{\gamma} = 30 \text{s}^{-1}$ . (d) The average disturbance flow velocity  $\langle V_d \rangle$  as a function of  $h$  at different bacterial densities. Symbols are from experiments in Fig. 6a. Bacterial density:  $n = 0.2 \mu\text{m}^{-1}$  (brown dotted line),  $1.0 \mu\text{m}^{-1}$  (red solid line) and  $4 \mu\text{m}^{-1}$  (purple dashed line). The black dashed line indicates a power-law scaling  $\langle V_d \rangle \sim h^{-0.81}$ . All the velocities are normalized by the swimming speed of bacteria  $v = 22 \mu\text{m/s}$ .

the wall (Fig. 3.7b). Collectively, the disturbance flow from the smectic layer of randomly distributed bacteria decays much slower as  $V_d \sim l^{-1}$ , quantitatively agreeing with our velocity-profile measurements (Fig. 3.8a). By comparing the experiments and calculation, we obtain the effective dipole density at the wall  $n = 2 \mu\text{m}^{-1}$ . Near the center of the channel away from the walls,  $V_d$  is small. The fluid is dominated by the pressure-driven Poiseuille flow and is approximately parabolic in shape, consistent with our experiments (Fig. 3.8b). We estimate the thickness of the boundary layer,  $l_b$ , by the location where the superposed velocity profile shows a minimum. Below  $l_b$ , the disturbance flow from the upstreaming bacteria dominates the Poiseuille flow. We find that  $l_b$  is a weak function of  $h$  over the range of  $\dot{\gamma}$  in our experiments (Fig. 3.8c inset), confirming that the disturbance flow induced by the upstreaming bacteria is confined within a boundary layer. Moreover,  $l_b$  decreases with increasing  $\dot{\gamma}$  (Fig. 3.8c). At high  $\dot{\gamma}$ , the boundary layer becomes insignificant, consistent with our observation (Fig. 3.2c). At  $\dot{\gamma} = 30 \text{ s}^{-1}$ ,  $l$  is about  $3 \mu\text{m}$ , qualitatively agreeing with our observations.

Finally, the average strength of the disturbance flow,  $\langle V_d \rangle$ , is calculated by integrating the disturbance velocity profile over the channel height.  $\langle V_d \rangle$  as a function of  $h$  is shown in Fig. 3.8d. At a fixed  $h$ ,  $\langle V_d \rangle$  increases linearly with bacterial density. More importantly,  $\langle V_d \rangle$  decreases with  $h$ , agreeing with our experimental observations qualitatively (Fig. 3.8d). The best fitting gives  $n = 1.0 \mu\text{m}^{-1}$ , comparable with the fitting from  $V_d(l)$ . Numerically, we find  $\langle V_d \rangle \sim h^{-0.81}$ , with a scaling exponent smaller than that of the experiments. Although the disturbance flow induced by a single bacterium near the wall decays as  $l^{-2.8}$ , too weak to influence the macroscopic fluid flows driven by pressure gradients, the formation of the boundary layer allows such a weak effect from individual bacteria to add coherently, which strongly modifies the fluid flows of bacterial suspensions in confined channels. Hydrodynamic simulations have further

shown that coherent structures of active particles including layers of upstream swimming bacteria emerge in confined geometries when the run length of active particles exceeds the confinement length [163]. Such a finding provides a possible explanation why the confinement effect is most obvious when the system size is comparable or below the run length of bacteria in our experiments.

Although the velocity profiles and the power-law scaling can be qualitatively explained by the presence of the boundary layers of upstream swimming bacteria, there are still open questions on the hypothesis. First, at the experimental bacterial density of  $0.2 \mu\text{m}^{-1}$ , the strength of the disturbance flow  $V_d$  calculated from our simple model is about 5 times weaker than that from our experiments (Fig. 3.8d). Such a discrepancy may be accounted for by considering a finite thickness of the boundary layer and including multiple bacterial layers near the confined walls. Second, the calculated velocity profile oscillates strongly within the cutoff length of the boundary layer due to the singular nature of the dipole flow (Fig. 3.8b). The dipole flow describes the far-field flow of the bacteria quantitatively but provides only a qualitative trend in the near field [117, 171]. Thus, to quantify the disturbance flow within the boundary layer close to the bacteria, detailed understanding of the near-field bacterial flow is needed. Third, the upstream swimming behavior of bacteria depends on the strength of external flows [165]. Bacterial concentrations next to the walls are also a function of shear rate and system size (Fig. 3.5b). These effects will likely lead to the dependence of  $V_d$  on  $\dot{\gamma}$  and  $h$ , which are not included in our qualitative discussion above. The lack of these dependencies may explain the smaller scaling exponent of  $\langle V_d \rangle(h)$  in our model. Lastly, it is worth noting that both active hydrodynamic and diffusive stresses are still present in confined bacterial suspensions. In the bulk limit, the contribution of the boundary-driven disturbance flow diminishes. Active hydrodynamic stresslets and diffusive stresses become the leading reason for the non-trivial rheology of active

fluids [43, 54]. Thus, their contributions should also be included in formulating a quantitative theory of active fluids under confinement. We hope our simple heuristic model on the upstream swimming bacteria, an effect that is missing in previous theories, can stimulate further theoretical development.

In summary, we experimentally studied the rheology of confined bacterial suspensions using a microfluidic viscometer. A confinement effect was observed at low shear rates, where the viscosity of bacterial suspensions decreases with increasing confinement. We showed that such a confinement effect arises from the interplay between bacterial motility and confining surfaces. A simple analysis was developed to reveal the physical origin of the confinement effect. We proposed that the boundary layers near confining surfaces, where bacteria collectively swim against the imposed shear flows, play a key role in determining the flow structure and the rheology of confined bacterial suspensions. A simple model based on this picture shows a qualitative agreement with our macroscopic rheology and microscopic dynamics measurements. Open questions were finally discussed for future theoretical development. As such, our experiments demonstrate the importance of system boundary on the flow of bacterial suspensions and present a benchmark to verify different models of the rheology of active fluids. The results are also potentially useful in designing new strategies to modify bacterial transport in confined geometries.

## Chapter 4

# The Emergence of Active Turbulence\*

### 4.1 Introduction

Collective motions of biological systems such as bird flocks, fish schools and bacterial swarms are the most vivid examples of the emergent behaviors of active matter [7]. While moving independently at low density, self-propelled units in active matter can move collectively at high density, giving rise to coherent flows at length scales much larger than the size of individual units. In bacterial suspensions, these coherent flows exhibit a chaotic pattern of intermittent vortices and jets, reminiscent of turbulent flows at high Reynolds numbers. Hence, the flows induced by bacterial collective swimming are also known as active or bacterial turbulence [21, 70, 104, 172]. Extensive theoretical and numerical studies have been conducted in understanding the physical principles underlying the nonequilibrium transition between the disordered and the turbulent states in bacterial suspensions [5, 7, 82, 86]. Particularly, kinetic theories have been developed by

---

\*Reproduced in part with permission from (Yi Peng, Zhengyang Liu and Xiang Cheng, “Imaging the emergence of bacterial turbulence using light-powered *Escherichia coli*”, *arXiv e-print*).

extending the classic models of suspensions of passive rod-shaped particles [82, 86, 173]. The theories consider the probability distribution of the position and orientation of bacteria based on a Smoluchowski equation, where a bacterium is modeled as a rigid rod exerting a pusher-type force dipole on the suspending fluid. In addition to self-propulsion, the motion of bacteria is further coupled with a mean-field background Stokes flow, driven by an average active dipolar stress as well as more conventional particle-induced viscous stresses. Using the kinetic theories, Saintillan and Shelley first showed that a long wavelength hydrodynamic instability drives the transition to active turbulence in suspensions of pusher swimmers [66, 81, 86, 174]. The transition kinetics was further studied beyond the linear regime by numerically solving kinetic equations [66] and simulations of self-propelled rods [92]. By incorporating the effect of tumbling and rotational diffusion in the kinetic theories, Subramanian and Koch independently showed that the isotropic disordered state of bacterial suspensions becomes unstable above a threshold concentration in the bulk limit [82, 175]. The threshold concentration increases with the random reorientation and decreases with the swimming activity of bacteria. In general, the kinetic theories assume long-range hydrodynamic dipolar interactions between bacteria and are therefore strictly valid only for dilute suspensions. Nevertheless, the onset of bacterial collective swimming is typically observed at intermediate to high concentrations where steric interactions are supposed to be important [140, 176, 177], raising the question on the relative importance of hydrodynamic versus steric interactions in the formation of bacterial turbulence. Indeed, simulations and models with steric interactions have also been developed, which successfully predicted the rise of collective motions both with hydrodynamic interactions [176, 177] and without [178, 179]. Although steric interactions have been shown to play a leading role in bacterial collective swimming in 2D or quasi-2D systems such as Hele-Shaw cells with two confining walls [98, 180] and bacterial monolayers on agar substrates [94, 181], it is still far from clear what is the

dominant interaction leading to bacterial turbulence in 3D suspensions.

In comparison with the theoretical development, definitive experiments on bacterial suspensions that can quantitatively verify theoretical predictions are still few and far between [82,86]. Pioneering experiments on suspensions of *Bacillus subtilis* first showed the emergence of bacterial turbulence at high concentrations in absence of bioconvection and chemotaxis [20,23,74,140,182]. Various physical properties of bacterial turbulence such as density fluctuations [23], coherent and defect flow structures [83,141,183,184] and mass and momentum transports [1,25,30,35] have been subsequently studied. While most of these studies focused on the rise of bacterial turbulence with increasing bacterial concentrations, few experiments have considered other factors important for bacterial turbulence such as the swimming speed of bacteria [83,183] and the presence of defective immobile bacteria. A systematic mapping of the phase diagram of 3D bacterial flows over a large control parameter space is still lacking. Such an experimental phase diagram is essential to verify the quantitative prediction of the kinetic theories. Particularly, the study of the effect of doping immobile bacteria on the phase dynamics will provide strong evidence to resolve the controversy over the dominant interaction responsible for collective swimming in 3D suspensions of microorganisms [176,177]. Increasing the ratio of immobile to mobile bacteria in a suspension of fixed total bacterial concentration would proportionally reduce the active stress and thus suppress the hydrodynamics-driven collective motion. On the contrary, adding immobile bacteria to a suspension with a fixed concentration of mobile bacteria would promote steric interactions due to the rigid rod-shaped body of immobile bacteria and therefore enhance the collective motion if steric interactions are the leading cause of bacterial turbulence.

Moreover, the kinetic pathway towards the collective motion of swimming microorganisms remains largely unexplored. The kinetics of a phase transition affects both the transition rate and the structure of intermediate states and is of importance in

understanding the phase dynamics of equilibrium systems [185]. It plays a key role in distinguishing first-order and second-order phase transitions. Kinetics is equally important in a nonequilibrium phase transition, which can reveal not only the nature of the transition but also the missing link between the rise of the macroscopic order and the microscopic interparticle interaction. Hence, resolving the route to bacterial turbulence—a premier example of collective motions—addresses the central question in active matter: how do random self-propelled units self-organize into large-scale dynamic structures?

Here, we aim to address the above open questions. Our experiments provide not only the most comprehensive phase diagram of the flow of 3D bacterial suspensions heretofore, but also the detailed characterization of the kinetic route of the bacterial turbulent transition. Our experimental phase diagram quantitatively agrees with the kinetic theories, as well as our simple hydrodynamic model balancing dipolar interactions and rotational diffusion of bacteria. By further examining the effect of doping immobile bacteria on the phase dynamics, we show unambiguously that hydrodynamic interactions dominate the formation of collective swimming in 3D bacterial suspensions. Moreover, our kinetic measurements reveal an unexpected kinetic pathway near the phase boundary in analogy of the nucleation and growth process in equilibrium phase transitions and confirm the existence of a long-wavelength instability deep inside the turbulent phase. Together, our experiments validate the basic assumption of the kinetic theories and corroborate the principal predictions of the theories on the transition point and the mode of instability. Furthermore, our study uncovers new kinetic features of the bacterial turbulent transition and sheds new light on the nature of the nonequilibrium phase transition in active microbiological systems. These findings open new questions for future experimental and theoretical development.

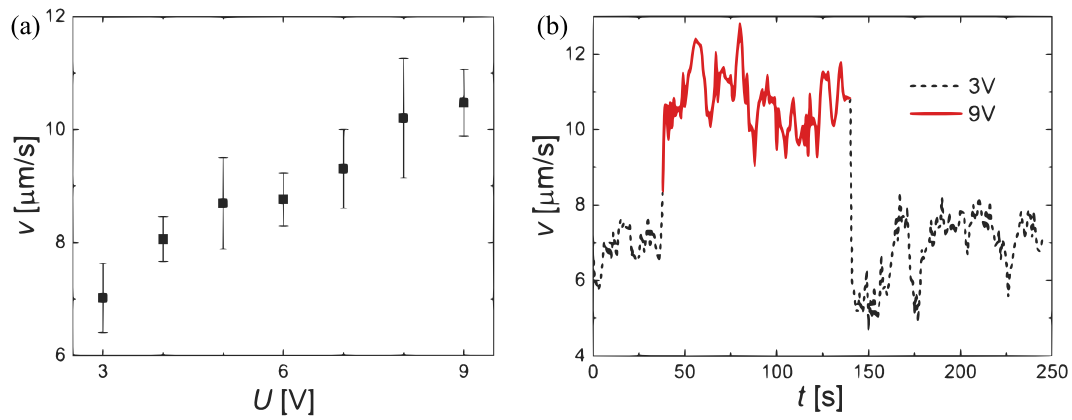


**Figure 4.1: Motility of light-powered bacteria.** (a) Swimming speeds of the light-powered bacteria at different light intensities. The light intensity is tuned by setting the voltage of the illuminating lamp from 3 V up to 9 V. The average swimming speeds and the error bars are obtained by measuring tens of bacteria at a low bacterial volume fraction of  $\phi = 1.8 \times 10^{-4}$  away solid boundaries. The measurements are taken 2 min after setting the light intensity, sufficient for the motility of bacteria reaching the steady state. (b) Temporal evolution of bacterial speed when the light intensity is changed. The velocity is averaged over all the bacteria in the field of view within a time interval of 1 s ( $\sim 100$  bacteria). The video is taken at 30 frames per second. The response of bacteria to the change of light is fast on the order of seconds.

## 4.2 Methods

### 4.2.1 Bacteria

Three strains of *Escherichia coli* (*E. coli*) are used. (i) A wild-type *E. coli* K-12 strain (BW25113), which executes normal run-and-tumble motion with an average swimming speed  $v = 28.7 \mu\text{m/s}$  [152]. (ii) A “tumbler” strain, which is made by knocking out *cheZ* of a wild-type *E. coli* strain (RP1616). The  $\Delta cheZ$  mutant shows constant tumbling motions. We use tumblers as passive particles. To deactivate the bacteria, we remove the flagella of tumblers by pipetting tumbler suspensions through a narrow pipette tip a few tens of times. (iii) A light-powered *E. coli*, whose swimming speed can be reversibly controlled by light. We introduce a light-driven transmembrane proton pump, proteorhodopsin (PR), to wild-type *E. coli* (BW25113) by transforming the bacteria with plasmid pZE-PR encoding the SAR86  $\gamma$ -proteobacterial PR-variant [110]. The activity of PR is directly correlated with the light intensity. Thus, we can control the swimming speed of bacteria using light of different intensities. The quantitative relation between the light intensity (in terms of the power of the light source) and the average swimming speed of bacteria is measured by tracking the motion of bacteria in dilute suspensions (Fig. 4.1a). The response time of the bacteria is fast within a few seconds after the change of the light (Fig. 4.1b). Note that the highest speed of the light-powered bacteria at high light intensity is about 10 to 11  $\mu\text{m/s}$  (Fig. 4.2c), which is smaller than that of the wild-type strain. Three strains share a similar body plan with the length of the bacterial body  $2a = 2.8 \pm 0.4 \mu\text{m}$  and the radius of  $b = 0.5 \pm 0.2 \mu\text{m}$  based on direct imaging of bacteria, where the errors are the standard errors of the measurements.

All the three strains are cultured using a similar procedure. They are first cultured at 37.0 °C with a shaking speed at 250 rpm for 14-16 hours in terrific broth (TB) culture medium. The saturated culture is then diluted 1:100 in TB culture medium

and grown at 30 °C for 6.5 hours. PR expression is triggered by 1 mM isopropyl  $\beta$ -D-thiogalactoside and 10  $\mu$ M methanolic all-trans-retinal, which are supplemented in the mid-log phase for the synthesis of proteorhodopsin. The bacteria are harvested by gentle centrifugation (800g for 5 min) in the late log phase. After discarding the supernatant, we resuspend bacteria with motility buffer MB (0.01 M potassium phosphate, 0.067 M NaCl, 10 M EDTA, pH 7.0). The suspension is finally washed twice and adjusted to the target volume fraction. Note that the volume fraction of bacteria at the standard concentration of  $n_0$  is  $\phi = 0.0018$ , where  $n_0 = 8 \times 10^8$  cells/ml is the *E. coli* concentration at  $OD_{600} = 1.0$ . To create the mixture of tumblers and swimmers, we separately prepare suspensions of tumblers and swimmers both at the targeted volume fraction. We then mix the two suspensions at a predetermined ratio to control the fraction of active swimmers  $f$ .

#### 4.2.2 Sample Preparation and Video Microscopy

For the wild-type bacteria, oxygen is necessary to maintain the swimming of bacteria. We deposit a 2  $\mu$ l wild-type bacterial suspension on a microscope coverslip, which forms a free suspension-air interface on the top. The droplet is millimetric in the lateral directions ( $x-y$ ) normal to the imaging plane and about 150  $\mu$ m in height ( $z$ ). The coverslip and the suspension are further enclosed in a humid chamber of  $\sim 1000$  mm $^3$  to reduce evaporation as well as perturbation due to ambient air flows. An inverted microscope is used to image bacterial motions 70  $\mu$ m above the coverslip, where the effect of oxygen gradients is weak and bacterial activity is uniform. No system-wide persistent flow associated with aerotaxis is observed in our experiments. The microscopy videos show bacterial flows in the 2D  $x-y$  plane inside the 3D suspension.

For the light-powered bacteria, it is important to shut down the metabolic pathway of aerobic respiration, so that the locomotion of bacteria is solely controlled by the PR

pump. We inject a suspension of light-powered bacteria into a sealed cell of  $18 \times 3 \times 0.17$  mm<sup>3</sup>. For concentrated bacterial suspensions above  $\phi = 0.062$ , bacteria stop swimming after a few minutes in the cell due to the depletion of oxygen. Microscope illumination is then used to switch on/off and control the activity of the PR pump for bacterial swimming. 2D bacterial flows are imaged 80  $\mu\text{m}$  above the bottom wall.

For most of our experiments, 2D flow fields are imaged through an inverted bright-field microscope using a 10 $\times$  (NA 0.3), 20 $\times$  (NA 0.5) or 40 $\times$  (NA 0.6) objectives. The field of view of images ranges from  $640 \times 640 \mu\text{m}^2$  to  $160 \times 160 \mu\text{m}^2$ . To measure the velocity orientational order and the kinetic energy in steady states, one-minute videos are taken 15 minutes after wild-type *E. coli* samples are loaded or 2 minutes after a new light condition is applied to light-powered *E. coli* samples. These times are sufficient for the sample to reach the steady state. Five-minute videos are taken for transition kinetics after light ramping. All the videos are recorded at 30 frames per second by a sCMOS camera. To control bacterial velocity, light intensity is tuned by the voltage of the light source. Three to twelve independent measurements are taken for each set of control parameters of our experiments.

To measure the dynamics of individual bacteria through the turbulent transition, we image fluorescent-labeled *E. coli* with an inverted fast confocal microscope using a 60 $\times$  objective (NA 1.4). The green fluorescent protein expressed in bacteria is excited by a 488 nm laser. The field of view of the images is  $180 \times 120 \mu\text{m}^2$ . Bacterial flows are imaged 10  $\mu\text{m}$  above the coverslip. Five-minute videos are taken at 10 frames per second.

### 4.2.3 Image Processing and Data Analysis

The velocity field of bacterial suspensions is obtained from raw videos using standard Particle Imaging Velocimetry (PIV). For each pair of neighboring frames, the interrogation window size shrinks from  $19.2 \times 19.2 \mu\text{m}^2$  to  $4.8 \times 4.8 \mu\text{m}^2$  in three iterations [186]. The final lattice spacing of the velocity field is  $2.4 \mu\text{m}$ . The velocity field in Fig. 4.2a shows the velocity vectors of every other lattice. To verify the accuracy of PIV, we have also measured the dynamics of bacterial suspensions using Particle Tracking Velocimetry (PTV) on passive colloidal tracers embedded in bacterial suspensions. The PTV results qualitatively agree with the PIV findings on both phase boundary and transition kinetics.

Energy spectra quantify the energy distribution over different length scales,  $\lambda = 2\pi/k$ , where  $k$  is the wavenumber. To obtain energy spectra, we first calculate the Fourier transform of the 2D velocity field  $v_x(x, y)$  and  $v_y(x, y)$  to obtain  $u_k(k_x, k_y)$  and  $v_k(k_x, k_y)$ . The point-wise kinetic energy density in the k-space is then computed  $E(k_x, k_y) = \langle u_k(k_x, k_y)u_k^*(k_x, k_y) + v_k(k_x, k_y)v_k^*(k_x, k_y) \rangle / 2$ , where  $*$  represents the complex conjugate. Finally, the energy spectrum  $E(k)$  is obtained by summing up  $E(k_x, k_y)$  at a constant  $k = (k_x^2 + k_y^2)^{1/2}$ . An alternative way to calculate  $E(k)$  through the Fourier transform of the two-point velocity correlation function  $\langle \vec{v}(\vec{r}_0) \cdot \vec{v}(\vec{r}_0 + \vec{r}) \rangle_{\vec{r}_0}$  yields quantitatively similar results.

To extract bacterial nematic order, we perform Fast Fourier transformation (FFT) on the local regions ( $20 \times 20 \mu\text{m}^2$ ) of confocal images. The FFT patterns are first smoothed with 3 neighboring pixels ( $0.15 \mu\text{m}^{-1}$ ) and then fitted with ellipses. The aspect ratio of the ellipses,  $a/b$ , quantifies the local nematic order of bacteria (Appendix B.4). The average of the aspect ratio is finally taken over the whole field of view,  $F = \langle a/b \rangle$ . To calibrate our method, we show numerically that the anisotropy of the FFT pattern of local regions,  $a/b$ , is approximately linearly proportional to the local nematic order

parameter of bacteria  $S = \frac{1}{N} \sum_{j=1}^N (3 \cos^2 \alpha_j - 1)/2$  within the range of our experiments, where  $\alpha_j$  is the angle between the orientation of bacterium  $j$  with respect to the mean orientation of all the  $N$  bacteria in a local region in 3D.

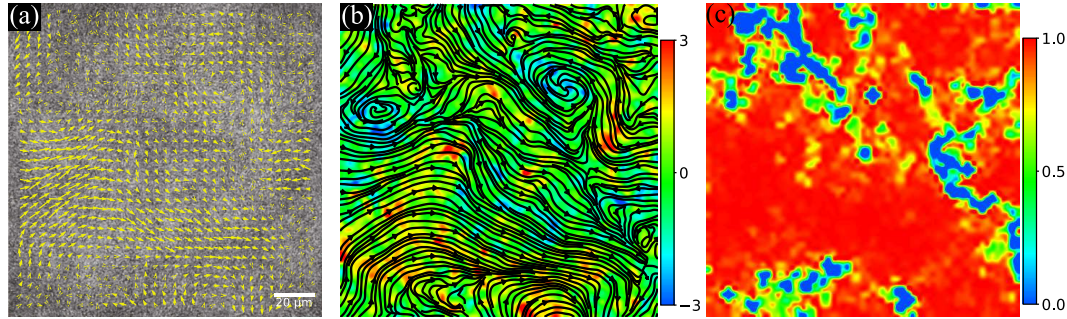


**Figure 4.2: Bacterial turbulence.** (a) The flow field of a suspension of wild-type *E. coli* at volume fraction  $\phi = 0.14$ . The arrows indicate local velocities from PIV. Scale bar: 20  $\mu\text{m}$ . (b) The corresponding streamlines and the vorticity field ( $\omega$ ), highlighting the characteristic features of bacterial turbulence including intermittent jets and vortices. (c) The corresponding velocity orientational correlation field  $c$ . The area fraction of red regions with  $c \geq 0.9$ ,  $M$ , is used to quantify the transition to bacterial turbulence.  $M < 1$  even for this highly turbulent state due to the presence of vortex cores and interstices.

### 4.3 Results

We use *E. coli* as our model bacteria. In order to examine a large control parameter space, three different strains of *E. coli* are used in our experiments, which all share similar body plans (Methods). In addition to a wild-type strain (BW25113), a strain of tumblers with *cheZ* knocked out (RP1616) and flagella removed is used as immobile passive bacteria. Moreover, a light-powered *E. coli* strain (BW25113 with proteorhodopsin, a light-driven transmembrane proton pump [110]) is also used, whose motility can be varied by green light of different intensities (Fig. 4.1). By mixing different strains of bacteria and controlling light intensity, we explore the phase diagram of 3D bacterial

flows spanned by bacterial volume fraction  $\phi$ , the average swimming speed of bacteria  $v$  and the number fraction of active swimmers  $f$ .

#### 4.3.1 Transition to Bacterial Turbulence

The collective motion of bacteria leads to bacterial turbulence with characteristic intermittent jets and whirls, whose lengths and speeds are much larger than those of individual bacteria (Figs. 4.2a and b). To quantify bacterial turbulence, we calculate the orientational correlation of local velocities,  $c_i = \min_{j=1..4}(\hat{v}_i \cdot \hat{v}_j)$ , where  $\hat{v}_i$  is the unit vector along the direction of the local velocity at position  $i$  and  $\hat{v}_j$  is the direction of the velocity in one of its four neighboring boxes adopted in Particle Imaging Velocimetry (PIV). Note that our PIV measures 2D in-plane flows  $\vec{v} = (v_x, v_y)$  in 3D bacterial suspensions (Methods). We identify a local region with high velocity orientational correlation when  $c \geq 0.9$ . The area fraction of these highly correlated regions,  $M$ , is used in our study as the order parameter quantifying the rise of bacterial turbulence (Fig. 4.2c). This choice is similar to that used in previous studies [140]. In addition to the velocity orientational order, we also measure the strength of bacterial flows via kinetic energy per unit mass,  $E = \langle v_x^2 + v_y^2 \rangle / 2$ . Although the definition of kinetic energy density is the same as that used for classical turbulent flows, the inertia of bacterial swimming in our experiments is negligible with the Reynolds number on the order of  $10^{-4}$ .

A transition to bacterial turbulence is observed as we increase bacterial volume fraction,  $\phi$  (Fig. 4.4a). A sharp increase of  $M$  occurs around  $\phi = 0.018$ . The transition point,  $\phi_c$ , is then obtained from the inflection point of the error function fitting of  $M(\phi)$ . The transition to bacterial turbulence at  $\phi_c$  is also coincident with a more gradual increase of  $E$  (Fig. 4.4a). We find similar sharp transitions to bacterial turbulence when increasing  $v$  and  $f$  at fixed  $\phi$  (Fig. 4.4b, c). Particularly, bacterial turbulence is

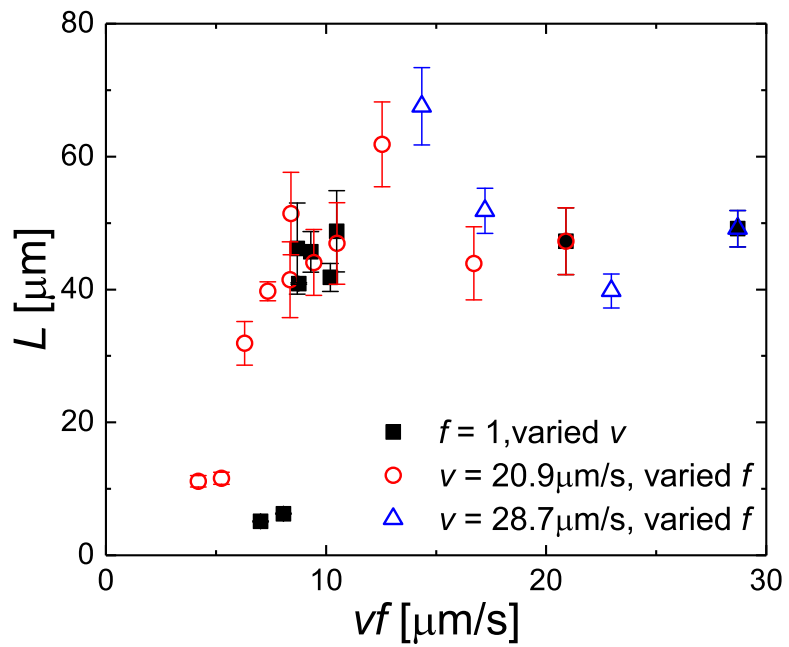


Figure 4.3: The correlation length  $L$  as a function of the product of swimmer fraction and swimming velocity  $fv$ .

observed at  $f = 20\%$  for the mixture of wild-type *E. coli* ( $v = 28.7 \mu\text{m/s}$ ) and immobile bacteria at  $\phi = 0.18$ . Such a low  $f$  demonstrates the robustness of the collective flow of bacterial suspensions, greatly surpassing the state-of-the-art design of active robotic systems [187]. This high tolerance to malfunctioning units likely arises from long-range hydrodynamic interactions, lacking in dry active matter [7].

### 4.3.2 3D Phase Diagram

Systematic measurements over a thousand bacterial samples under different combinations of control parameters yield a full 3D phase diagram of bacterial flows, where bacterial turbulence emerges at large  $\phi$ ,  $v$  and  $f$  (Fig. 4.4d). It should be emphasized that, although the transition to bacterial turbulence has been investigated with increasing  $\phi$  and  $v$  in separate experiments [23, 74, 83, 140, 183], to the best of our knowledge, systematic measurements over such a large parameter space in the same experimental system have not been achieved previously. This comprehensive 3D phase diagram not only allows us to quantitatively verify the theoretical prediction on the transition point, but also sets up a framework for exploring the kinetics of the transition in the next section.

We first estimate the phase boundary between disordered and turbulent phases using a simple hydrodynamic model proposed in Ref. [117], where the pairwise hydrodynamic interaction that promotes local bacterial alignment competes with the rotational relaxation that disorientates bacteria. Although these two competing factors also form the basic ingredients of the kinetic theories [82, 86], this simple model considers the interaction between two bacteria, instead of mean-field particle probability distributions. Specifically, we calculate the rotation of a bacterium in a flow field induced by the swimming of its neighbor at distance  $r$ . A critical distance  $r_c$  is determined when the flow-driven rotation of the bacterium balances the reorientation of the bacterium due to

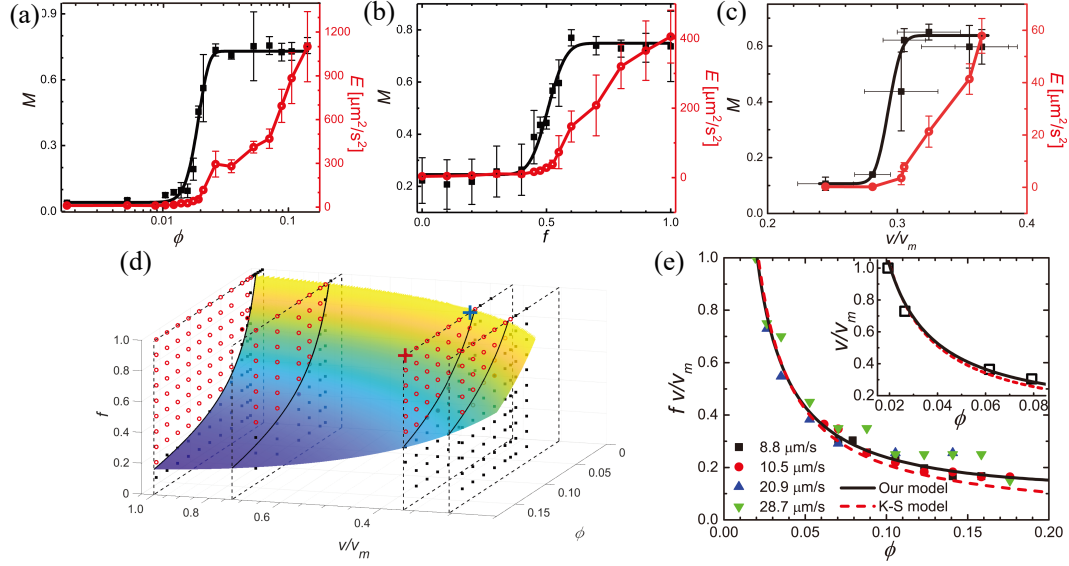


**Figure 4.4: Transition to bacterial turbulence and the phase diagram of 3D bacterial flows.** (a) Velocity orientational order  $M$  and kinetic energy  $E$  as a function of bacterial volume fraction  $\phi$  of wild-type bacteria with swimming speed  $v_m = 28.7 \mu\text{m/s}$  and swimmer fraction  $f = 1$ . Black squares are for  $M$  and red circles are for  $E$ . (b)  $M$  and  $E$  versus  $f$  at fixed  $\phi = 0.053$  and  $v = v_m$ . (c)  $M$  and  $E$  versus  $v$  at  $\phi = 0.11$  and  $f = 1$ .  $v$  is normalized by the swimming speed of wild-type bacteria  $v_m$ . Black lines indicate error function fittings. Each data point in (a)-(c) represent one experiment averaged over 30 s in time. The error bars are the standard deviations of the temporal fluctuations of measured quantities. The error bars in  $v$  are the standard deviations of the natural variation of bacterial swimming speeds in the dilute limit. Although for clarity we only show one set of experiments for each case, we have run more than 20 independent experiments near the phase boundary to locate the transition points. (d) A phase diagram of bacterial flows in the phase space spanned by  $\phi$ ,  $v$  and  $f$ . Red circles indicate the turbulent phase, whereas black squares indicate the disordered phase. The surface is the model prediction (Eq. 4.1). The crosses indicate the locales of the kinetics experiments shown in Fig. 4.6 and 4.8. (e) The rescaled phase boundary between the disordered and the turbulent phases at different  $v$  (indicated in the figure). The black line is our model prediction (Eq. 4.1), whereas the red dashed line is the prediction of Koch and Subramanian (Eq. 4.2). Inset shows the experimental phase boundary and the theoretical predictions with  $f = 1$ .

random tumbling and rotational diffusion. The transition volume fraction is then given as  $\phi_c = V_b/r_c^3$ , where  $V_b = 2\pi ab^2 = 2.20 \mu\text{m}^3$  is the volume of a single bacterium. Here, we approximate the bacterial body as a cylinder with an average length  $2a = 2.8 \mu\text{m}$  and radius  $b = 0.5 \mu\text{m}$ . The volume of bacterial flagella is too small to be considered when calculating  $V_b$ . To incorporate the presence of immobile bacteria, we extend the original model and include the higher-order hydrodynamic interaction due to reflection flows in the calculation. The model predicts the transition concentration  $\phi_c$  in the bulk limit

$$\phi_c - \frac{r_0^3}{V_b} \phi_c^2 = \frac{v_0}{fv}, \quad (4.1)$$

where  $r_0 = 1.6 \mu\text{m}$  provides a characteristic interaction range of the reflection flows and  $v_0$  is a velocity scale determined by the strength of the force dipole and the rotational relaxation of bacteria

$$v_0 = \frac{8\pi\eta V_b}{\xi l(\Gamma + 1)} \sqrt{\frac{20D_r}{3\tau}}$$

Here,  $\eta = 1 \text{ mPa}\cdot\text{s}$  is the viscosity of suspension buffer,  $\xi = 1.91 \times 10^{-8} \text{ kg/s}$  is the drag coefficient of bacterial body,  $l = 1.9 \mu\text{m}$  is the distance of the force dipole of bacteria and  $D_r = 0.057 \text{ s}^{-1}$  is the effective diffusion coefficient of bacteria.  $\xi$ ,  $l$  and  $D_r$  are all obtained from direct experimental measurements [117].  $\Gamma = (a^2 - b^2)/(a^2 + b^2)$  is the shape factor of a bacterial body. Lastly,  $\tau$  quantifies the interaction time of two bacteria bounded between  $a/v \sim 0.1 \text{ s}$  and the average tumbling time  $\tau_t \sim 1 \text{ s}$  [152]. Direct fitting of the phase boundary yields  $\tau = 0.85 \pm 0.04 \text{ s}$  within the bound, which leads to  $v_0 = 0.57 \mu\text{m/s}$ . Eq. 4.1 allows for the collapse of the transition boundaries of different parameters and shows an excellent agreement with experiments (Fig. 4.4e). The rescaled phase boundary shows that the fraction of active swimmers couples with the velocity of bacteria in determining the transition to bacterial turbulence. The equivalence of  $f$  and  $v$  can be further seen from the dynamic structure of the turbulent

flows beyond the transition point, where the velocity correlation lengths  $L$  at different  $v$  and  $f$  also collapse into a master curve when plotting against  $fv$  (Fig. 4.3). Thus, by varying  $f$ , we can effectively extend bacterial velocity over a much broader range in experiments.

The simple hydrodynamic model discussed above provides a physically intuitive picture for the emergence of bacterial collective motions. However, to incorporate many-body interactions beyond two bacteria and avoid the divergence associated with the slow algebraic decay of the dipolar interaction, one needs to consider effective media or averaged equations adapted in the kinetic theories [175]. Next, we compare our experiments with the prediction of the kinetic theories. First, at low  $\phi_c$ , the higher order term on the left side of Eq. 4.1 is negligible, which leads to  $\phi_c \sim 1/v$ , consistent with the kinetic theories [82, 173, 188]. Quantitatively, Koch and Subramanian predicted the transition volume fraction in the bulk limit [82]

$$\phi_c = \frac{\eta V_b}{\xi l} \left[ \frac{5}{\tau_t} + 30D_r \right] \frac{1}{fv} \quad (4.2)$$

where  $\xi = 6\pi\eta b \left[ 1 - \frac{1}{5}(1 - \frac{a}{b}) \right] \approx 1.28 \times 10^{-8}$  kg/s is the calculated drag coefficient of bacterial body orientated along its major axis, which is slightly smaller than the measured value shown above. The linear stability analysis of the original kinetic theories can be easily extended for the mixture of mobile bacteria and immobile bacteria with zero dipolar strength [175, 188], which results in  $f$  as the prefactor of  $v$  in Eq. 4.2. Without fitting parameters, Eq. 4.2 quantitatively agrees with our experiments (Fig. 4.4e), although small deviations between the theory and experiments can be observed at high concentrations. As such, our systematic measurements of the phase diagram provide a quantitative verification of the prediction of the kinetic theories on the transition point. Our experiments also confirm numerical results from large-scale particle-based

simulations with hydrodynamic interactions and random reorientations [103,189], where collective motions have been observed above the predicted threshold concentration.

At  $f = 1$ , we find  $\phi_c$  ranges between 0.02 and 0.08 for different bacterial velocities (Fig. 4.4e inset). The average distance between bacteria at  $\phi_c$  is about 6 to 9.5  $\mu\text{m}$ , on the order of the size of a single bacterium [152]. Short-range hydrodynamic and steric interactions could be important at such small scales [176,177]. Hence, it is nontrivial that the far-field dipolar hydrodynamic interaction adapted in our simple model (Eq. 4.1) and in the kinetic theories (Eq. 4.2) is sufficient to describe the experimental phase boundary. The observation supports the basic assumption of the kinetic theories [82,86]. Consistent with this finding, increasing the fraction of immobile bacteria at either a fixed total bacterial volume fraction  $\phi$  or a fixed volume fraction of active swimmers  $f\phi$  suppresses bacterial turbulence in our experiments (Fig. 4.5), rather than promoting the collective motion as observed in dry active matter with purely short-range steric interactions [190]. Thus, our study provides experimental evidence on the dominant role of long-range hydrodynamic interactions in 3D suspensions, resolving the controversy over the interparticle interaction responsible for 3D bacterial collective swimming. Physically, if bacterial orientation is random, the effective volume occupied by a bacterium should be considered as a sphere of radius  $a$  instead of the excluded volume of the bacterial body  $V_b$ , which would lead to much larger effective  $\phi_c$  up to 0.41 in the semi-dilute regime [140]. The dominant role of the long-range dipolar interaction observed in our experiments suggests that bacterial orientation is strongly correlated near the phase boundary under the influence of the hydrodynamic interaction. As a result, bacteria show preferred alignment with their neighbors, giving rise to relatively large inter-bacteria distances suitable for the long-range hydrodynamic interaction.

Lastly, it is worth noting that the size of samples in our experiments is fixed with the minimal dimension between 150  $\mu\text{m}$  and 170  $\mu\text{m}$ , much larger than the size of single

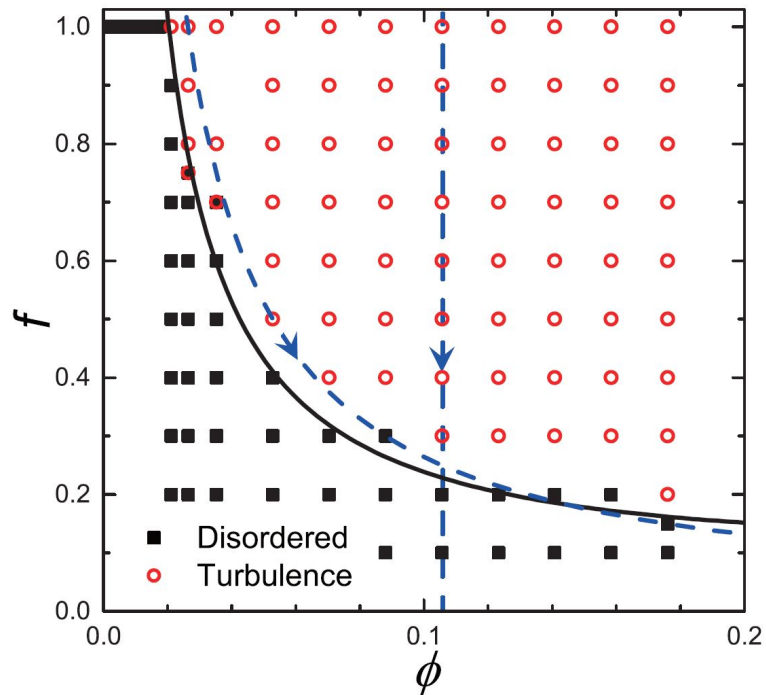


**Figure 4.5: Effect of immobile bacteria.** The phase diagram as a function of bacterial volume fraction  $\phi$  and swimmer fraction  $f$  at a fixed swimming velocity  $v = 28.7 \mu\text{m/s}$ . Black squares indicate the isotropic disordered phase, whereas red circles indicate the turbulent phase. The black solid line represents the phase boundary predicted by our simple hydrodynamic model (Eq. 4.1). The vertical line indicates a constant total bacterial concentration  $\phi = 0.11$ , whereas the curved dashed line indicates a constant concentration of active swimmers  $\phi f = 0.027$ . The arrows on the dashed lines show the direction of increasing the fraction of immobile bacteria  $1 - f$ .

bacteria. The volume of our samples is on the order of several microliters, which contains more than  $10^7$  bacteria at  $\phi = 0.018$ . Simulations and kinetic theories have shown that  $\phi_c$  is independent of the system size at such large scales [173]. More recent experiments have also shown that the onset of collective motions and bacterial superfluids is insensitive to the system size above  $170 \mu\text{m}$  [191]. Thus, the phase diagram shown in Fig. 4.4d should approximate the phase behavior of bacterial suspensions in the bulk limit.

### 4.3.3 Transition Kinetics

Next, using the phase diagram as a roadmap, we explore the kinetics of bacterial turbulent transition, which reveals the mode of instability and the transient structure of bacterial suspensions through the transition. To study the kinetics, we trigger the onset of bacterial turbulence by suddenly ramping up light intensity at  $t = 0$ , which increases the swimming speed of light-powered bacteria from that below the phase boundary to high  $v$  above the boundary at a given combination of  $\phi$  and  $f$ . Although individual bacteria in dilute suspensions recover their swimming speeds within a couple of seconds (Fig. 4.1), the emergence of collective flows can take much longer times depending on the specific control parameters. In the region above but close to the phase boundary, the transition exhibits a surprisingly long incubation period with low velocity orientational order  $M$  and kinetic energy  $E$  ( $\sim 100$  s in Fig. 4.6a). During incubation, localized regions with relatively large velocity orientational correlation (high  $c$ ) and large kinetic energy (high  $E$ ) nucleate within the disordered phase (Fig. 4.6b).

The incubation period witnesses the slow growth and the fluctuation of these high- $c$  and high- $E$  regions. After incubation, the high- $c$  and high- $E$  regions grow quickly and eventually percolate the entire system.  $M$  and  $E$  are directly coupled and increase simultaneously during the transition. The incubation period becomes increasingly short

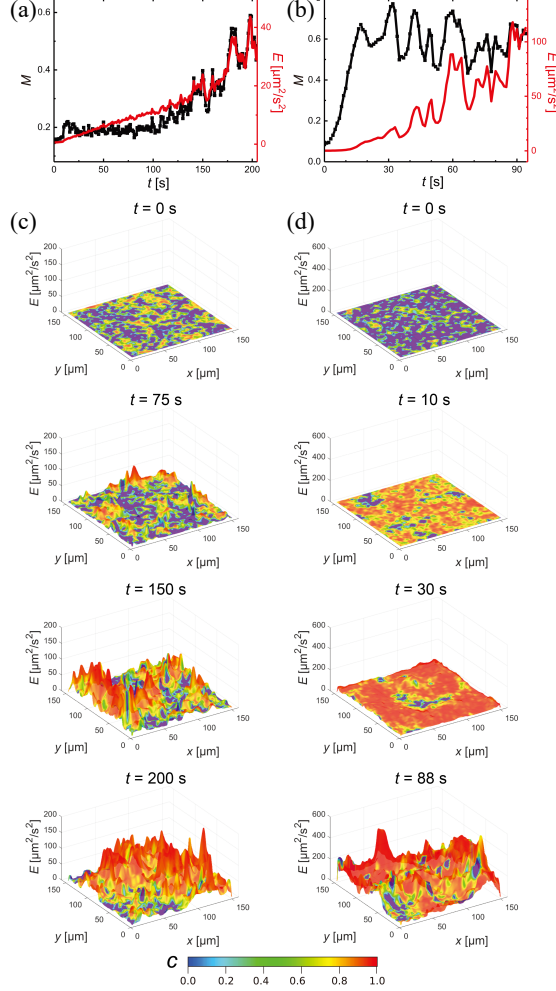
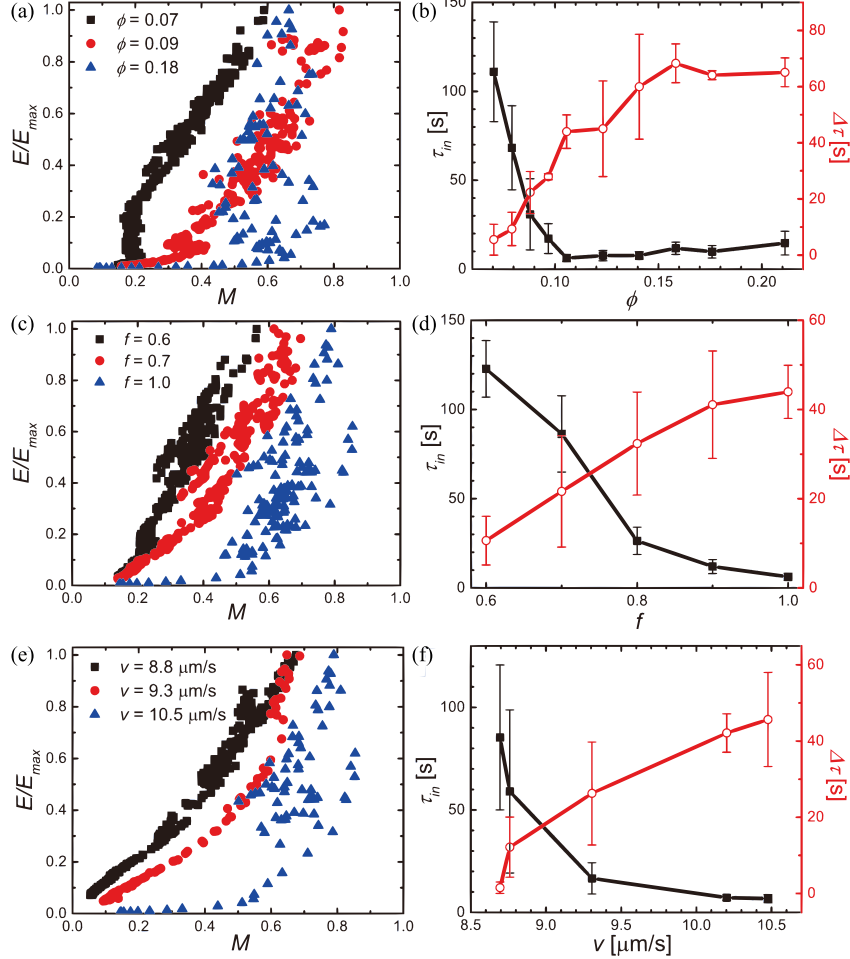


Figure 4.6: **Transition kinetics.** (a) Velocity orientational order  $M$  and kinetic energy  $E$  as a function of time through the turbulent transition.  $t = 0$  corresponds to the time when light intensity is ramped up. Bacterial volume fraction  $\phi = 0.071$ , speed  $v = 10.5 \mu\text{m}/\text{s}$  and swimmer fraction  $f = 1$ , which is near the phase boundary shown by the blue cross in Fig. 4.4d. (b) Spatiotemporal evolution of the local velocity orientational correlation  $c$  and the local kinetic energy  $E$  over the transition shown in (a). The spatial coordinates are shown in the  $x$ - $y$  plane. The height indicates the value of  $E$ , whereas the color shows the value of  $c$ . (c)  $M$  and  $E$  as a function of  $t$  for  $\phi = 0.18$ ,  $v = 10.5 \mu\text{m}/\text{s}$  and  $f = 1$  deep inside the turbulent phase shown by the red cross in Fig. 4.4d. (d) Spatiotemporal evolution of  $c$  and  $E$  over the transition shown in (c).

as we move away from the phase boundary. Far above the boundary, the increase of the velocity orientational correlation is almost instantaneous across the entire system after the light ramp (Fig. 4.6c and d), whereas the kinetic energy remains low at beginning and grows to a steady-state plateau only at a later time. The growths of  $M$  and  $E$  are decoupled in this case. The system exhibits a transient state with high velocity orientational order but low kinetic energy (the middle two pictures at  $t = 10$  and 30 s in Fig. 4.6d).

A smooth crossover from the single-step transition near the phase boundary to the two-step transition with the transient state deep inside the turbulent phase can be seen from the  $E$ - $M$  plot (Fig. 4.7a).  $E$  increases linearly with  $M$  near the phase boundary at low  $\phi$  indicating the concurrent increase of the two quantities, whereas an L-shaped  $E$ - $M$  relation is observed for the two-step transition at high  $\phi$  deep inside the turbulent phase. The fast increase of  $M$  at early times results in the flat region of the curves at low  $E$ . We further quantify the time and length scales associated with transition kinetics. The transition rate is measured by the incubation time,  $\tau_{in}$ , defined in analogy of nucleation and growth processes in equilibrium phase transitions.  $\tau_{in}$  decreases with  $\phi$  and reaches a low plateau of  $\sim 10$  s above  $\phi = 0.105$  (Fig. 4.7b), comparable to the time for a single bacterium to recover its swimming speed in the dilute limit.  $1/\tau_{in}$  provides an estimate of the growth rate of the hydrodynamic instability. The presence of the transient state with high velocity orientational correlation and low kinetic energy is characterized by the time difference,  $\Delta\tau = \tau_E - \tau_M$ , where  $\tau_E$  and  $\tau_M$  are the times when  $E$  and  $M$  reach their steady states, respectively.  $\Delta\tau$  increases with  $\phi$  and can be as large as 65 s above  $\phi = 0.16$  deep inside the turbulent phase. Note that although we discuss transition kinetics with increasing  $\phi$ , qualitatively similar trends are also observed when  $v$  and  $f$  are varied (Figs. 4.7c-f).

The length scales associated with the transition kinetics are revealed by the energy



**Figure 4.7: One-step and two-step transitions.** (a) Kinetic energy  $E$  versus velocity orientational order  $M$  over a transition at a given bacterial volume fractions  $\phi$ , fixed bacterial speed  $v = 10.5 \mu\text{m/s}$  and swimmer fraction  $f = 1$ . While the one-step transition shows an approximately linear concurrent increase of  $E$  and  $M$  over time (black squares), the two-step transition shows an increase  $M$  at low in the first step at early times and then an increase of  $E$  at an approximately constant  $M$  in the second step at later times (blue triangles).  $E$  is normalized by the maximal energy density at the steady state,  $E_{max}$ . (b) Incubation time,  $\tau_{in}$ , and the time difference,  $\Delta\tau$ , as a function of  $\phi$  at the same  $v$  and  $f$  as in (a). The error bars reflect the standard error of three to twelve experimental runs for each data point. (c)  $E/E_{max}$  versus  $M$  at different  $f$  and a fixed  $\phi = 0.11$  and  $v = 10.5 \mu\text{m/s}$ . (d)  $\tau_{in}$  and  $\Delta\tau$  at different  $f$  at the same  $\phi$  and  $v$  as in (c). (e)  $E/E_{max}$  versus  $M$  at different  $v$  and a fixed  $\phi = 0.11$  and  $f = 1$ . (f)  $\tau_{in}$  and  $\Delta\tau$  at different  $v$  at the same  $\phi$  and  $f$  as in (e).

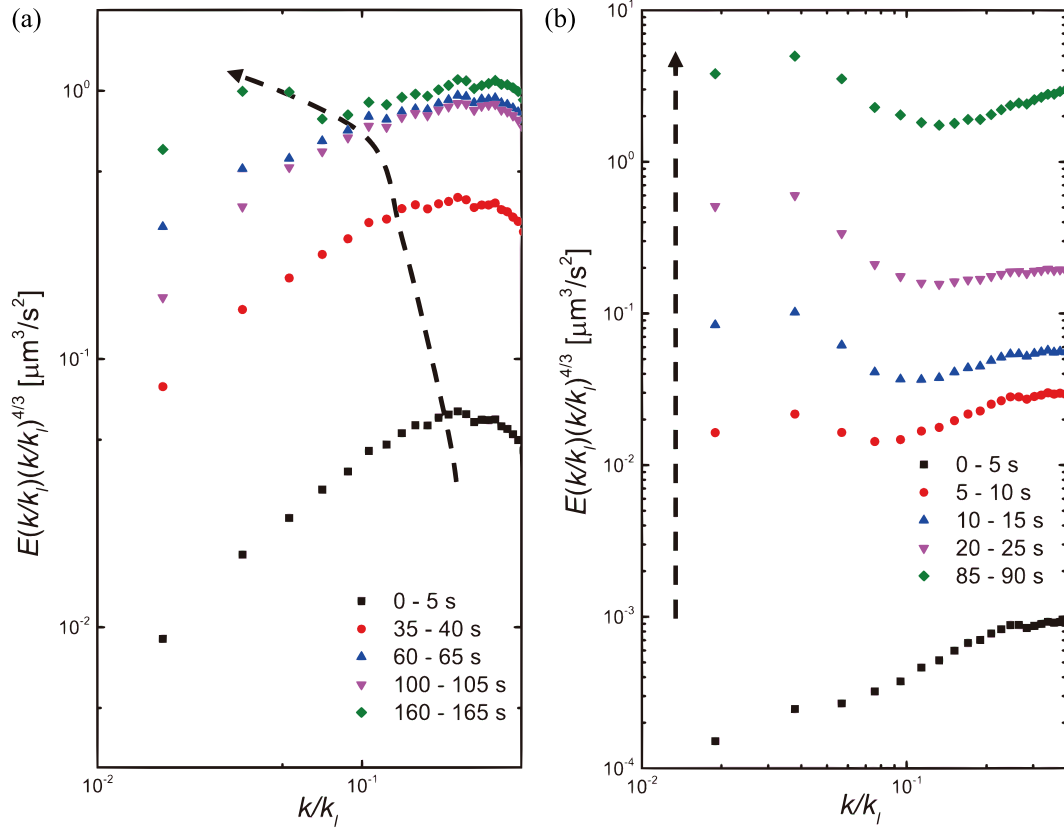
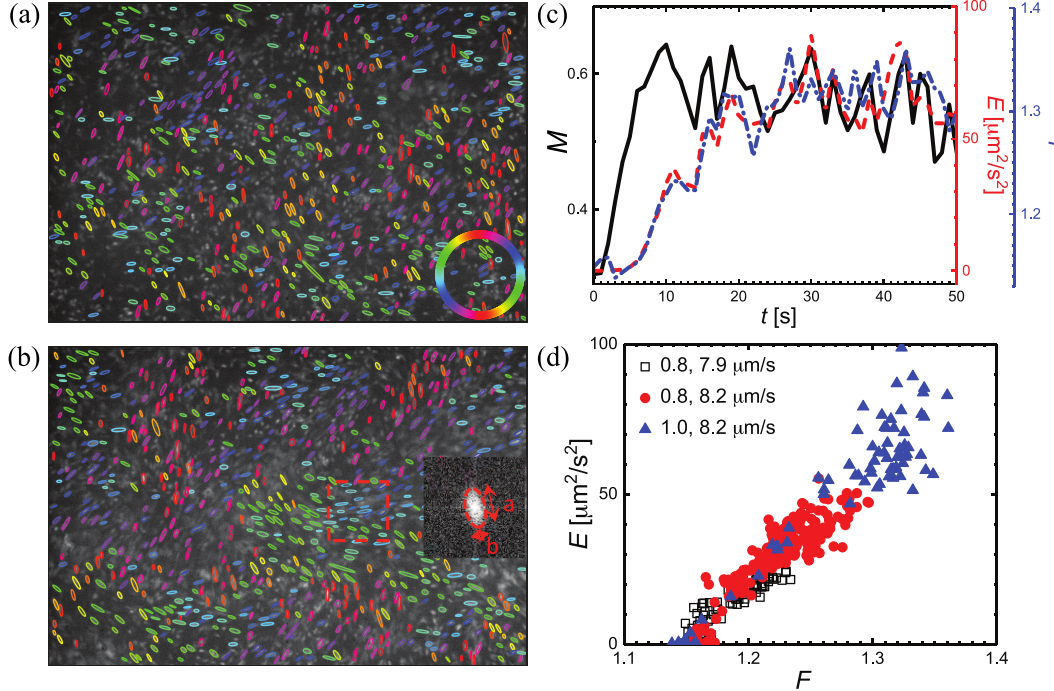


Figure 4.8: **Energy spectra through the bacterial turbulent transition.** (a) Temporal evolution of energy spectrum  $E(k)$  through the turbulent transition for a system near the phase boundary (blue cross in Fig. 2D). Bacterial volume fraction  $\phi = 0.071$ , speed  $v = 10.5 \mu\text{m}/\text{s}$  and swimmer fraction  $f = 1$ . (b) Temporal evolution of  $E(k)$  through the turbulent transition for a system deep inside the turbulent phase (red cross in Fig. 2D).  $\phi = 0.18$ ,  $v = 10.5 \mu\text{m}/\text{s}$  and  $f = 1$ . Since  $E(k)$  shows a  $k^{-4/3}$  scaling at high  $k$  from direct fitting, we plot  $E(k)(k/k_l)^{4/3}$  to make the curves flat at high  $k$ , where  $k_l = 2\pi/3 \mu\text{m}^{-1}$  is the wavenumber for the size of single bacteria. The dashed arrows indicate different increasing trends of  $E(k)$ .

spectrum of bacterial flows,  $E(k)$ , where  $k$  is the wavenumber [21].  $E(k)$  is related to the energy density  $E$  through  $E = \int_0^\infty E(k)dk$ . Near the phase boundary, the increase of  $E(k)$  initiates at large  $k$  (or short wavelengths) and then propagates to small  $k$  over time (Fig. 4.8a), consistent with the scenario of nucleation and growth. In sharp contrast, deep inside the turbulent phase, the spectrum increases significantly faster at small  $k$  at early times (Fig. 4.8b), indicating a long-wavelength instability. Such a long-wavelength instability qualitatively explains the two-step transition. The instability at a long wavelength naturally leads to a longrange velocity orientational correlation and, therefore, the fast increase of  $M$  at early times. However, since  $E$  is determined by the integral of  $E(k)$  over all  $k$ , the early-time increase of  $E(k)$  at small  $k$  does not substantially affect the total kinetic energy, which shows strong increase only when  $E(k)$  at high  $k$  starts to grow at later times. Hence, our measurements of transition kinetics provide experimental evidence confirming the key prediction of the kinetic theories on the existence of a long wavelength instability in suspension of pusher swimmers [66,81,92,174]. The observation of the long incubation period near the phase boundary is, however, not captured by the kinetic theories. Although the growth rate of the long wavelength instability also approaches zero near the phase boundary within the framework of the kinetic theories, one would expect to see the initial increase of  $E(k)$  at small  $k$  near the phase boundary. This prediction contradicts our k-space analysis (Fig. 4.8a), as well as the real-space observation shown in Fig. 4.6b, where the collective turbulent phase initiates locally at small scales and coalesces into large-scale structures only after the prolonged incubation period. Beyond the kinetic theories, the presence of two different transition kinetics is reminiscent of a theoretical phase diagram on the motility-induced phase separation of active fluids, where binodal and spinodal regions have been predicted based on the concept of swim pressures [192].



**Figure 4.9: Microscopic view of the turbulent transition deep inside the turbulent phase.** Confocal microscopy of a bacterial suspension at  $t = 10$  s (a) and  $30$  s (b) after the light ramp. The incubation time of the transition  $\tau_{in} \approx 6$  s. Bacterial volume fraction  $\phi = 0.14$ , speed  $v = 8.2 \mu\text{m}/\text{s}$  and swimmer fraction  $f = 1$ . Individual bacteria identified manually are marked with ellipsoids, whose orientation is indicated by the color bar in the inset of (a). The inset of (b) shows the FFT of a local region of  $20 \times 20 \mu\text{m}^2$  indicated by the dashed box. The aspect ratio of FFT patterns averaged over all the local regions,  $F \equiv \langle a/b \rangle$ , is used to quantify the local nematic order of bacteria. (c) Velocity orientational order,  $M$ , kinetic energy,  $E$ , and  $F$  as a function of time  $t$  through the transition shown in (a) and (b). The black solid line is for  $M$  shown to the left axis, whereas the red dashed line and the blue dash-dotted line are for  $E$  and  $F$ , respectively, shown to the right axis.  $E$  and  $F$  show quantitatively similar trends, different from that of  $M$ . (d)  $E$  versus  $F$  at  $\phi = 0.14$  and different  $f$  and  $v$  (indicated in the figure). The open squares are for a system close to the phase boundary with the one-step transition, whereas the blue triangles are for a system deep inside the turbulent phase with the two-step transition. The red circles are for a crossover system between the two limits. Different from the  $E$ - $M$  plots shown in Fig. 4.6a, c and e, all the data collapse into a master curve showing the linear relation between  $E$  and  $F$ .

#### 4.3.4 Microscopic View

Lastly, we examine the evolution of the long-wavelength instability from the perspective of the dynamics of single bacteria using high-resolution fast confocal microscopy (Fig. 4.9a, b). We find that the two-step transition deep inside the turbulent phase can be understood microscopically from the development of the orientational order of bacteria in emerging turbulent flows. Directly tracking the orientation of individual bacteria in dense 3D suspensions is unavoidably subject to large experimental errors. In order to quantify the local nematic order of bacteria without tracking individual bacteria, we perform Fast Fourier Transform (FFT) on local regions ( $20 \times 20 \mu\text{m}^2$ ) of confocal images. The degree of the local nematic order is characterized by the anisotropy of the resulting FFT patterns,  $F$  (Fig. 4.9b inset). Our measurements show that the local bacterial nematic order is linearly proportional to the kinetic energy  $E$ , but decouples from the velocity orientational order  $M$  in the two-step transition (Fig. 4.9c, d).

The finding suggests the following physical picture. At early times, a slight deviation from the isotropic distribution of bacterial orientations induced by the long wavelength instability is sufficient to establish a strong velocity orientational correlation, where bacteria still appear to orientate randomly in the emergent turbulent flow as shown in Fig. 4.9a. This picture further corroborates the exceptional robustness of bacterial turbulence identified at large  $f$  of the phase diagram (Fig. 4.4d). Over time, the kinetic energy gradually increases as the local bacterial alignment is enhanced by local coherent flows (Fig. 4.9c). This positive feedback loop between kinetic energy and bacterial alignment qualitatively agrees with the numerical solution of the kinetic equations in the nonlinear regime [66], where the alignment of pusher swimmers with the direction of local flows develops progressively through the transition and the increasing alignment in turn enhances the velocity of local flows. A strong steady-state turbulence is finally established when bacteria well align with their neighbors as shown in Fig. 4.9b,

which gives rise to both a large kinetic energy and a high local bacterial nematic order. Thus, our confocal measurements provide a microscopic view of the kinetics of the long-wavelength-instability-driven two-step transition: the disordered phase (low  $M$ , low  $E$ , low  $F$ ) → the disordered turbulent phase (high  $M$ , low  $E$ , low  $F$ ) → the ordered turbulent phase (high  $M$ , high  $E$ , high  $F$ ).

#### 4.4 Discussion and Conclusion

We experimentally studied the emergence of the collective motion of bacterial suspensions, the so-called bacterial turbulence. By using three different *E. coli* strains and examining over a thousand of bacterial suspensions at different concentrations, swimming speeds and fractions of active swimmers, we systematically mapped a phase diagram of 3D bulk bacterial flows over a large control parameter space in a single experimental system. Furthermore, taking the advantage of genetically engineered light-powered *E. coli* whose locomotion can be reversibly controlled by light, we imaged the onset of bacterial turbulence and performed detailed measurements on the kinetic pathways of bacterial turbulence transition.

The contribution of our study is two-fold. On the one hand, our experiments validated the assumption of the kinetic theories of collective bacterial motions and verified the main predictions of the theories on the transition point and the mode of instabilities. Specifically, the phase boundary of our experimental phase diagram showed a quantitative agreement with the prediction of the theories without fitting parameters. Our kinetic measurements further showed the existence of the long wavelength instability deep inside the turbulent phase and therefore provided an experimental support to this key theoretical prediction. In addition, our microscopic measurements on single bacterial dynamics through the long-wavelength instability revealed the rise of local bacterial nematic order and its coupling with local coherent flows, qualitatively testifying the

numerical solution of the kinetic equations in the nonlinear regime.

On the other hand, our measurements also revealed new features of bacterial turbulent transition, unexpected from existing theories. Particularly, we explored the effect of doping immobile bacteria on the phase dynamics of bacterial flows, which allowed us to distinguish the dominant role of hydrodynamic interactions in the formation of bacterial collective swimming in 3D suspensions. The finding not only resolved the controversy over the relative importance of hydrodynamic versus steric interactions, but also illustrated the remarkable robustness of bacterial turbulent flows with high fractions of malfunctioning units. More importantly, our experiments uncovered two distinct kinetic pathways towards bacterial turbulence at different locales of the phase diagram, i.e., the one-step transition with long incubation periods near the phase boundary and the two-step transition driven by the long wavelength instability deep inside the turbulent phase. These two pathways exhibited dramatically different transition rates and transient structures, suggesting two qualitatively different transition mechanisms.

Taken together, our study provided an experimental benchmark on the collective behaviors of 3D suspensions of swimming microorganisms. The quantitative understanding of the phase diagram and kinetics of bacterial turbulent transition from our study paves a foundation for achieving a dynamic control over mass transport, fluid mixing and rheology of bacterial suspensions in microfluidic applications [25, 30]. As bacterial suspensions are widely viewed as a paradigmatic example of active matter, our experiments are also valuable more broadly for understanding the general organizing principles of the “thermodynamics” and kinetics of nonequilibrium phase transitions in active matter [192].

Finally, our study also opens new questions for future experimental and theoretical development. First, it is unclear on the microscopic origin of the long incubation period in the one-step transition near the phase boundary. Our preliminary study indicates

that the incubation process may be influenced by the formation of bacterial clusters in suspensions. Nevertheless, the incubation time can be significantly longer than the time scale associated with the dissolving of bacterial clusters close to the phase boundary, suggesting the generic nature of the phenomenon. To understand the nucleation and growth process with long incubation, prolonged experiments are required beyond the time scale of typical bacterial experiments, which pose an experimental challenge due to photobleaching and decreasing bacterial activity over time. How to incorporate the incubation process in the kinetic theories also presents a challenging theoretical question. Second, the long wavelength instability observed in our experiments indicates a system-size dependence of phase dynamics in confined systems. The change of the phase diagram and the transition kinetics with the system size needs to be further confirmed and measured in future experiments. Lastly, it is certainly worth of investigating the kinetic route to collective motions in other active fluids such as active cytoskeletons [193] and suspensions of colloidal swimmers [44] and checking to what extent the kinetic features observed in our experiments are generic for active fluids in general.

## Chapter 5

# Giant Number Fluctuations in 3-Dimensional Space

### 5.1 Introduction

Active fluids exhibit many unusual behaviors beyond the expectation of equilibrium statistical mechanics [5, 7, 115, 194, 195]. In particular, an active fluid can exhibit anomalously large density variations, the so-called giant number fluctuations (GNF), where the standard deviation of the number of particles grows nonlinearly with the square root of the mean particle number, defying the central limit theorem of equilibrium systems [196]. Such unusual density fluctuations have been observed in a wide range of active fluids in both living and non-living systems including vibrated granular rods [67, 93, 95, 100], swarming bacteria [94, 98] and mammalian cells [97], self-propelled cytoskeleton [96], and synthetic colloidal swimmers [15, 99]. As a result, GNF has generally been viewed as a hallmark of the emergent behaviors of active fluids.

Significant theoretical and computational advancement on GNF has been made over the past two decades since the seminal works of Toner and Tu [4, 8, 19, 76, 78–80, 87–

89, 91, 92, 197]. Meanwhile, many important theoretical and numerical predictions have been tested in experimental realizations [15, 67, 93–98].

Of particular interest is the scaling exponent  $\alpha$ , which is defined following  $\Delta N/\sqrt{N} \propto N^\alpha$ , where  $\Delta N$  is the standard deviation of particle number and  $N$  is the mean number of particles in a subsystem of given size. Heretofore, all the existing experiments on GNF were limited to two-dimensional (2D) or quasi-2D systems. In contrast to theoretical predictions (where  $\alpha \approx 0.3$ ),  $\alpha$ 's obtained in these experiments show large variations ranging from 0.13 to 0.5. Such a large variation arises partially because of complicated particle-boundary interactions, which are hard to incorporate in theoretical studies. Moreover, the predictions of  $\alpha$  in three-dimensional (3D) wet active fluids—one of the most important classes of active fluids where hydrodynamics dominate the interparticle interactions and conserve the total momentum of systems [7]—has not been experimentally testified. Therefore, there is an imperative need for an experimental measurement of  $\alpha$  in 3D active fluids, which are not affected by system boundaries. Such a measurement will provide not only an unambiguous experimental benchmark to testify theories of active fluids, but also experimental support on the effect of dimensionality on GNF of active fluids [7].

The rise of GNF in active fluids is usually accompanied by the transition to ordered phases with collective motions [5, 7]. For wet 3D active fluids such as bacterial suspensions, these collective motions lead to large-scale coherent flows with intermittent vortices and jets, which are often referred to as active turbulence [2, 21, 70, 101, 103, 104, 106, 141, 172, 198]. Similar to GNF that manifests density fluctuations across different scales, the flow of active turbulence also exhibits scale-dependent structures. Imported from the study of classical turbulence, energy spectra are frequently measured to quantify such structures in active turbulence [21, 70, 84, 102, 198–200]. Although both GNF and energy spectra quantify the scale-dependent dynamics of active fluids, the deep

connection between these two quantities at different scales has not been experimentally investigated. Our experiment reveals the density- and scale- independent coupling between GNF and energy spectra, suggesting that GNF is governed by the strength of the motion-induced flow.

## 5.2 Methods

### 5.2.1 Sample Preparation, Imaging and Analysis

Here, we present our systematic experimental study of GNF and energy spectra in bulk bacterial suspensions, a premier example of 3D wet active fluids. We use genetically engineered light-powered *Escherichia coli* (*E. coli*) as our model bacteria. For a typical experiment, a bacterial suspension of control volume fraction  $\phi$  is injected into a sealed chamber of  $20 \text{ mm} \times 3 \text{ mm} \times 140 \mu\text{m}$ . Without supply of oxygen, bacteria quickly consume all the remaining oxygen in the chamber and stop moving after 5 minutes. We then illuminate the suspension with a high-intensity microscope light, which powers bacteria at their maximal swimming speed of  $15 \pm 3 \mu\text{m/s}$  in the dilute limit. A video of the suspension is taken  $50 \mu\text{m}$  above the bottom wall of the chamber by a bright-field inverted microscope at a frame rate of 30 fps and the field of view of  $420 \times 360 \mu\text{m}^2$  (Fig. 5.1a, c). We use a standard Particle Image Velocimetry (PIV) algorithm [134] to extract the 2D in-plane velocity field  $(v_x, v_y)$  in the 3D suspension, which exhibits the characteristic chaotically-moving vortices and jets of active turbulence at high  $\phi$  (Fig. 5.1b, d).

### 5.2.2 The Relation between Pixel Intensity and Concentration

It is challenging to directly count the number of bacteria in a 3D suspension of fast moving bacteria. Luckily, by virtue of Beer-Lambert law, the local bacterial density is

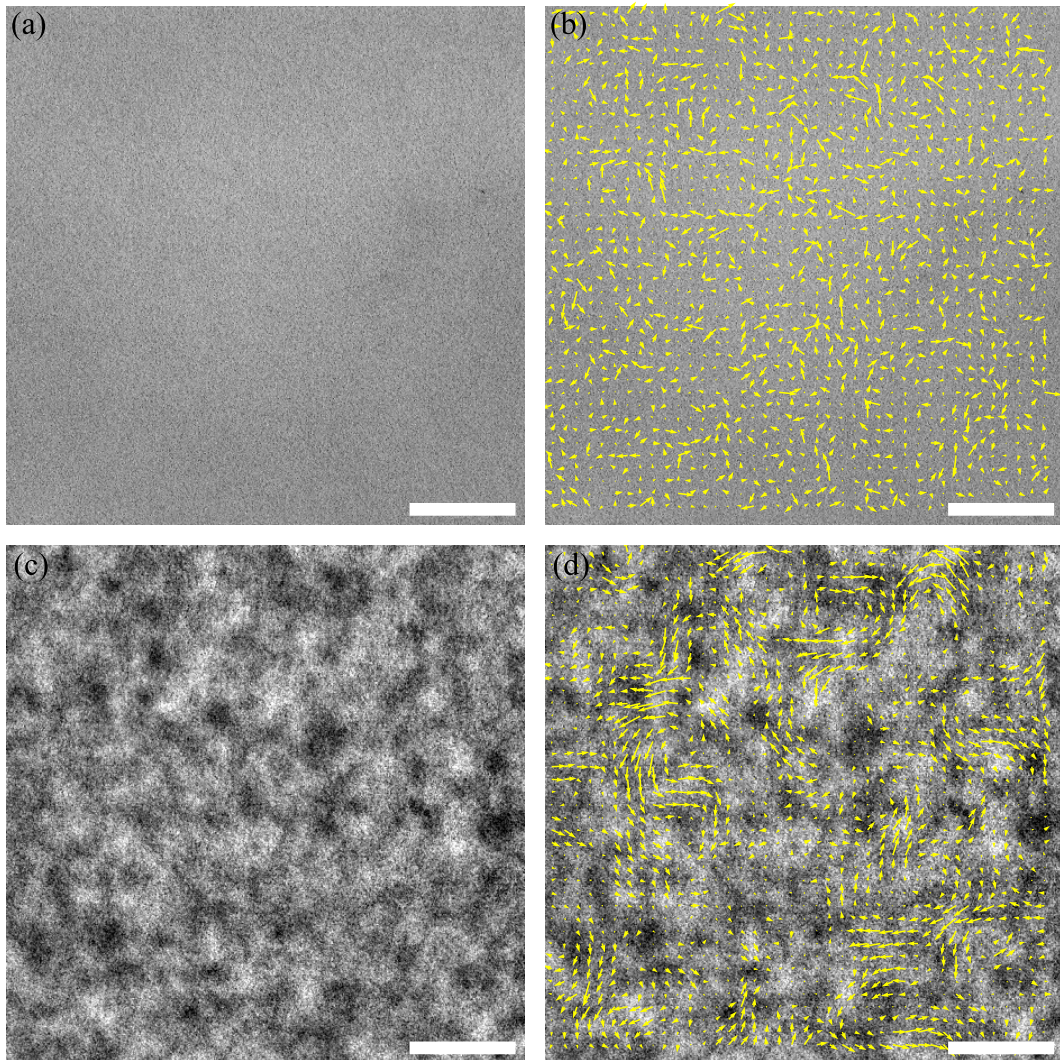


Figure 5.1: **Images of bacterial active turbulence and its flow fields.** (a) and (b) are active turbulence in a dense bacterial suspension (1.6%) displaying constantly varying concentration inhomogeneity and the corresponding flow field. (c) and (d) are a dilute bacterial suspension (6.4%) and the corresponding flow field. Scale bars are 85  $\mu$  m.

monotonically correlated with the local intensity of microscope images, where darker regions correspond to higher bacterial densities (Fig. 5.1c). Similarly principles also appeared in other experimental works, where optical information was exploited in probing the dynamics in suspensions of bacteria and actin filaments [23, 96, 201].

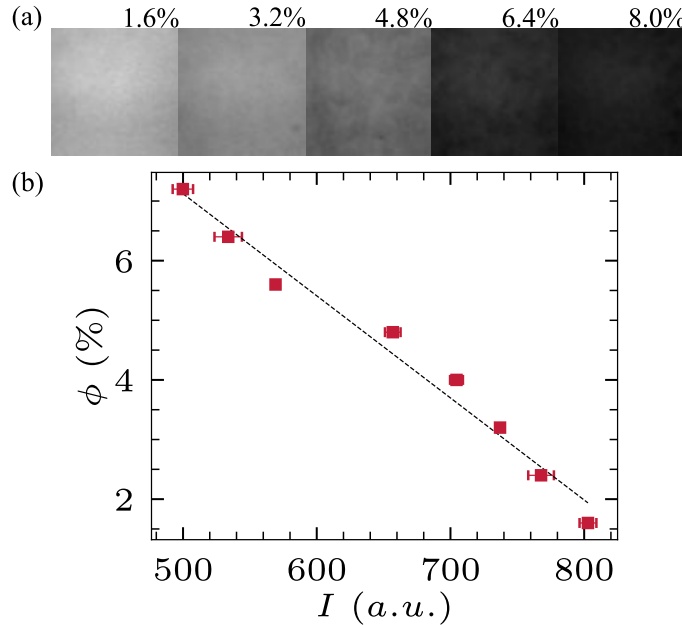


Figure 5.2: **Relation between image intensity and concentration.** (a) Images of bacterial suspensions of different volume fractions under the same illumination conditions. (b) Volume fractions as a function of average pixel intensities.

To calibrate the density-intensity correlation, we prepare bacterial suspensions of different  $\phi$  and image the suspensions under the same illumination (Fig. 5.2a). The mean image intensity decreases with increasing  $\phi$  following an approximately linear relation (Fig. 5.2b), agreeing with the Beer-Lambert law for samples of small thickness and weak absorptivity appropriate for our experiments. The linear density-intensity relation has also been used in previous experiments on *E. coli* suspensions [201].

In the low attenuation limit (small thickness and weak absorptivity),  $I = I_0 - \epsilon$

where  $\epsilon \ll I_0$ :

$$\log \frac{I_0}{I} = \log \frac{I_0}{I_0 - \epsilon} \approx \frac{\epsilon}{I_0} \sim c \quad (5.1)$$

$$I = I_0 - \epsilon \sim c \quad (5.2)$$

where  $I_0$  is the original light intensity,  $I$  is the transmission light intensity,  $\epsilon$  is the attenuated light intensity, which is much smaller than the original light intensity.

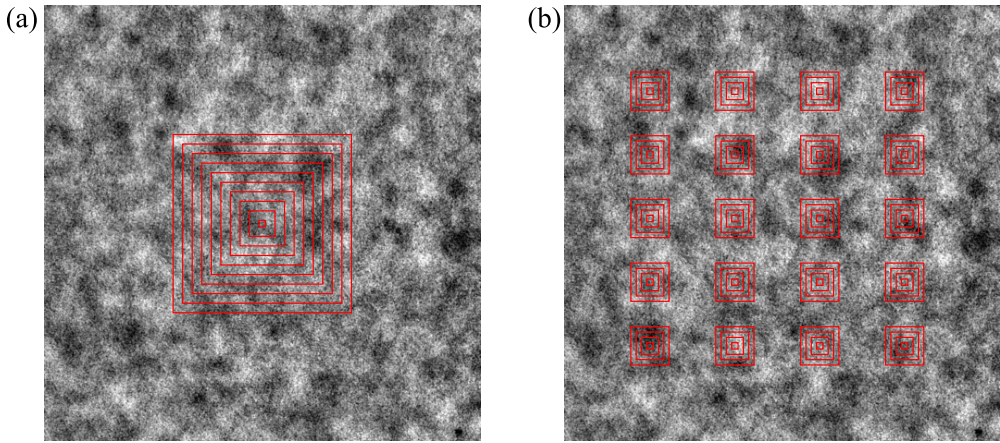


Figure 5.3: **GNF calculations.** (a) Varying subsystem sizes. (b) Multiple seeds of subsystems for spatial average.

### 5.2.3 GNF Calculations

In Fig. 5.2b, we show that under the same illumination and imaging condition, bacterial density and the average pixel intensity follow approximately a linear relation, which can be expressed as follows:

$$\phi = a + bI, \quad (5.3)$$

where  $\phi$  is the volume fraction of bacterial suspensions,  $I$  is the average pixel intensity,  $a$  and  $b$  are constants at the fixed illumination and imaging condition. The number of

bacteria in a given subsystem of side length  $l$  and thickness  $d$  can be calculated as

$$N = \frac{l^2 d}{V_b} \phi = \frac{l^2 d}{V_b} (a + bI), \quad (5.4)$$

where  $V_b$  is the volume of a single bacterium.  $d \approx 6 \mu\text{m}$  is the depth of the field of microscopy, which is fixed in our experiments. Thus, the number of bacteria in the subsystem  $N$  is proportional to  $l^2\phi$ . Taking the standard deviation of both sides of Eq. 5.4, we obtain

$$\Delta N = \frac{l^2 d}{V_b} |b| \Delta I, \quad (5.5)$$

where  $\Delta N$  is the standard deviation of the bacterial number in the subsystem over time and  $\Delta I$  is the standard deviation of the average pixel intensity of the subsystem over time. Since  $d|b|/V_b$  is a constant independent of subsystem sizes and bacterial volume fractions,  $\Delta N$  is linearly proportional to  $l^2\Delta I$ . Because any constant in front of  $\Delta N$  would not affect either the scaling relation or the relative magnitude of density fluctuations at different  $\phi$ , we simply take  $l^2\Delta I$  as  $\Delta N$  in our study.

Based on the linear relation between  $\Delta N$  and  $\Delta I$ , we calculate the density fluctuations at different length scales. We first crop square-shape subsystems of increasing sizes, as shown in Fig. 5.3. For each subsystem size  $l$ , the standard deviation of the average pixel intensity of the subsystem is calculated over 50 frames (1.67 s or  $8.35\tau_b$ ), which is longer than the saturated density correlation time of  $4\tau_b = 0.8$  s. To improve statistics, we choose 20 subsystems of the same size evenly distributed in the field of view and obtain a spatial average of the temporal standard deviation of the average pixel intensity  $\Delta I$  (Fig. 5.3). This averaged  $\Delta I$  is then multiplied by  $l^2$  to give the number density fluctuations  $\Delta N$  at the length scale  $l$ . Note that a second method has also been proposed for calculating number fluctuations, where the standard deviation of particle numbers is computed first spatially over different locations in a single time frame and is

then averaged over time of different frames [93]. Although the two methods lead to the same results when spatial and temporal correlations are small compared with the system size and experiment duration [93], the second method is subject to potential systematic errors in our study due to time-independent non-uniform light illumination and intrinsic stationary density variations in non-motile suspensions at  $t = 0$  in the kinetic measurements. Using the first method, any stable non-uniform light illumination or stationary non-uniform density variations would result in zero temporal standard deviations of  $I$  and, therefore, would not affect our measurements of true density fluctuations of motile bacterial suspensions.

#### 5.2.4 Normalization of GNF at Different Volume Fractions

Practically, to optimize image qualities, we adjust the exposure time of imaging for suspensions of different  $\phi$ . Exposure times affect the proportional constant  $b$  in Eq. 5.3, which introduces a  $\phi$ -dependent linear constant  $b(\phi)$  in Eq. 5.4. Although  $b(\phi)$  does not affect the scaling exponent of density fluctuations  $\alpha$ , it modifies the relative magnitude of  $\Delta N$  at different  $\phi$ . In order to compare the magnitude of density fluctuations at different  $\phi$ , we further calibrate and normalize  $\Delta I$  for different  $\phi$ . Specifically, as the calibration, we take videos of bacterial suspensions at different  $\phi$  under the exact same imaging condition with fixed illumination light intensity, condenser position, optical filters and all the camera settings such as the exposure time and the dynamic range. The calibration results are shown in Fig. 5.4, where  $\Delta N \sim l^2 \Delta I$  at different  $\phi$  collapse at small length scales. The calibration results show that we can normalize  $l^2 \Delta I$  of different exposure times by its value at a fixed small length scale. We choose the small scale at  $l = 0.3l_b$  in our study. Since  $l^2 \Delta I$  at different  $\phi$  shows the same slope at small  $l$ , choosing any other small lengths between  $0.1l_b$  and  $0.5l_b$  would lead to quantitatively the same results. The normalized density fluctuations show not only the correct scaling

exponents but also the right relative magnitudes at different  $\phi$ .

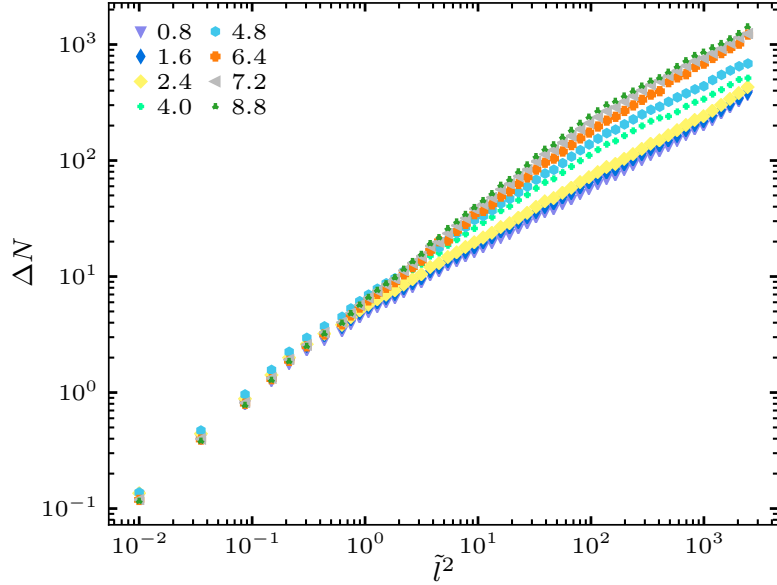


Figure 5.4: Calibration of the standard deviation of bacterial number  $\Delta N \sim l^2 \Delta I$  at different volume fractions  $\phi$ .  $\Delta N$  versus the dimensionless subsystem size  $\tilde{l}^2 = l^2/l_b^2$  for bacterial suspensions at different  $\phi$ . The images are taking under the same illumination with the same imaging condition.

### 5.2.5 Correlation of Local Density Fluctuations and Kinetic Energies

To calculate local temporal density fluctuations, we need to approximate instantaneous intensity variations. On the one hand, the time interval for calculating the intensity difference between two frames needs to be smaller than the density correlation time ( $4\tau_b = 0.8$  s) in order to satisfy the instantaneous approximation. On the other hand, the time interval should be sufficiently long to suppress the influence of random fluctuations of image intensities in adjacent frames. In our study, we choose 0.3 s (10 frames) for the local density fluctuation calculation. We do not expect the results to be much different

when varying this number from 0.17 to 0.6 s.

To calculate the local density variations at the length scale of  $l = 2.75l_b$  and time  $t$ , we take 10 consecutive frames following the frame at  $t$ . All the 10 frames are first coarse-grained by averaging the intensity of pixels in square windows of size  $2.75l_b \times 2.75l_b$  into single coarse-grained pixels (Fig. 5.5b). We then take the temporal standard deviation of the coarse-grained pixel intensity over the 10 frames at different positions to obtain a field of density fluctuations at  $t$ ,  $\delta N(\mathbf{r}, t)$ , as shown in Fig. 5.5d.

Independently, the PIV algorithm is also applied on the original images of the first two frames to obtain the velocity field at time  $t$ ,  $\mathbf{v}(\mathbf{r}, t)$  (Fig. 5.5c). Since the step size of the PIV analysis is also at  $2.75l_b$ , the velocity field has the same dimensions as the coarse-grained density fluctuation field obtained above. The local kinetic energy can then be calculated as  $E(\mathbf{r}, t) = |\mathbf{v}(\mathbf{r}, t)|^2/2$  (Fig. 5.5e). Finally, the normalized correlation between  $\delta N(\mathbf{r}, t)$  and  $E(\mathbf{r}, t)$  is computed as

$$C_s = \frac{\langle (\Delta N - \bar{\Delta N})(E - \bar{E}) \rangle}{\sigma_{\Delta N} \sigma_E}, \quad (5.6)$$

where  $\bar{A}$  indicates the mean of variable  $A$ ,  $\sigma_A$  indicates the standard deviation of  $A$ , and  $\langle A \rangle$  denotes the average of  $A$  over all the positions. The correlation quantifies the spatial similarity between  $\delta N$  and  $E$ , which ranges between  $-1$  to  $1$ .

## 5.3 Results

### 5.3.1 Density Fluctuations

The simple linear relation allows us to measure the spatiotemporal evolution of relative local bacterial densities and investigate density fluctuations in 3D bacterial suspensions. We first calculate the two-point density spatial correlation and the density auto-correlation for suspensions of different  $\phi$  and compare them with well-studied velocity

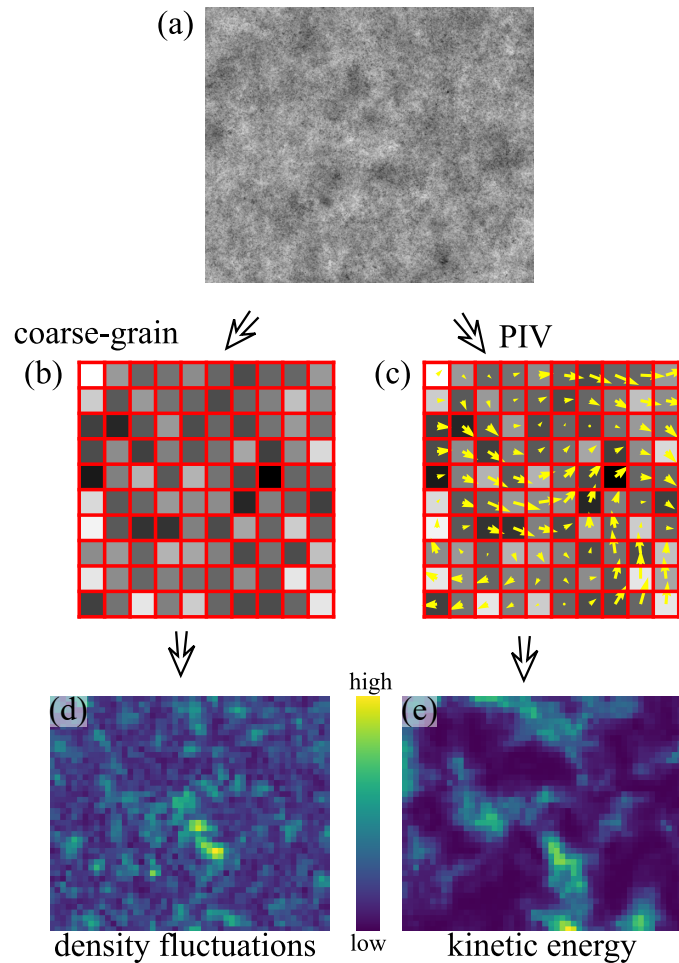


Figure 5.5: Diagram showing the procedure to calculate the correlation between local density fluctuations and kinetic energies. (a) The raw image of a bacterial suspension at a given time  $t$ . (b) The coarse-grained image with a pixel size of  $l = 2.75l_b$ . (c) The velocity field from PIV. (d) The field of local density fluctuations, obtained by calculating the standard deviation of the intensity of coarse-grained pixels shown in (b) over a short time interval. (e) The field of local kinetic energy, obtained by calculating  $E = \mathbf{v}^2/2$  from the velocity field shown in (c).

correlations extracted from PIV (Fig. 5.6).

The correlation length  $\lambda$  and correlation time  $\tau$  are determined when the corresponding normalized correlation functions decay to  $1/e$  (Fig. 5.6c, f). Figure 5.6c shows the density correlation lengths at different  $\phi$ , which characterize the scale of density inhomogeneities in suspensions.  $\lambda$  is small at low  $\phi$ , gradually increases with  $\phi$  and reaches a plateau of  $\sim 5l_b$  in high-concentration bacterial suspensions of  $\phi > \phi_c = 3.2\%$ , where  $l_b = 3 \mu\text{m}$  is the average length of bacterial body. The velocity correlation length follows the exact same trend and also saturates when  $\phi > \phi_c$ . Such a quantitative similarity indicates the direct coupling between density fluctuations and collective turbulent flows, a feature we shall examine in much more details later. In the fully-developed turbulent regime above  $\phi_c$ , the velocity correlation length is about twice the density correlation length. Fig. 5.6f shows the density and velocity correlation times at different  $\phi$ . The velocity and density correlation time at low  $\phi$  show a large discrepancy. When  $\phi > \phi_c = 3.5\%$ , they plateau at  $\sim 6\tau_b$  and  $\sim 4\tau_b$ , respectively, where  $\tau_b = 0.2 \text{ s}$  is the characteristic time scale of *E. coli* swimming.

We further examine GNF by calculating the standard deviation of bacterial number  $\Delta N$  and the mean bacterial number  $N$  in subsystems of increasing sizes. The normalized  $\Delta N$  as a function of rescaled subsystem size  $\tilde{l}^2 = l^2/l_b^2$  for bacterial suspensions of different  $\phi$  is plotted in Fig. 5.7, where  $l$  is the side length of square subsystems. Note that the area of the subsystem  $l^2$  is linearly proportional to mean particle number  $N$  at a given  $\phi$ . At small length scales, when  $l \leq \lambda_n$ , bacterial suspensions of all volume fractions examined in this study (0.8% to 9.6%) exhibit GNF, with  $\Delta N$  increasing with subsystem size  $l^2$ . When the size of subsystems is much larger than the density correlation length  $\lambda$ , the giant fluctuation diminishes due to the spatial average over multiple dense and dilute regions.

The degree of GNF can be quantified by the scaling exponent  $\alpha$  following  $\Delta N/\sqrt{N} \sim$

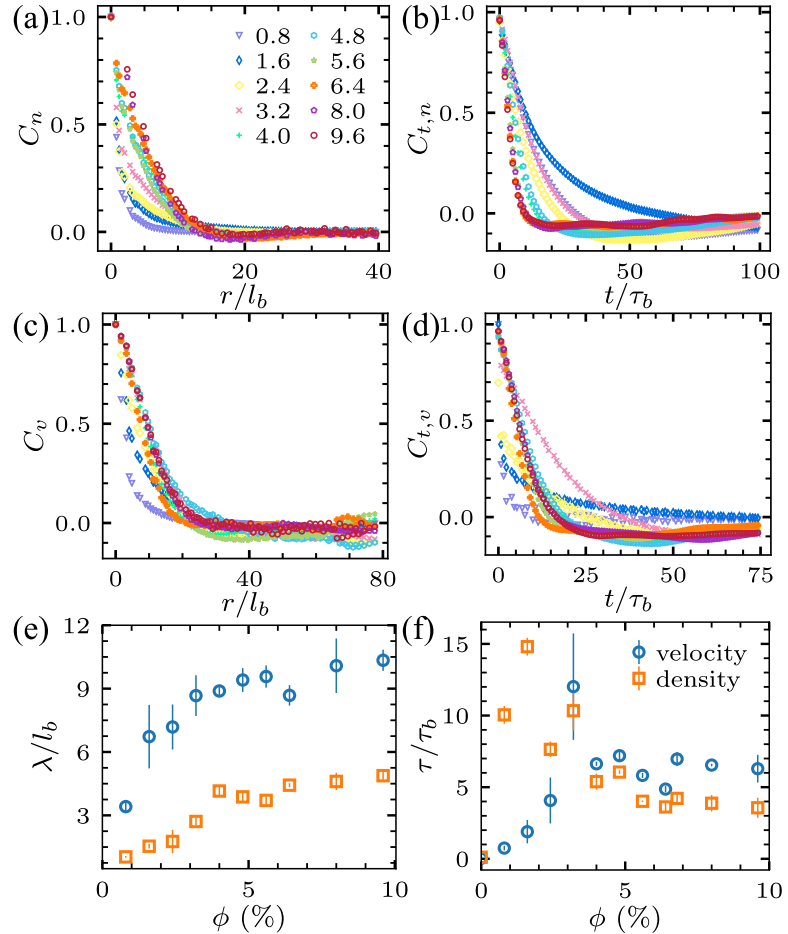


**Figure 5.6: Spatial and temporal correlations functions of density and velocity in active turbulence.** (a) Two-point density correlations at different bacterial volume fractions  $\phi$ . Radial position  $r$  is normalized by the average length of bacteria  $l_b = 3 \mu\text{m}$ . (b) Density autocorrelations at different  $\phi$ . Time  $t$  is normalized by the characteristic swimming time of bacteria  $\tau_b = 0.2 \text{ s}$ . (c) Two-point velocity correlations at different  $\phi$ . (d) Velocity autocorrelations at different  $\phi$ .  $\phi$  (%) of different curves are indicated in (a). (e) Density and velocity correlation lengths,  $\lambda$ , versus  $\phi$ . (f) Density and velocity correlation times,  $\tau$ , versus  $\phi$ . The error bars in (e) and (f) represent the standard deviations of measurements over 3 independent experiments.

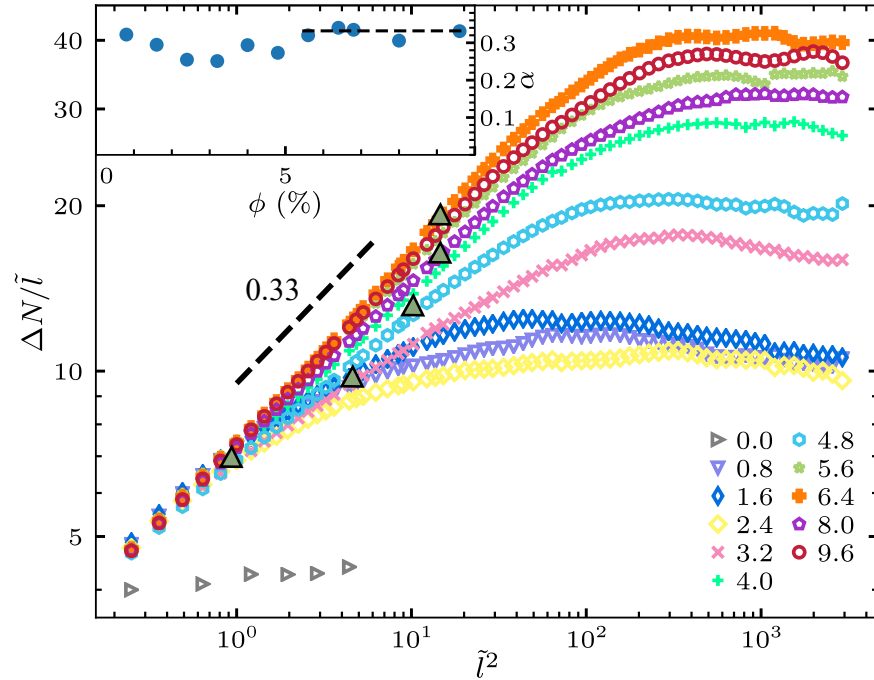


Figure 5.7: Density fluctuations of bacterial suspensions of different volume fractions  $\phi$ . The standard deviation of bacterial number  $\Delta N$  in a subsystem of length  $l$  as a function of the area of the subsystem  $l^2$ .  $\Delta N$  is normalized by the length of the subsystem  $l$ , which is proportional to the square root of bacterial number in the subsystem  $\sqrt{N}$ .  $l$  is presented in a dimensionless form,  $\tilde{l} = l/l_b$ , where  $l_b = 3 \mu\text{m}$  is the average length of bacteria. Dark green triangles indicate the density correlation lengths  $\lambda(\phi)$  from Fig. 5.6e. The black dashed line indicates a power-law scaling of 0.33. Inset: Scaling exponent  $\alpha$  versus  $\phi$ .  $\alpha$  are extracted by fitting the experimental data from  $0.3l_b$  to  $\lambda(\phi)$ . The dashed line in the inset indicates the theoretical prediction of  $\alpha = 1/3$ .

$N^\alpha$ .  $\alpha = 0$  for equilibrium systems obeying the central limit theorem, whereas the upper bound  $\alpha = 0.5$  corresponds to a system with maximal density fluctuations. We extract  $\alpha$  by fitting the experimental curves with power-law relations only below the density correlation length  $\lambda$ . The inset of Fig. 5.7 shows  $\alpha$  as a function of  $\phi$ .

At all volume fractions,  $\alpha$  takes a value of  $0.30 \pm 0.03$ . Notably, at high volume fractions, when  $\phi \geq \phi_h = 6.4\%$ ,  $\alpha$  approaches a narrower plateau of  $0.33 \pm 0.01$ .

The plateau value quantitatively agrees with the theoretical prediction of  $\alpha = 1/3$  for 3D suspensions of polar-ordered self-propelled particles with hydrodynamic interactions [19]. As such, our experiments provide the first quantitative verification of the theory of GNF in 3D wet active fluids.

The observation of GNF at volume fractions lower than  $\phi_c$  suggests that even in a dilute suspension below the turbulent transition, bacteria swim in a correlated fashion, in qualitative agreement with the prediction of the kinetic theory [173].

### 5.3.2 Energy Spectra

Similar to GNF, the velocity field of active turbulence also shows scale-dependent structures, which are often characterized by the energy spectrum of turbulent flows,  $E(k)$ .  $E(k)$  measures the kinetic energy density at different scales in terms of wavenumber  $k = 2\pi/l$ . It is related to the mean kinetic energy density by  $\langle \mathbf{v}^2 \rangle/2 = \langle v_x^2 + v_y^2 \rangle/2 = \int_0^\infty E(k)dk$ . Figure 5.8 shows  $E(k)$  of bacterial suspensions at different  $\phi$ . In the dilute suspension of  $\phi = 0.8\%$ ,  $E(k)$  is independent of  $k$  in the small  $k$  limit and then decreases at high  $k$ . The oscillation observed at high  $k$  likely arises from PIV errors due to the small number of bacteria in each PIV box of low- $\phi$  suspensions. With increasing  $\phi$ ,  $E(k)$  at small  $k$  increases sharply. In the turbulent regime at high  $\phi$ , the kinetic energy is concentrated at scales much larger than the size of single bacteria, even though the turbulent flow is entirely driven by the swimming of single bacteria. The overall trend

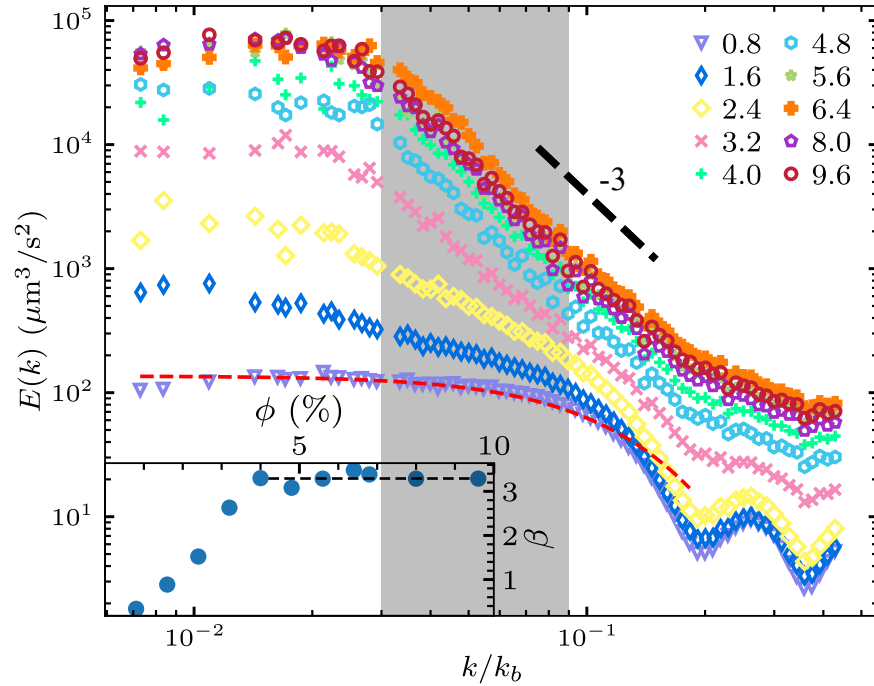


Figure 5.8: Energy spectra  $E(k)$  of bacterial suspensions of different volume fractions  $\phi$ . Shaded region indicates the range over which the scaling exponent  $\beta$  is fitted. The black dashed line indicates a power-law scaling of  $-3$ . The red dashed line is a fitting of  $E(k)$  at  $\phi = 0.8\%$  using Eq. 5.7. In the fitting, the bacterial number density  $n = \phi V_b$  and the dipole length  $l_d = 1.9 \mu\text{m}$  are from experiments, whereas the dipole strength  $\kappa = 100 \mu\text{m}^3/\text{s}$  and the regularization length  $\epsilon = 14 \mu\text{m}$  are taken as fitting parameters. In comparison,  $\kappa = 300.8 \mu\text{m}^3/\text{s}$  from experiments (see text). Inset: Scaling exponent of  $E(k)$ ,  $\beta$ , as a function of  $\phi$ . Dashed line indicates  $\beta = 3.3$ .

of  $E(k)$  with increasing  $\phi$  qualitatively agrees with the results from large-scale particle simulations [92, 103].

$E(k)$  of low- $\phi$  suspensions with uncorrelated pusher swimmers has been predicted [103]

$$E(k) = 4\pi n \kappa^2 \left[ \frac{1}{3} + \frac{\cos(kl_d)}{(kl_d)^2} - \frac{\sin(kl_d)}{(kl_d)^3} \right] \frac{\epsilon^4 k^2}{l_d^2} K_2^2(k\epsilon), \quad (5.7)$$

where  $n$  is the number density of bacteria,  $\kappa$  is the dipole strength and  $l_d$  is the dipolar length of *E. coli*.  $\epsilon$  is the distance for the regularization of the dipolar flow field.  $K_2$  is the modified Bessel function of the second kind. The fitting of Eq. 5.7 agrees well with our experimental  $E(k)$  at low  $\phi$  in the small  $k$  limit (Fig. 5.8). Particularly, Eq. 5.7 dictates that  $E(k)$  is flat as  $k \rightarrow 0$ , a key feature confirmed by our experiments. A simple dimensional analysis can show that the plateau  $E(k)$  at the small  $k$  follows  $\lim_{k \rightarrow 0} E(k) \sim n\kappa^2$  for uncorrelated swimmers of density  $n$ . The dipole strength can be estimated as  $\kappa = Fl_d/\eta = \xi v_{old}/\eta = 300.8 \mu\text{m}^3/\text{s}$ , where  $\eta$  is the viscosity of the buffer.  $\xi$  is the drag coefficient of a bacterial body orientated along its major axis, which can be calculated based on the body geometry  $\xi = 3\pi\eta w_b [1 - (1 - l_b/w_b)/5]$  [202].  $l_d = 1.9 \mu\text{m}$  is taken from direct measurements [117]. Thus,  $\lim_{k \rightarrow 0} E(k) \approx 7 \times 10^2 \mu\text{m}^3/\text{s}$ , within the same order of magnitude of our experiments. The discrepancy between Eq. 5.7 and experiments at large  $k$  may arise from the strong bacterial correlation at small length scales as shown by density fluctuations as well as the PIV errors.

We also extract the scaling exponent  $\beta$  of  $E(k) \sim k^{-\beta}$  by fitting the energy spectra at intermediate  $k$ , where a significant change of  $E(k)$  with  $\phi$  occurs and  $E(k)$  exhibits good power-law relations.  $\beta$  increases with  $\phi$  and saturates around 3 at high  $\phi > \phi_c$  (Fig. 5.8 inset). The saturated scaling exponent quantitatively agrees with previous experimental results obtained from the active turbulence of high-concentration sperm suspensions and *B. subtilis* suspensions at large  $k$  [21, 199]. At small  $k$ ,  $E(k)$  reported in Ref. [21] decreases with decreasing  $k$  and exhibits a non-monotonic trend, different

from the result in this work. Such discrepancy is attributed to the confined geometry used in [21], which limits the size of turbulent vortices and thus leads to a decrease of  $E(k)$  at small  $k$  [141]. The large system size of  $L = 140 \mu\text{m}$  of our experiments allows us to probe the small  $k$  limit predicted by theories and simulations without the influence of system boundaries.

Although the scaling in the small  $k$  limit is strongly affected by the system size, the scaling in the large  $k$  limit seems to be universal with  $\beta \approx 3$  from different experiments. To the best of our knowledge, no theoretical prediction has been made on this universal scaling behavior for 3D active turbulence. Giomi investigated the energy spectra of 2D active nematics by combining numerical simulations with mean-field theories and showed  $E(k) \sim k^{-4}$  in the large  $k$  limit [102]. The result has also been confirmed recently by a hydrodynamic theory [198]. For isotropic turbulence in  $d$  dimension, the energy spectra can be written as  $E(k) = C_d k^{d-1} \langle \mathbf{v}(\mathbf{k}) \cdot \mathbf{v}(-\mathbf{k}) \rangle_{k=|\mathbf{k}|}$  [21, 103], where  $C_d k^{d-1}$  is the surface area of  $(d-1)$ -sphere and  $\langle \mathbf{v}(\mathbf{k}) \cdot \mathbf{v}(-\mathbf{k}) \rangle_{k=|\mathbf{k}|}$  is the Fourier transform of the velocity-velocity spatial correlation function. If the velocity correlation function for 2D active nematics is qualitatively similar to that of 3D bacterial suspensions independent of the dimensionality of systems, the mean-field theory would then predict a scaling of  $E(k) \sim k^{-3}$ , consistent with experimental observations. Such a hypothesis, although intriguing, is certainly non-trivial and needs further theoretical investigation.

### 5.3.3 Density-Flow Coupling

Both GNF and energy spectra probe the scale dependence of active turbulence. The former measures density fluctuations at different scales, whereas the latter considers flow energies across scales. Although both properties have been extensively studied, the coupling between the two has not been explicitly examined so far. The GNF curves and energy spectra shown in Fig. 5.7 and 5.8 show similar characteristics, including the rapid

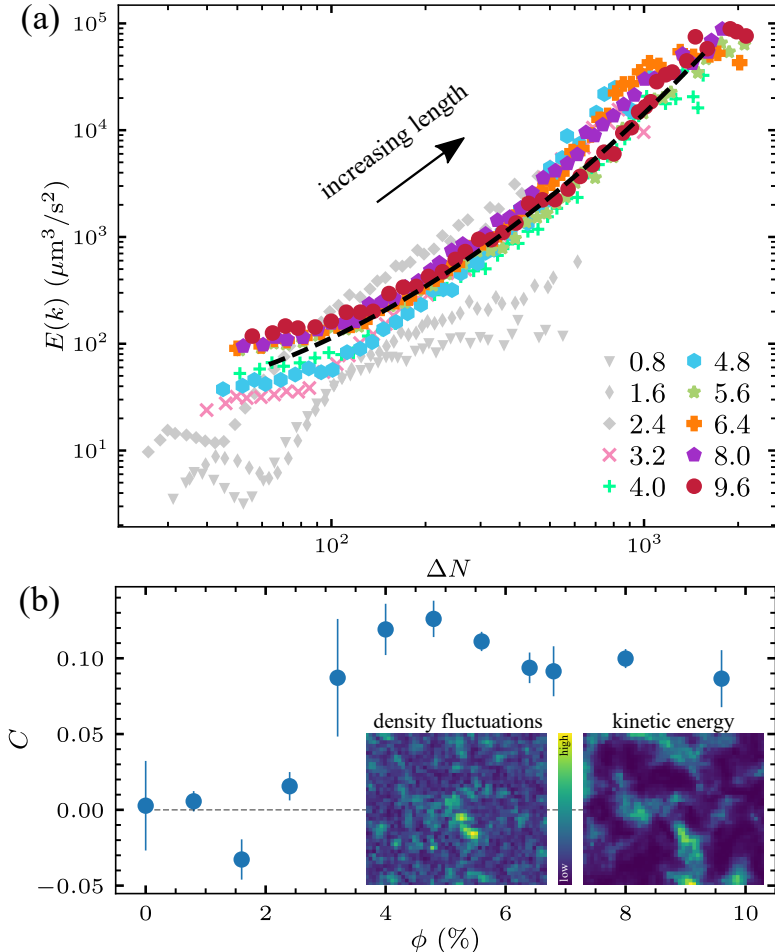


Figure 5.9: The coupling between density fluctuations and kinetic energies in the steady state. (a) Energy spectra  $E(k)$  plotted against number density fluctuations  $\Delta N$  at each corresponding length scale for bacterial suspensions of different volume fractions  $\phi$ . Gray symbols are used for low- $\phi$  suspensions without active turbulence. The black dashed line is a polynomial fitting of the master curve, serving as a guide for the eye. The black arrow indicates the direction of increasing lengths. (b) Correlation of local density fluctuations and kinetic energies  $C$  as a function of  $\phi$ .  $C$  is averaged over 1000 frames in steady state, and the error bars represent the standard deviations. Inset: Density fluctuation and kinetic energy fields in a bacterial suspension of  $\phi = 4.8\%$ .

increase at small length scale and plateaus at large length scale. Such similarity suggests that a density-independent correlation between density fluctuations and kinetic energies may exist across all different length scales. Indeed, when we plot density fluctuations  $\Delta N$  against the corresponding kinetic energies  $E$  at the same scale in Fig. 5.9a, all the  $\Delta N-E$  pairs fall onto a universal curve over two orders of magnitude in scales extending from the size of single PIV boxes to the vortex size in the turbulent regime, regardless of the specific volume fractions of the samples. In contrast,  $\Delta N-E$  shows much larger scattering for low  $\phi$  suspensions with random swimming bacteria. Although it is not surprising that density fluctuations correlate with kinetic energies in general as both measure different aspects of the same active turbulence, the collapse of data from samples of different volume fractions is still quite unexpected. The results show that the coupling between density fluctuations and turbulent flows occur at every scale of active turbulence in a quantitative same fashion. Such a scale-invariant coupling is independent of the volume fraction of bacterial suspensions. A phenomenological fitting of the universal coupling between density fluctuations and kinetic energy is shown in Fig. 5.9a by a black dashed line.

To further illustrate such an unusual coupling in real space, we measure the *local* correlation of density fluctuations and kinetic energy at a randomly chosen small scale of  $l = 2.5l_b$ . The local density fluctuation  $\delta N(\mathbf{r}, t)$  and local kinetic energy  $E(\mathbf{r}, t)$  at position  $\mathbf{r} = (x, y)$  and time  $t$  are extracted from the image intensity field and the PIV velocity field, respectively (Fig. 5.9b inset). The normalized correlation between  $\delta N(\mathbf{r}, t)$  and  $E(\mathbf{r}, t)$  is then computed at different  $\phi$  (Fig. 5.9b). At low  $\phi$  with random swimming bacteria, the correlation is weak fluctuating around zero, which then increases with  $\phi$  as bacterial suspensions transition to active turbulence. A constant positive correlation is found in the turbulent regime when  $\phi \geq \phi_c$ . The real-space measurement provides a concrete example of the coupling between density fluctuations and turbulent flows at

small scales.

Moreover, we find that the same density-energy coupling also exists in the kinetic process during the transition towards bacterial turbulence. Taking the advantage of the light-powered bacteria, we trigger the onset of bacterial turbulence by suddenly turning on the light illumination on high- $\phi$  bacterial suspensions at  $t = 0$  [2]. The temporal evolution of density fluctuations and turbulent flows in a bacterial suspension of  $\phi = 6.4\%$  during the kinetic process is illustrated in Fig. 5.10a. At  $t = 0$ , the flow velocities are close to 0. The suspension shows no sign of density fluctuations. At  $t = 40$  s, although the magnitudes of velocities are still small, local alignment of velocity directions can be clearly observed, which gives rise to the characteristic pattern of vortices and jets of active turbulence. Weak density fluctuations start to emerge. At  $t = 103$  s, the magnitudes of velocities grow significantly and saturate. The suspension reaches the steady state of active turbulence with strong density fluctuations. Note that the response time of individual bacteria is much shorter than the emergence of collective flows.

In Fig. 5.10b, the evolution of the scaling exponent  $\alpha$  is shown as a function of  $t$ . It grows relatively fast at the beginning and shows a saturation at  $\sim 60$  s. The growth of both  $\alpha$  and the large scale kinetic energy  $\langle \mathbf{v}^2 \rangle / 2$  are significantly delayed compared with the formation of collective flows, which is quantified by the area fraction of the regions with strong alignment of local velocities  $M$  [2]. The finding provides strong experimental support to an important prediction of the kinetic theory of active fluids [66, 81], where the density fluctuation arises due to the nonlinear coupling between collective flows and particle densities. At the onset of hydrodynamic instability in the linear regime, when velocities are largely aligned but flow strength is low, GNF is not very pronounced, as confirmed by our experiments at early times.

By comparing the temporal evolution of both GNF and energy spectra during the

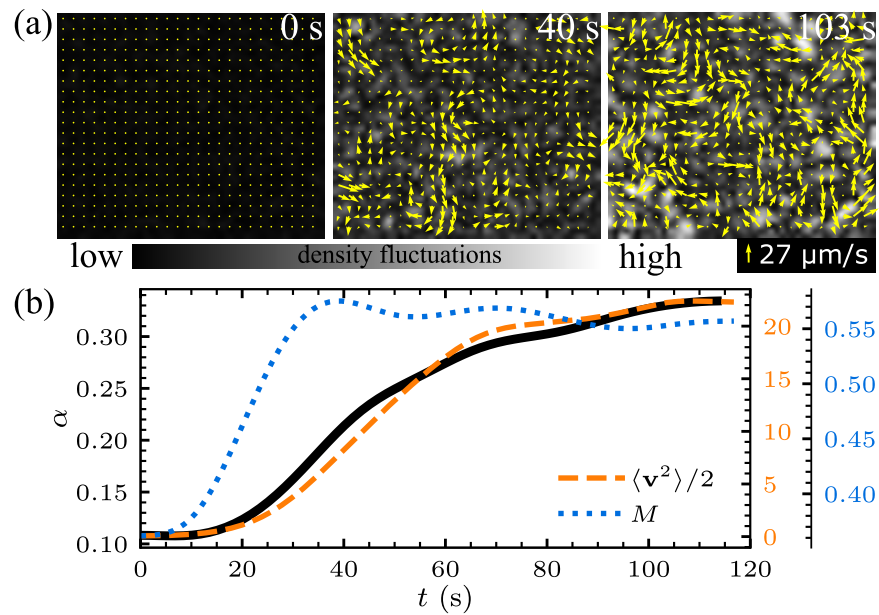
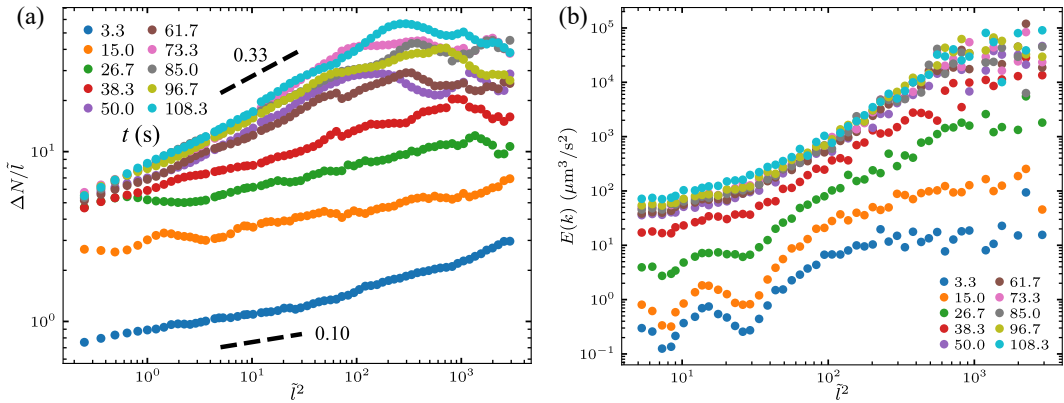
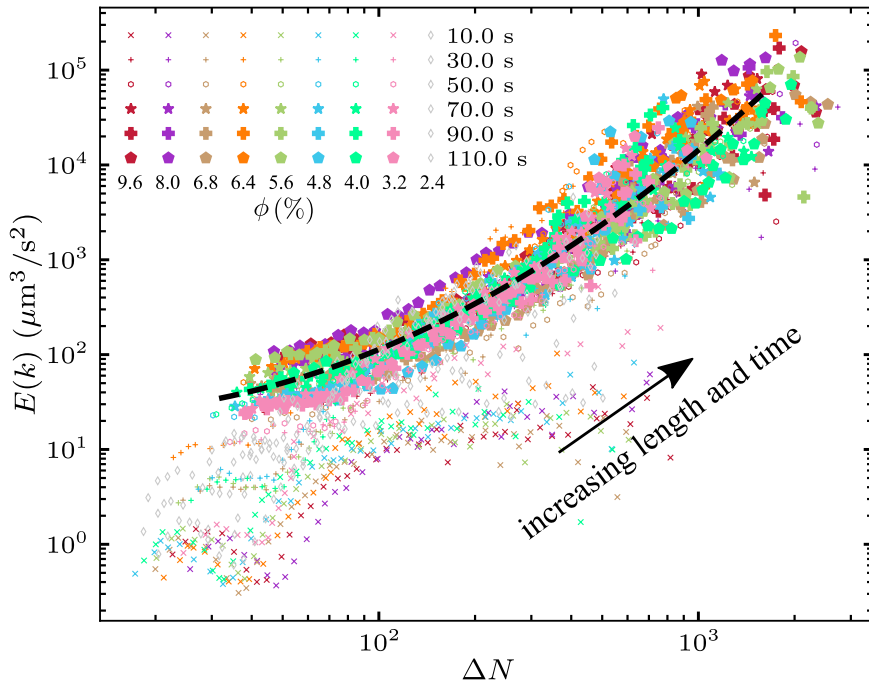


Figure 5.10: **Temporal evolution of  $\alpha$ , flow kinetic energy  $\langle v^2 \rangle / 2$  and fraction of aligned flow region  $M$ .** (a) Snapshots of density fluctuation evolution during the transition towards active turbulence, overlaid with velocity fields obtained from PIV analysis. At  $t = 0$  s, we turn on the illumination light and the bacteria start to gain speed. Times are labeled in corresponding images ( $\phi = 6.4\%$ ). (b) Temporal evolution of scaling exponent  $\alpha$ , total kinetic energy  $E$  and the region fraction of aligned velocity  $M$  in the same sample.



**Figure 5.11: Evolution of GNF and energy spectra during the turbulent transition.** (a) Number density fluctuations  $\Delta N$  and (b) energy spectra  $E(k)$  as functions of subsystem size  $l^2$  at different times over the turbulence transition of the same bacterial suspension.  $\Delta N$  is normalized by the length of subsystems  $l$ , similar to that in Fig. 5.7.  $\tilde{l} = l/l_b$ . This particular sample has a volume fraction  $\phi = 6.4$ .  $t$  is indicated by the legends, in units of seconds.

turbulence transition as shown in Fig. 5.11a and b, we find that they are analogous in at least two ways. First, both quantities reach a saturation at  $\sim 60$  s. Second, both quantities grow faster at large length scales. Such analogies indicate that GNF and kinetic energy are closely coupled not only in the steady state of active turbulence, but also during the transient state in the transition to active turbulence. Motivated by this observation, we plot  $\Delta N$  and  $E(k)$  in the same axis for samples of different volume fractions, at different times and length scales  $l$  collapse into the same master curve obtained from the steady-state measurements. These kinetic measurements further suggest that the rise of GNF is governed by the kinetic energy at each corresponding scale.



**Figure 5.12: Density flow coupling during the transition towards active turbulence.** Kinetic energy  $E(k)$  at various length scales is plotted against number fluctuations  $\Delta N$  at corresponding length scales for bacterial suspensions at volume fractions ranging from 2.4% to 9.6% at different times. Different colors indicate samples of different volume fractions. The size and the shape of the markers indicate the time. Small markers stand for early times and large markers stand for late times. The black dashed line is the same master curve as shown in Fig. 5.9a. In this plot, length scale and time are hidden variables, and their direction of evolving is indicated by a black arrow.

## 5.4 Conclusion

We have conducted systematic experiments measuring density fluctuations and energy spectra of 3D bacterial suspensions over a wide range of concentrations in both steady and transient states. We illustrated the scaling behavior of giant number fluctuations in bulk bacterial suspensions and showed that such a scaling persisted at small scales even in low-concentration suspensions well before the transition to active turbulence. The finding provided new experimental evidence on the existence of local spatial and temporal correlations between bacteria in dilute suspensions due to the long-range hydrodynamic interactions unique to 3D wet active fluids. In addition, we also examined the energy spectra of bacterial suspensions of different concentrations and showed the spectral properties of the active turbulence of dense bacterial suspensions in the bulk limit. Lastly, by comparing density fluctuations and energy spectra at different scales, we revealed an unexpected coupling between density fluctuations and kinetic energies across more than one order of magnitude of length scales from the scale of single bacteria up to the size of the system. We further showed that such a density-independent and scale-invariant coupling also dominated the kinetic process during the transition towards bacterial active turbulence.

Our experiments also verified several important theoretical predictions on 3D wet active fluids:

1. The scaling behavior of density fluctuations observed in our experiments

$$\Delta N/\sqrt{N} \sim N^{0.33}$$

quantitatively agreed with the theoretical prediction on the giant number fluctuations of 3D suspensions of polar-ordered self-propelled particles [19].

2. The energy spectra of low-concentration bacterial suspensions measured in our study confirmed the key feature of the predicted energy spectra of uncorrelated pusher swimmers in the small wavenumber limit [103].
3. The delayed onset of density fluctuations uncovered in our experiments supported the central prediction of the kinetic theories on the nonlinear development of the hydrodynamic instability of pusher suspensions [66, 81].

Thus, our study provided a comprehensive experimental benchmark on the density fluctuations and energy spectra of bulk bacterial suspensions and shed new light onto the emergent dynamics of 3D wet active fluids.

# Chapter 6

## Summary and Outlook

### 6.1 Summary

In this thesis, I described my investigations on the rheological properties of active fluids and the collective motions of the active swimmers, using *E. coli* suspensions as a model system. Due to self-propulsion, active fluids exhibit unusual interplay with system boundaries, and self-organize into complicated patterns, which are absent in equilibrium systems.

We used a microfluidic viscometer to study the confinement effect on the viscosity of active fluids. We showed that such a confinement effect arises from the interplay between bacterial motility and confining surfaces. We found that the upstream swimming bacteria near the boundaries played a key role in the confinement effect on the viscosity of bacterial suspensions. We developed a simple model based on this observation, which showed a qualitative agreement with our rheological and microscopic dynamics measurements.

We further studied active turbulence—arguably the most intriguing phenomenon in active fluids—using a light-powered *E. coli* mutant strain. Our systematic experiments

explored a large parameter space and identified the phase boundaries between disordered and ordered states. We also uncovered the kinetics of the transition into active turbulence, which strongly supported the predictions of the kinetic theories.

We also studied the giant number fluctuations and the energy spectra are systematically studied. Both measurements provided supporting evidence for several predictions of the kinetic theories and other models. Our experimental results also revealed a strong coupling between GNF and energy spectra, deepening the understanding of the microscopic origin of the GNF, the landmark phenomenon of active fluids.

Our work provides a deeper understanding on the self-organization of active constituents in active fluids, as well as its consequences on the macroscopic properties and collective behavior of active fluids, and lays the foundation of engineering machines composed of active constituents which mimics the properties of real living matter.

## 6.2 Outlook

*E. coli* bacteria have served as a great model swimmer for active fluid experiment, for their robustness and ease to cultivate. However, assuming they are just reckless swimmers is sometimes not appropriate, since they are ultimately microorganisms and are certainly more complex than what we expect. We describe their swimming as “run-and-tumble” fashion, but in fact, their motion can be highly correlated with the environment, which is affected by chemotaxis, gyrotaxis, rheotaxis, etc.. We have always been looking at these bacteria from a pure physical point of view, and have been encouraged that some seemingly biological processes, such as the collective motions, are indeed governed by physical principles. In other times when physical principles don’t capture a phenomenon, however, we will have to incorporate the biological aspects of them.

Due to the above reasons, in the future investigations on biological active fluids, the biological aspects of the swimmers need to be properly accounted for. For pure physics

study, the rapid growth of artificial swimmers, such as chemical reaction driven Janus particles and electric field driven Quincke rollers, can serve as a better model system since they are much simpler than *E. coli* and thus behave in a less complex way. These two directions will bring us closer to the ultimate goal of active matter study—to better understand the biological and ecological significance of animal behavior and to have real world applications.

# Bibliography

- [1] Zhengyang Liu, Kechun Zhang, and Xiang Cheng. Rheology of bacterial suspensions under confinement. *Rheologica Acta*, 58(8):439–451, 2019.
- [2] Yi Peng, Zhengyang Liu, and Xiang Cheng. Imaging the emergence of bacterial turbulence using light-powered *Escherichia coli*. *arXiv*, 2020, 2003.12399.
- [3] Zhengyang Liu, Wei Zeng, Xiaolei Ma, and Xiang Cheng. Density fluctuations and energy spectra of 3d bacterial suspensions. *arXiv*, 2020, 2012.13680.
- [4] John Toner, Yuhai Tu, and Sriram Ramaswamy. Hydrodynamics and phases of flocks. *Annals of Physics*, 318(1):170–244, 2005.
- [5] Sriram Ramaswamy. The Mechanics and Statistics of Active Matter. *Annual Review of Condensed Matter Physics*, 1(1):323–345, 2010.
- [6] Tamás Vicsek and Anna Zafeiris. Collective motion. *Physics Reports*, 517(3):71 – 140, 2012. Collective motion.
- [7] M. C. Marchetti, J. F. Joanny, S. Ramaswamy, T. B. Liverpool, J. Prost, Madan Rao, and R. Aditi Simha. Hydrodynamics of soft active matter. *Reviews of Modern Physics*, 85(3):1143–1189, 2013.

- [8] David Saintillan and Michael J. Shelley. Active suspensions and their nonlinear models. *Comptes Rendus Physique*, 14(6):497–517, 2013.
- [9] Clemens Bechinger, Roberto Di Leonardo, Hartmut Löwen, Charles Reichhardt, Giorgio Volpe, and Giovanni Volpe. Active particles in complex and crowded environments. *Reviews of Modern Physics*, 88(4), 2016.
- [10] F. Jülicher, K. Kruse, J. Prost, and J.-F. Joanny. Active behavior of the cytoskeleton. *Physics Reports*, 449(1):3–28, 2007.
- [11] P. G. de Gennes. Soft matter. *Rev. Mod. Phys.*, 64:645–648, 1992.
- [12] Sharon C. Glotzer. Editorial: Soft Matters. *Physical Review Letters*, 114:050001, 2015.
- [13] Jesse L. Silverberg, Matthew Bierbaum, James P. Sethna, and Itai Cohen. Collective motion of humans in mosh and circle pits at heavy metal concerts. *Physical Review Letters*, 110:228701, 2013.
- [14] Stephen J. DeCamp, Gabriel S. Redner, Aparna Baskaran, Michael F. Hagan, and Zvonimir Dogic. Orientational order of motile defects in active nematics. *Nature Materials*, 14(11):1110–1115, 2015.
- [15] Jeremie Palacci, Stefano Sacanna, Asher Preska Steinberg, David J. Pine, and Paul M. Chaikin. Living crystals of light-activated colloidal surfers. *Science*, 339(6122):936–940, 2013.
- [16] B. A. Finlayson and L. E. Scriven. Convective instability by active stress. *Proc. Roy. Soc. A.*, 301(1501):183–219, 1969.

- [17] Tamás Vicsek, András Czirók, Eshel Ben-Jacob, Inon Cohen, and Ofer Shochet. Novel type of phase transition in a system of self-driven particles. *Physical Review Letters*, 75:1226–1229, 1995.
- [18] Yashodhan Hatwalne, Sriram Ramaswamy, Madan Rao, and R. Aditi Simha. Rheology of active-particle suspensions. *Physical Review Letters*, 92:118101, 2004.
- [19] R. Aditi Simha and Sriram Ramaswamy. Hydrodynamic fluctuations and instabilities in ordered suspensions of self-propelled particles. *Physical Review Letters*, 89:058101, 2002.
- [20] Christopher Dombrowski, Luis Cisneros, Sunita Chatkaew, Raymond E. Goldstein, and John O. Kessler. Self-concentration and large-scale coherence in bacterial dynamics. *Physical Review Letters*, 93:098103, 2004.
- [21] Henricus H. Wensink, Jörn Dunkel, Sebastian Heidenreich, Knut Drescher, Raymond E. Goldstein, Hartmut Löwen, and Julia M. Yeomans. Meso-scale turbulence in living fluids. *Proceedings of the National Academy of Sciences of the United States of America*, 109(36):14308–14313, 2012.
- [22] Salima Rafaï, Levan Jibuti, and Philippe Peyla. Effective viscosity of microswimmer suspensions. *Physical Review Letters*, 104:098102, 2010.
- [23] Andrey Sokolov, Raymond E. Goldstein, Felix I. Feldchtein, and Igor S. Aranson. Enhanced mixing and spatial instability in concentrated bacterial suspensions. *Physical Review E*, 80(3):1–8, 2009.
- [24] Jérémie Gachelin, Gastón Miño, Hélène Berthet, Anke Lindner, Annie Rousselet, and Éric Clément. Non-newtonian viscosity of escherichia coli suspensions. *Physical Review Letters*, 110:268103, 2013.

- [25] Héctor Matías López, Jérémie Gachelin, Carine Douarche, Harold Auradou, and Eric Clément. Turning bacteria suspensions into superfluids. *Physical Review Letters*, 115:028301, 2015.
- [26] Sriram Ramaswamy. Active fluids. *Nature Reviews Physics*, 1(11):640–642, 2019.
- [27] A. I. Curatolo, N. Zhou, Y. Zhao, C. Liu, A. Daerr, J. Tailleur, and J. Huang. Cooperative pattern formation in multi-component bacterial systems through reciprocal motility regulation. *Nature Physics*, 2020.
- [28] David Saintillan. Rheology of active fluids. *Annual Review of Fluid Mechanics*, 50(1):563–592, 2018.
- [29] Xiao-Lun Wu and Albert Libchaber. Particle diffusion in a quasi-two-dimensional bacterial bath. *Physical Review Letters*, 84:3017–3020, 2000.
- [30] Yi Peng, Lipeng Lai, Yi-Shu Tai, Kechun Zhang, Xinliang Xu, and Xiang Cheng. Diffusion of ellipsoids in bacterial suspensions. *Physical Review Letters*, 116:068303, 2016.
- [31] Avi Caspi, Rony Granek, and Michael Elbaum. Enhanced Diffusion in Active Intracellular Transport. *Physical Review Letters*, 85:5655–5658, 2000.
- [32] Alexander Morozov and Davide Marenduzzo. Enhanced diffusion of tracer particles in dilute bacterial suspensions. *Soft Matter*, 10(16):2748–2758, 2014.
- [33] Alison E. Patteson, Arvind Gopinath, Prashant K. Purohit, and Paulo E. Arratia. Particle diffusion in active fluids is non-monotonic in size. *Soft Matter*, 12(8):2365–2372, 2016.

- [34] Kyriacos C. Leptos, Jeffrey S. Guasto, J. P. Gollub, Adriana I. Pesci, and Raymond E. Goldstein. Dynamics of enhanced tracer diffusion in suspensions of swimming eukaryotic microorganisms. *Physical Review Letters*, 103:198103, 2009.
- [35] Ou Yang, Yi Peng, Zhengyang Liu, Chao Tang, Xinliang Xu, and Xiang Cheng. Dynamics of ellipsoidal tracers in swimming algal suspensions. *Phys. Rev. E*, 94:042601, 2016.
- [36] Chantal Valeriani, Martin Li, John Novosel, Jochen Arlt, and Davide Marenduzzo. Colloids in a bacterial bath: Simulations and experiments. *Soft Matter*, 7(11):5228–5238, 2011.
- [37] Hüseyin Kurtuldu, Jeffrey S. Guasto, Karl A. Johnson, and J. P. Gollub. Enhancement of biomixing by swimming algal cells in two-dimensional films. *Proceedings of the National Academy of Sciences of the United States of America*, 108(26):10391–10395, 2011.
- [38] M. Cristina Marchetti. Soft matter: Frictionless fluids from bacterial teamwork. *Nature*, 525(7567):37–39, 2015.
- [39] Luca Giomi, Tanniemola B. Liverpool, and M. Cristina Marchetti. Sheared active fluids: Thickening, thinning, and vanishing viscosity. *Physical Review E*, 81:051908, 2010.
- [40] A. Einstein. Eine neue bestimmung der moleküldimensionen. *Annalen der Physik*, 324(2):289–306, 1906.
- [41] Dieter Forster. Microscopic theory of flow alignment in nematic liquid crystals. *Physical Review Letters*, 32:1161–1164, 1974.

- [42] J. Tailleur and M. E. Cates. Statistical mechanics of interacting run-and-tumble bacteria. *Physical Review Letters*, 100:218103, 2008.
- [43] S. C. Takatori and J. F. Brady. Superfluid Behavior of Active Suspensions from Diffusive Stretching. *Physical Review Letters*, 118:018003, 2017.
- [44] Antoine Bricard, Jean Baptiste Caussin, Nicolas Desreumaux, Olivier Dauchot, and Denis Bartolo. Emergence of macroscopic directed motion in populations of motile colloids. *Nature*, 503(7474):95–98, 2013.
- [45] R. Voituriez, J. F. Joanny, and J. Prost. Spontaneous flow transition in active polar gels. *Europhysics Letters*, 70(3):404–410, 2005.
- [46] Miha Ravnik and Julia M. Yeomans. Confined active nematic flow in cylindrical capillaries. *Physical Review Letters*, 110:026001, 2013.
- [47] H Wioland, E Lushi, and R E Goldstein. Directed collective motion of bacteria under channel confinement. *New Journal of Physics*, 18(7):075002, 2016.
- [48] Kun-Ta Wu, Jean Bernard Hishamunda, Daniel T. N. Chen, Stephen J. DeCamp, Ya-Wen Chang, Alberto Fernández-Nieves, Seth Fraden, and Zvonimir Dogic. Transition from turbulent to coherent flows in confined three-dimensional active fluids. *Science*, 355(6331), 2017.
- [49] Francis G. Woodhouse and Raymond E. Goldstein. Spontaneous circulation of confined active suspensions. *Physical Review Letters*, 109:168105, 2012.
- [50] Hugo Wioland, Francis G. Woodhouse, Jörn Dunkel, John O. Kessler, and Raymond E. Goldstein. Confinement stabilizes a bacterial suspension into a spiral vortex. *Physical Review Letters*, 110:268102, 2013.

- [51] Enkeleida Lushi, Hugo Wioland, and Raymond E. Goldstein. Fluid flows created by swimming bacteria drive self-organization in confined suspensions. *Proceedings of the National Academy of Sciences of the United States of America*, 111(27):9733–9738, 2014.
- [52] Andrey Sokolov, Mario M. Apodaca, Bartosz A. Grzybowski, and Igor S. Aranson. Swimming bacteria power microscopic gears. *Proceedings of the National Academy of Sciences of the United States of America*, 107(3):969–974, 2010.
- [53] Alex E. Hamby, Dhruv K. Vig, Sasha Safonova, and Charles W. Wolgemuth. Swimming bacteria power microspin cycles. *Science Advances*, 4(12), 2018.
- [54] Roberto Alonso-Matilla, Barath Ezhilan, and David Saintillan. Microfluidic rheology of active particle suspensions: Kinetic theory. *Biomicrofluidics*, 10(4):18–26, 2016.
- [55] Jonasz Słomka and Jörn Dunkel. Geometry-dependent viscosity reduction in sheared active fluids. *Physical Review Fluids*, 2:043102, 2017.
- [56] Y. Han, A. M. Alsayed, M. Nobili, J. Zhang, T. C. Lubensky, and A. G. Yodh. Brownian motion of an ellipsoid. *Science*, 314(5799):626–630, 2006.
- [57] Todd M. Squires and Thomas G. Mason. Fluid mechanics of microrheology. *Annual Review of Fluid Mechanics*, 42:413–438, 2010.
- [58] Patrick T. Underhill, Juan P. Hernandez-Ortiz, and Michael D. Graham. Diffusion and spatial correlations in suspensions of swimming particles. *Physical Review Letters*, 100:248101, 2008.
- [59] Zhi Lin, Jean Luc Thiffeault, and Stephen Childress. Stirring by squirmers. *Journal of Fluid Mechanics*, 669:167–177, 2011.

- [60] Ramin Golestanian. Anomalous diffusion of symmetric and asymmetric active colloids. *Physical Review Letters*, 102:188305, 2009.
- [61] D. T.N. Chen, A. W.C. Lau, L. A. Hough, M. F. Islam, M. Goulian, T. C. Lubensky, and A. G. Yodh. Fluctuations and rheology in active bacterial suspensions. *Physical Review Letters*, 99:148302, 2007.
- [62] Gastón Miño, Thomas E. Mallouk, Thierry Darnige, Mauricio Hoyos, Jeremi Dauchet, Jocelyn Dunstan, Rodrigo Soto, Yang Wang, Annie Rousselet, and Eric Clement. Enhanced diffusion due to active swimmers at a solid surface. *Physical Review Letters*, 106:048102, 2011.
- [63] G. L. Miño, J. Dunstan, A. Rousselet, E. Clément, and R. Soto. Induced diffusion of tracers in a bacterial suspension: Theory and experiments. *Journal of Fluid Mechanics*, 729:423–444, 2013.
- [64] T. V. Kasyap, Donald L. Koch, and Mingming Wu. Hydrodynamic tracer diffusion in suspensions of swimming bacteria. *Physics of Fluids*, 26:081901, 2014.
- [65] Craig W Reynolds. Flocks-Hers-and-Schools. *ACM SIGGRAPH Computer Graphics*, 21(4):25–34, 1987.
- [66] David Saintillan and Michael J. Shelley. Instabilities, pattern formation, and mixing in active suspensions. *Physics of Fluids*, 20(12):123304, 2008.
- [67] Vijay Narayan, Sriram Ramaswamy, and Narayanan Menon. Long-lived giant number fluctuations in a swarming granular nematic. *Science*, 317(5834):105–108, 2007.
- [68] Ashley J.W. Ward, David J.T. Sumpter, Iain D. Couzin, Paul J.B. Hart, and Jens Krause. Quorum decision-making facilitates information transfer in fish shoals.

- Proceedings of the National Academy of Sciences of the United States of America*, 105(19):6948–6953, 2008.
- [69] M. Ballerini, N. Cabibbo, R. Candelier, A. Cavagna, E. Cisbani, I. Giardina, V. Lecomte, A. Orlandi, G. Parisi, A. Procaccini, M. Viale, and V. Zdravkovic. Interaction ruling animal collective behavior depends on topological rather than metric distance: Evidence from a field study. *Proceedings of the National Academy of Sciences of the United States of America*, 105(4):1232–1237, 2008.
- [70] Jörn Dunkel, Sebastian Heidenreich, Knut Drescher, Henricus H. Wensink, Markus Bär, and Raymond E. Goldstein. Fluid dynamics of bacterial turbulence. *Physical Review Letters*, 110:228102, 2013.
- [71] Ivo Buttinoni, Julian Bialké, Felix Kümmel, Hartmut Löwen, Clemens Bechinger, and Thomas Speck. Dynamical clustering and phase separation in suspensions of self-propelled colloidal particles. *Physical Review Letters*, 110:238301, 2013.
- [72] Tim Sanchez, Daniel T.N. Chen, Stephen J. Decamp, Michael Heymann, and Zvonimir Dogic. Spontaneous motion in hierarchically assembled active matter. *Nature*, 491(7424):431–434, 2012.
- [73] Volker Schaller, Christoph Weber, Christine Semmrich, Erwin Frey, and Andreas R. Bausch. Polar patterns of driven filaments. *Nature*, 467(7311):73–77, 2010.
- [74] Andrey Sokolov, Igor S. Aranson, John O. Kessler, and Raymond E. Goldstein. Concentration dependence of the collective dynamics of swimming bacteria. *Physical Review Letters*, 98:158102, 2007.
- [75] Guillaume Grégoire and Hugues Chaté. Onset of Collective and Cohesive Motion. *Physical Review Letters*, 92:025702, 2004.

- [76] Hugues Chaté, Francesco Ginelli, Guillaume Grégoire, and Franck Raynaud. Collective motion of self-propelled particles interacting without cohesion. *Physical Review E*, 77:046113, 2008.
- [77] Francesco Ginelli, Fernando Peruani, Markus Bär, and Hugues Chaté. Large-scale collective properties of self-propelled rods. *Physical Review Letters*, 104:184502, 2010.
- [78] Sandrine Ngo, Anton Peshkov, Igor S. Aranson, Eric Bertin, Francesco Ginelli, and Hugues Chaté. Large-scale chaos and fluctuations in active nematics. *Physical Review Letters*, 113:038302, 2014.
- [79] Benoît Mahault, Francesco Ginelli, and Hugues Chaté. Quantitative Assessment of the Toner and Tu Theory of Polar Flocks. *Physical Review Letters*, 123:218001, 2019.
- [80] John Toner and Yuhai Tu. Long-range order in a two-dimensional dynamical XY model: How birds fly together. *Physical Review Letters*, 75:4326–4329, 1995.
- [81] David Saintillan and Michael J. Shelley. Instabilities and pattern formation in active particle suspensions: Kinetic theory and continuum simulations. *Physical Review Letters*, 100:178103, 2008.
- [82] Donald L. Koch and Ganesh Subramanian. Collective Hydrodynamics of Swimming Microorganisms: Living Fluids. *Annual Review of Fluid Mechanics*, 43(1):637–659, 2011.
- [83] Andrey Sokolov and Igor S. Aranson. Physical properties of collective motion in suspensions of bacteria. *Physical Review Letters*, 109:248109, 2012.

- [84] T. Ishikawa, N. Yoshida, H. Ueno, M. Wiedeman, Y. Imai, and T. Yamaguchi. Energy transport in a concentrated suspension of bacteria. *Physical Review Letters*, 107:028102, 2011.
- [85] Aparna Baskaran and M. Cristina Marchetti. Statistical mechanics and hydrodynamics of bacterial suspensions. *Proceedings of the National Academy of Sciences of the United States of America*, 106(37):15567–15572, 2009.
- [86] David Saintillan and Michael J. Shelly. *Theory of Active Suspensions*. Number Chapter 9. 2015.
- [87] John Toner and Yuhai Tu. Flocks, herds, and schools: A quantitative theory of flocking. *Physical Review E*, 58(4):4828–4858, 1998.
- [88] Yuhai Tu, John Toner, and Markus Ulm. Sound waves and the absence of galilean invariance in flocks. *Physical Review Letters*, 80:4819–4822, 1998.
- [89] S. Ramaswamy, R. Aditi Simha, and J. Toner. Active nematics on a substrate: Giant number fluctuations and long-time tails. *Europhysics Letters*, 62(2):196–202, 2003.
- [90] Shradha Mishra and Sriram Ramaswamy. Active nematics are intrinsically phase separated. *Physical Review Letters*, 97:090602, 2006.
- [91] Supravat Dey, Dibyendu Das, and R. Rajesh. Spatial structures and giant number fluctuations in models of active matter. *Physical Review Letters*, 108:238001, 2012.
- [92] David Saintillan and Michael J. Shelley. Emergence of coherent structures and large-scale flows in motile suspensions. *Journal of the Royal Society Interface*, 9(68):571–585, 2012.

- [93] I. Aranson, A. Snezhko, J. S. Olafsen, and J. S. Urbach3. Comment on “Long-Lived Giant equal size L and measured the number of particles Ni in each subsystem. The fluctuation in a given Number Fluctuations in a Swarming subsystem was calculated from the series of Ni versus time by measuring the mean square Granular Nematic”. *320*:612c, 2008.
- [94] H. P. Zhang, Avraham Be’er, E. L. Florin, and Harry L. Swinney. Collective motion and density fluctuations in bacterial colonies. *Proceedings of the National Academy of Sciences of the United States of America*, 107(31):13626–13630, 2010.
- [95] Julien Deseigne, Olivier Dauchot, and Hugues Chaté. Collective motion of vibrated polar disks. *Physical Review Letters*, 105:098001, 2010.
- [96] Volker Schaller and Andreas R. Bausch. Topological defects and density fluctuations in collectively moving systems. *Proceedings of the National Academy of Sciences of the United States of America*, 110(12):4488–4493, 2013.
- [97] Kyogo Kawaguchi, Ryoichiro Kageyama, and Masaki Sano. Topological defects control collective dynamics in neural progenitor cell cultures. *Nature*, 545(7654):327–331, 2017.
- [98] Long-range nematic order and anomalous fluctuations in suspensions of swimming filamentous bacteria. *Physical Review E*, 95(2):020601, 2017.
- [99] Hamid Karani, Gerardo E. Pradillo, and Petia M. Vlahovska. Tuning the Random Walk of Active Colloids: From Individual Run-And-Tumble to Dynamic Clustering. *Physical Review Letters*, 123:208002, 2019.
- [100] Arshad Kudrolli, Geoffroy Lumay, Dmitri Volfson, and Lev S. Tsimring. Swarming and swirling in self-propelled polar granular rods. *Physical Review Letters*, 100:058001, 2008.

- [101] Vasil Bratanov, Frank Jenko, and Erwin Frey. New class of turbulence in active fluids. *Proceedings of the National Academy of Sciences of the United States of America*, 112(49):15048–15053, 2015.
- [102] Luca Giomi. Geometry and topology of Turbulence in active nematics. *Physical Review X*, 5:031003, 2015.
- [103] Dóra Bárdfalvy, Henrik Nordanger, Cesare Nardini, Alexander Morozov, and Joakim Stenhammar. Particle-resolved lattice Boltzmann simulations of 3-dimensional active turbulence. *Soft Matter*, 15(39):7747–7756, 2019.
- [104] Moritz Linkmann, Guido Boffetta, M. Cristina Marchetti, and Bruno Eckhardt. Phase Transition to Large Scale Coherent Structures in Two-Dimensional Active Matter Turbulence. *Physical Review Letters*, 122:214503, 2019.
- [105] Rayan Chatterjee, Navdeep Rana, R. Aditi Simha, Prasad Perlekar, and Sriram Ramaswamy. Fluid flocks with inertia. *arXiv*, 2019, 1907.03492.
- [106] Viktor Škultéty, Cesare Nardini, Joakim Stenhammar, Davide Marenduzzo, and Alexander Morozov. Swimming Suppresses Correlations in Dilute Suspensions of Pusher Microorganisms. *Physical Review X*, 10:031059, 2020.
- [107] Oded Beja, L. Aravind, Eugene V. Koonin, Marcelino T. Suzuki, Andrew Hadd, Linh P. Nguyen, Stevan B. Jovanovich, Christian M. Gates, Robert A. Feldman, John L. Spudich, Elena N. Spudich, and Edward F. DeLong. Bacterial rhodopsin: Evidence for a new type of phototrophy in the sea. *Science*, 289(5486):1902–1906, 2000.
- [108] Sriram Subramaniam and Richard Henderson. Molecular mechanism of vectorial proton translocation by bacteriorhodopsin. *Nature*, 406(6796):653–657, 2000.

- [109] José R. De la Torre, Lynne M. Christianson, Oded Béjà, Marcelino T. Suzuki, David M. Karl, John Heidelberg, and Edward F. DeLong. Proteorhodopsin genes are distributed among divergent marine bacterial taxa. *Proceedings of the National Academy of Sciences of the United States of America*, 100(22):12830–12835, 2003.
- [110] Jessica M. Walter, Derek Greenfield, Carlos Bustamante, and Jan Liphardt. Light-powering Escherichia coli with proteorhodopsin. *Proceedings of the National Academy of Sciences of the United States of America*, 104(7):2408–2412, 2007.
- [111] Nico J. Claassens, Michael Volpers, Vitor A.P.Martins dos Santos, John Van der Oost, and Willem M. de Vos. Potential of proton-pumping rhodopsins: Engineering photosystems into microorganisms. *Trends in Biotechnology*, 31(11):633–642, 2013.
- [112] W. C.K. Poon. From Clarkia to escherichia and janus: The physics of natural and synthetic active colloids. *Proceedings of the International School of Physics "Enrico Fermi"*, 184:317–386, 2012.
- [113] Jana Schwarz-Linek, Jochen Arlt, Alya Jepson, Angela Dawson, Teun Vissers, Dario Miroli, Teuta Pilizota, Vincent A. Martinez, and Wilson C.K. Poon. Escherichia coli as a model active colloid: A practical introduction. *Colloids and Surfaces B: Biointerfaces*, 137:2–16, 2016.
- [114] Eric Lauga. Bacterial Hydrodynamics. *Annual Review of Fluid Mechanics*, 48:105–130, 2016.
- [115] J. Elgeti, R. G. Winkler, and G. Gompper. Physics of microswimmers - Single particle motion and collective behavior: A review. *Reports on Progress in Physics*, 78(5):056601, 2015.

- [116] Takuji Ishikawa and T. J. Pedley. The rheology of a semi-dilute suspension of swimming model micro-organisms. *Journal of Fluid Mechanics*, 588:399–435, 2007.
- [117] Knut Drescher, Jörn Dunkel, Luis H. Cisneros, Sujoy Ganguly, and Raymond E. Goldstein. Fluid dynamics and noise in bacterial cell-cell and cell-surface scattering. *Proceedings of the National Academy of Sciences of the United States of America*, 108(27):10940–10945, 2011.
- [118] Linda Turner, William S. Ryu, and Howard C. Berg. Real-time imaging of fluorescent flagellar filaments. *Journal of Bacteriology*, 182(10):2793–2801, 2000.
- [119] Nikon Instruments Inc. Nikon inverted microscope eclipse ti-e ti-e/b instructions:  
<http://squishycell.uchicago.edu/manuals/Ti-E%20manual.pdf>.
- [120] Yannis Kalaidzidis. Intracellular objects tracking. *European Journal of Cell Biology*, 86(9):569–578, 2007.
- [121] Erik Meijering, Ihor Smal, and Gaudenz Danuser. Tracking in molecular bioimaging. *IEEE Signal Processing Magazine*, 23(3):46–53, 2006.
- [122] Khuloud Jaqaman, Dinah Loerke, Marcel Mettlen, Hirotaka Kuwata, Sergio Grinstein, Sandra L. Schmid, and Gaudenz Danuser. Robust single-particle tracking in live-cell time-lapse sequences. *Nature Methods*, 5(8):695–702, 2008.
- [123] Karl Rohr, William J. Godinez, Nathalie Harder, Stefan Wörz, Julian Mattes, Wolfgang Tvaruskó, and Roland Eils. Tracking and quantitative analysis of dynamic movements of cells and particles. *Cold Spring Harbor Protocols*, 5(6):1–17, 2010.

- [124] Jonas F. Dorn, Gaudenz Danuser, and Ge Yang. Computational Processing and Analysis of Dynamic Fluorescence Image Data. *Methods in Cell Biology*, 85(08):497–538, 2008.
- [125] Erik Meijering, Oleh Dzyubachyk, Ihor Smal, and Wiggert A. van Cappellen. Tracking in cell and developmental biology. *Seminars in Cell and Developmental Biology*, 20(8):894–902, 2009.
- [126] Ihor Smal, Marco Loog, Wiro Niessen, and Erik Meijering. Quantitative comparison of spot detection methods in fluorescence microscopy. *IEEE Transactions on Medical Imaging*, 29(2):282–301, 2010.
- [127] Erik Meijering, Oleh Dzyubachyk, and Ihor Smal. *Methods for cell and particle tracking*, volume 504. Elsevier Inc., 1 edition, 2012.
- [128] Nicolas Chenouard, Ihor Smal, Fabrice De Chaumont, Martin Maška, Ivo F. Sbalzarini, Yuanhao Gong, Janick Cardinale, Craig Carthel, Stefano Coraluppi, Mark Winter, Andrew R. Cohen, William J. Godinez, Karl Rohr, Yannis Kalaidzidis, Liang Liang, James Duncan, Hongying Shen, Yingke Xu, Klas E.G. Magnusson, Joakim Jaldén, Helen M. Blau, Perrine Paul-Gilloteaux, Philippe Roudot, Charles Kervrann, François Waharte, Jean Yves Tinevez, Spencer L. Shorte, Joost Willemse, Katherine Celler, Gilles P. Van Wezel, Han Wei Dan, Yuh Show Tsai, Carlos Ortiz De Solórzano, Jean Christophe Olivo-Marin, and Erik Meijering. Objective comparison of particle tracking methods. *Nature Methods*, 11(3):281–289, 2014.
- [129] Martin Maška, Vladimír Ulman, David Svoboda, Pavel Matula, Petr Matula, Cristina Ederra, Ainhoa Urbiola, Tomás España, Subramanian Venkatesan, Deepak M.W. Balak, Pavel Karas, Tereza Bolcková, Markéta Štreitová, Craig

Carthel, Stefano Coraluppi, Nathalie Harder, Karl Rohr, Klas E.G. Magnusson, Joakim Jaldén, Helen M. Blau, Oleh Dzyubachyk, Pavel Křížek, Guy M. Hagen, David Pastor-Escuredo, Daniel Jimenez-Carretero, Maria J. Ledesma-Carbayo, Arrate Muñoz-Barrutia, Erik Meijering, Michal Kozubek, and Carlos Ortiz-De-Solorzano. A benchmark for comparison of cell tracking algorithms. *Bioinformatics*, 30(11):1609–1617, 2014.

- [130] Oliver Hilsenbeck, Michael Schwarzfischer, Stavroula Skylaki, Bernhard Schauberger, Philipp S. Hoppe, Dirk Loeffler, Konstantinos D. Kokkaliaris, Simon Hastreiter, Eleni Skylaki, Adam Filipczyk, Michael Strasser, Felix Buggenthin, Justin S. Feigelman, Jan Krumsiek, Adrianus J.J. Van Den Berg, Max Endele, Martin Etzrodt, Carsten Marr, Fabian J. Theis, and Timm Schroeder. Software tools for single-cell tracking and quantification of cellular and molecular properties. *Nature Biotechnology*, 34(7):703–706, 2016.
- [131] F. Boulogne. Custom feature detection and velocity fields: Bubble tracking in 2d foams: <http://soft-matter.github.io/trackpy/v0.4.2/tutorial/custom-feature-detection.html>.
- [132] A. Sauret, F. Boulogne, J. Cappello, E. Dressaire, and H. A. Stone. Damping of liquid sloshing by foams. *Physics of Fluids*, 27(2):022103, 2015.
- [133] J. Cappello, A. Sauret, F. Boulogne, E. Dressaire, and H. A. Stone. Damping of liquid sloshing by foams: from everyday observations to liquid transport. *Journal of Visualization*, 18(2):269–271, 2015.
- [134] Z. J. Taylor, R. Gurka, G. A. Kopp, and A. Liberzon. Openpiv official website: <http://www.openpiv.net/>.

- [135] Z. J. Taylor, R. Gurka, G. A. Kopp, and A. Liberzon. Long-duration time-resolved piv to study unsteady aerodynamics. *IEEE Transactions on Instrumentation and Measurement*, 59(12):3262–3269, 2010.
- [136] Dong Qin, Younan Xia, and George M. Whitesides. Soft lithography for micro- and nanoscale patterning. *Nature Protocols*, 5(3):491–502, 2010.
- [137] Hanjing Yang, Hachiro Inokuchi, and Julius Adler. Phototaxis away from blue light by an Escherichia coli mutant accumulating protoporphyrin IX. *Proceedings of the National Academy of Sciences of the United States of America*, 92(16):7332–7336, 1995.
- [138] Kirill A. Datsenko and Barry L. Wanner. One-step inactivation of chromosomal genes in Escherichia coli K-12 using PCR products. *Proceedings of the National Academy of Sciences of the United States of America*, 97(12):6640–6645, 2000.
- [139] Jérémie Palacci, Cécile Cottin-Bizonne, Christophe Ybert, and Lydéric Bocquet. Sedimentation and effective temperature of active colloidal suspensions. *Physical Review Letters*, 105:088304, 2010.
- [140] Luis H. Cisneros, John O. Kessler, Sujoy Ganguly, and Raymond E. Goldstein. Dynamics of swimming bacteria: Transition to directional order at high concentration. *Physical Review E*, 83:061907, 2011.
- [141] Shuo Guo, Devranjan Samanta, Yi Peng, Xinliang Xu, and Xiang Cheng. Symmetric shear banding and swarming vortices in bacterial superfluids. *Proceedings of the National Academy of Sciences of the United States of America*, 115(28):7212–7217, 2018.

- [142] Brian M. Haines, Andrey Sokolov, Igor S. Aranson, Leonid Berlyand, and Dmitry A. Karpeev. Three-dimensional model for the effective viscosity of bacterial suspensions. *Physical Review E*, 80:041922, 2009.
- [143] D. Saintillan. The Dilute Rheology of Swimming Suspensions: A Simple Kinetic Model. *Experimental Mechanics*, 50(9):1275–1281, 2010.
- [144] Shawn D. Ryan, Brian M. Haines, Leonid Berlyand, Falko Ziebert, and Igor S. Aranson. Viscosity of bacterial suspensions: Hydrodynamic interactions and self-induced noise. *Physical Review E*, 83:050904, 2011.
- [145] Moslem Moradi and Ali Najafi. Rheological properties of a dilute suspension of self-propelled particles. *Europhysics Letters*, 109(2):24001, 2015.
- [146] Toni M. Bechtel and Aditya S. Khair. Linear viscoelasticity of a dilute active suspension. *Rheologica Acta*, 56(2):149–160, 2017.
- [147] S. C. Takatori, W. Yan, and J. F. Brady. Swim pressure: Stress generation in active matter. *Physical Review Letters*, 113:028103, 2014.
- [148] Sho C. Takatori and John F. Brady. Swim stress, motion, and deformation of active matter: Effect of an external field. *Soft Matter*, 10(47):9433–9445, 2014.
- [149] Hugo Wioland, Francis G. Woodhouse, Jörn Dunkel, and Raymond E. Goldstein. Ferromagnetic and antiferromagnetic order in bacterial vortex lattices. *Nature Physics*, 12(4):341–345, 2016.
- [150] Wilhelm Foissner. An updated compilation of world soil ciliates (Protozoa, Ciliophora), with ecological notes, new records, and descriptions of new species. *European Journal of Protistology*, 34(2):195–235, 1998.

- [151] D. Or, B. F. Smets, J. M. Wraith, A. Dechesne, and S. P. Friedman. Physical constraints affecting bacterial habitats and activity in unsaturated porous media - a review. *Advances in Water Resources*, 30(6-7):1505–1527, 2007.
- [152] Howard C. Berg. *E. coli in Motion*. 2004.
- [153] J. S. Parkinson. Complementation analysis and deletion mapping of Escherichia coli mutants defective in chemotaxis. *Journal of Bacteriology*, 135(1):45–53, 1978.
- [154] H. Lamb. *Hydrodynamics*. The University Press, 1932.
- [155] Pierre Guillot, Pascal Panizza, Jean Baptiste Salmon, Mathieu Joanicot, Annie Colin, Charles Henri Bruneau, and Thierry Colin. Viscosimeter on a microfluidic chip. *Langmuir*, 22(14):6438–6445, 2006.
- [156] Philippe Nghe, Patrick Tabeling, and Armand Ajdari. Flow-induced polymer degradation probed by a high throughput microfluidic set-up. *Journal of Non-Newtonian Fluid Mechanics*, 165(7-8):313–322, 2010.
- [157] E. J. Hinch, O. J. Harris, and J. M. Rallison. The instability mechanism for two elastic liquids being co-extruded. *Journal of Non-Newtonian Fluid Mechanics*, 43(2-3):311–324, 1992.
- [158] John F. Brady and Ileana C. Carpen. Second normal stress jump instability in non-Newtonian fluids. *Journal of Non-Newtonian Fluid Mechanics*, 102(2):219–232, 2002.
- [159] Ronald G. Egres, Florian Nettesheim, and Norman J. Wagner. Rheo-SANS investigation of acicular-precipitated calcium carbonate colloidal suspensions through the shear thickening transition. *Journal of Rheology*, 50(5):685–709, 2006.

- [160] Marcos, Henry C. Fu, Thomas R. Powers, and Roman Stocker. Bacterial rheotaxis. *Proceedings of the National Academy of Sciences of the United States of America*, 109(13):4780–4785, 2012.
- [161] Roberto Rusconi, Jeffrey S. Guasto, and Roman Stocker. Bacterial transport suppressed by fluid shear. *Nature Physics*, 10(3):212–217, 2014.
- [162] Jane Hill, Ozge Kalkanci, Jonathan L. McMurry, and Hur Koser. Hydrodynamic surface interactions enable escherichia coli to seek efficient routes to swim upstream. *Physical Review Letters*, 98:068101, 2007.
- [163] R. W. Nash, R. Adhikari, J. Tailleur, and M. E. Cates. Run-and-tumble particles with hydrodynamics: Sedimentation, trapping, and upstream swimming. *Physical Review Letters*, 104:258101, 2010.
- [164] A. Costanzo, R. Di Leonardo, G. Ruocco, and L. Angelani. Transport of self-propelling bacteria in micro-channel flow. *Journal of Physics Condensed Matter*, 24(6):065101, 2012.
- [165] Tolga Kaya and Hur Koser. Direct upstream motility in Escherichia coli. *Bio-physical Journal*, 102(7):1514–1523, 2012.
- [166] Sandeep Chilukuri, Cynthia H. Collins, and Patrick T. Underhill. Impact of external flow on the dynamics of swimming microorganisms near surfaces. *Journal of Physics Condensed Matter*, 26(11):115101, 2014.
- [167] Barath Ezhilan and David Saintillan. Transport of a dilute active suspension in pressure-driven channel flow. *Journal of Fluid Mechanics*, 777:482–522, 2015.

- [168] Allison P. Berke, Linda Turner, Howard C. Berg, and Eric Lauga. Hydrodynamic attraction of swimming microorganisms by surfaces. *Physical Review Letters*, 101:038102, 2008.
- [169] Guanglai Li and Jay X. Tang. Accumulation of microswimmers near a surface mediated by collision and rotational Brownian motion. *Physical Review Letters*, 103:078101, 2009.
- [170] J. R. Blake. A note on the image system for a stokeslet in a no-slip boundary. *Mathematical Proceedings of the Cambridge Philosophical Society*, 70(2):303–310, 1971.
- [171] A. J.T.M. Mathijssen, A. Doostmohammadi, J. M. Yeomans, and T. N. Shendruk. Hydrodynamics of micro-swimmers in films. *Journal of Fluid Mechanics*, 806:35–70, 2016.
- [172] Charles W. Wolgemuth. Collective swimming and the dynamics of bacterial turbulence. *Biophysical Journal*, 95(4):1564–1574, 2008.
- [173] Joakim Stenhammar, Cesare Nardini, Rupert W. Nash, Davide Marenduzzo, and Alexander Morozov. Role of Correlations in the Collective Behavior of Microswimmer Suspensions. *Physical Review Letters*, 119:028005, 2017.
- [174] Christel Hohenegger and Michael J. Shelley. Stability of active suspensions. *Physical Review E*, 81:046311, 2010.
- [175] Ganesh Subramanian and Donald L. Koch. Critical bacterial concentration for the onset of collective swimming. *Journal of Fluid Mechanics*, 632:359–400, 2009.

- [176] Igor S. Aranson, Andrey Sokolov, John O. Kessler, and Raymond E. Goldstein. Model for dynamical coherence in thin films of self-propelled microorganisms. *Physical Review E*, 75:040901, 2007.
- [177] Barath Ezhilan, Michael J. Shelley, and David Saintillan. Instabilities and nonlinear dynamics of concentrated active suspensions. *Physics of Fluids*, 25(7):070607, 2013.
- [178] Nicholas Sambelashvili, A. W.C. Lau, and David Cai. Dynamics of bacterial flow: Emergence of spatiotemporal coherent structures. *Physics Letters, Section A: General, Atomic and Solid State Physics*, 360(4-5):507–511, 2007.
- [179] Aparna Baskaran and Cristina M. Marchetti. Nonequilibrium statistical mechanics of self-propelled hard rods. *Journal of Statistical Mechanics: Theory and Experiment*, 2010(4):P04019, 2010.
- [180] Takuji Ishikawa and Masateru Hota. Interaction of two swimming Paramecia. *Journal of Experimental Biology*, 209(22):4452–4463, 2006.
- [181] Nicholas C. Darnton, Linda Turner, Svetlana Rojevsky, and Howard C. Berg. Dynamics of bacterial swarming. *Biophysical Journal*, 98(10):2082–2090, 2010.
- [182] Luis H. Cisneros, Ricardo Cortez, Christopher Dombrowski, Raymond E. Goldstein, and John O. Kessler. Fluid dynamics of self-propelled microorganisms, from individuals to concentrated populations. *Experiments in Fluids*, 43(5):737–753, 2007.
- [183] Shawn D. Ryan, Andrey Sokolov, Leonid Berlyand, and Igor S. Aranson. Correlation properties of collective motion in bacterial suspensions. *New Journal of Physics*, 15:105021, 2013.

- [184] He Li, Xia qing Shi, Mingji Huang, Xiao Chen, Minfeng Xiao, Chenli Liu, Hugues Chaté, and H. P. Zhang. Data-driven quantitative modeling of bacterial active nematics. *Proceedings of the National Academy of Sciences of the United States of America*, 116(3):777–785, 2019.
- [185] Yi Peng, Feng Wang, Ziren Wang, Ahmed M. Alsayed, Zexin Zhang, Arjun G. Yodh, and Yilong Han. Two-step nucleation mechanism in solid-solid phase transitions. *Nature Materials*, 14(1):101–108, 2015.
- [186] F Scarano. Iterative image deformation methods in PIV. *Measurement Science and Technology*, 13(1):R1–R19, 2001.
- [187] Shuguang Li, Richa Batra, David Brown, Hyun Dong Chang, Nikhil Ranganathan, Chuck Hoberman, Daniela Rus, and Hod Lipson. Particle robotics based on statistical mechanics of loosely coupled components. *Nature*, 567(7748):361–365, 2019.
- [188] Dóra Bárdfalvy, Shan Anjum, Cesare Nardini, Alexander Morozov, and Joakim Stenhammar. Symmetric Mixtures of Pusher and Puller Microswimmers Behave as Noninteracting Suspensions. *Physical Review Letters*, 125:018003, 2020.
- [189] Deepak Krishnamurthy and Ganesh Subramanian. Collective motion in a suspension of micro-swimmers that run-and-tumble and rotary diffuse. *Journal of Fluid Mechanics*, 781:422–466, 2015.
- [190] Nitin Kumar, Harsh Soni, Sriram Ramaswamy, and A. K. Sood. Flocking at a distance in active granular matter. *Nature Communications*, 5:4688, 2014.
- [191] Vincent A. Martinez, Eric Clément, Jochen Arlt, Carine Douarche, Angela Dawson, Jana Schwarz-Linek, Adama K. Creppy, Viktor Škultéty, Alexander N. Morozov, Harold Auradou, and Wilson C.K. Poon. A combined rheometry and imaging

- study of viscosity reduction in bacterial suspensions. *Proceedings of the National Academy of Sciences of the United States of America*, 117(5):2326–2331, 2020.
- [192] S. C. Takatori and J. F. Brady. Towards a thermodynamics of active matter. *Physical Review E*, 91:032117, 2015.
- [193] Berta Martínez-Prat, Jordi Ignés-Mullol, Jaume Casademunt, and Francesc Sagués. Selection mechanism at the onset of active turbulence. *Nature Physics*, 15(4):362–366, 2019.
- [194] M E Cates. Diffusive transport without detailed balance in motile bacteria: does microbiology need statistical physics? *Reports on Progress in Physics*, 75(4):42601, 2012.
- [195] W. C. K. Poon. From Clarkia to escherichia and janus: The physics of natural and synthetic active colloids. *Proceedings of the International School of Physics "Enrico Fermi"*, 184:317–386, 2013.
- [196] Y Mishin. Thermodynamic theory of equilibrium fluctuations. *Annals of Physics*, 363:48–97, 2015.
- [197] Shradha Mishra, Aparna Baskaran, and M. Cristina Marchetti. Fluctuations and pattern formation in self-propelled particles. *Physical Review E*, 81:061916, 2010.
- [198] Ricard Alert, Jean François Joanny, and Jaume Casademunt. Universal scaling of active nematic turbulence. *Nature Physics*, 16(6):682–688, 2020.
- [199] Adama Creppy, Olivier Praud, Xavier Druart, Philippa L. Kohnke, and Franck Plouraboué. Turbulence of swarming sperm. *Physical Review E*, 92:032722, 2015.

- [200] Alison E. Patteson, Arvind Gopinath, and Paulo E. Arratia. The propagation of active-passive interfaces in bacterial swarms. *Nature Communications*, 9(1):5373, 2018.
- [201] L. G. Wilson, V. A. Martinez, J. Schwarz-Linek, J. Tailleur, G. Bryant, P. N. Pusey, and W. C.K. Poon. Differential dynamic microscopy of bacterial motility. *Physical Review Letters*, 106:018101, 2011.
- [202] Yukio Magariyama and Seishi Kudo. A mathematical explanation of an increase in bacterial swimming speed with viscosity in linear-polymer solutions. *Biophys. J.*, 83(2):733 – 739, 2002.
- [203] Daniel G. Gibson, Lei Young, Ray Yuan Chuang, J. Craig Venter, Clyde A. Hutchison, and Hamilton O. Smith. Enzymatic assembly of DNA molecules up to several hundred kilobases. *Nature Methods*, 6(5):343–345, 2009.
- [204] Zymo Research. Plasmid miniprep kit manual: [https://files.zymoresearch.com/protocols/\\_d4019\\_d4020\\_d4036\\_d4037\\_zyppy\\_plasmid\\_miniprep\\_kit.pdf](https://files.zymoresearch.com/protocols/_d4019_d4020_d4036_d4037_zyppy_plasmid_miniprep_kit.pdf).
- [205] Zymo Research. Gel dna recovery kit manual: [https://files.zymoresearch.com/protocols/\\_d4001t\\_d4001\\_d4002\\_d4007\\_d4008\\_zymoclean\\_gel\\_dna\\_recovery\\_kit.pdf](https://files.zymoresearch.com/protocols/_d4001t_d4001_d4002_d4007_d4008_zymoclean_gel_dna_recovery_kit.pdf).

# Appendix A

## Light-controlled *Escherichia coli*

### A.1 Plasmid Construction and Transformation

#### A.1.1 Plasmid Construction

Here I present the plasmid construction protocol using Gibson assembly. This method can ligate the target gene PR with the plasmid carrier pZE. We first use polymerase chain reaction (PCR) to amplify the gene to sufficient concentration for the ligation. PCR can be easily done with a standard thermo cycler, and all we need to do is to prepare a mixture according to the recipe shown in Table. A.1

The sequence of the primers can be found in Table. 2.2, and are synthesized by Eurofins Scientific. After we obtain the more concentrated DNA from PCR, we use Gibson assembly [203] to ligate the plasmid carrier pZE and the target DNA sequence PR. Gibson assembly is done in the following steps:

- prepare the Gibson assembly mix accoring to the Table. A.2.
- add the mix into a  $200 \mu\text{l}$  centrifuge tube, then put the tube into a thermal cycler and run the Gibson assembly program ( $50\text{--}55^\circ\text{C}$  for 1 hour).

Ingredients	Amount ( $\mu$ l)
ddH <sub>2</sub> O	37
5X HF buffer (Phusion)	10
dNTP	1
Primer-forward	0.5
Primer-reverse	0.5
Template	small amount of cell culture / 0.5 $\mu$ l plasmid solution
Phusion polymerase	0.5
Sum	50

Table A.1: PCR recipe using Phusion polymerase

- thaw the chemical competent cells in ice (XL10-Gold, 3-4 min).
- mix cells and plasmid solution for 10 min in ice.
- spread the mix on a selective plate.

Ingredients	Amount ( $\mu$ l)
PCR product	3.3
pZE solution	1.7
2X Gibson assembly mix	5
Sum	10

Table A.2: Gibson assembly recipe.

### A.1.2 Extraction and Purification

After growing the chemical competent cells into concentrated liquid cultures, we extract the plasmid from the cells and purify them. We follow the steps in the Zippy Plasmid Miniprep Kit manual [204] and Zymoclean Gel DNA Recovery Kit manual [205].

### A.1.3 Transformation

#### Make electrocompetent cells

- Inoculate target cells (*E. coli*, 1 ml) into a test tube and incubate at 37 °C for 16-18 hours.
- Prepare a box of ice and put 10% glycerol on it.
- Place the cell culture on ice for 15 minutes (Note: from this step, the cell culture must be on ice all the time).
- Centrifuge at 4000 rpm for 5 min, at 4 °C (use the low temperature centrifuge)
- Discard the supernatant, aspirate the residual broth and add 1 ml glycerol. Resuspend the cells by pipetting up and down.
- Repeat step 4 and 5 for 2 more times (Note: for the last time, add ~ 50  $\mu$ l glycerol instead of 1 ml).

#### Electroporation

- Thaw the cell suspensions prepared in the previous step on ice. Place a 1.5 ml centrifuge tube and a 0.1 cm cuvette on ice.
- Add 40  $\mu$ l cell suspension and 1  $\mu$ l DNA solution to the 1.5 ml centrifuge tube.
- Set the electroporator mode to Ec1.
- Transfer the mixture of cells and DNA to the cuvette and tap it to make the cell suspension go to the bottom of the cuvette.
- Put the cuvette into the electroporator, and press the pulse button once.

- Remove the cuvette from the electroporator and spread the cell suspension on a selective plate.

## A.2 DNA Sequences

### A.2.1 Proteorhodopsin (PR) Sequence

```

1 ATGAAGTTGT TGTTGATCTT GGGATCTGTG ATTGCACTTC CGACGTTCGC TGCCGGCGGC
61 GGGGATTGAG ACACATCAGA CTACACAGGG GTTCGTTTT GGCTGGTCAC AGCCGCGCTG
121 TTAGCGTCCA CCGTCTTTT TTTCGTTGAA CGGGATAGAG TCTCAGCTAA GTGGAAGACA
181 TCGTTGACCG TCTCAGGCTT GGTTACCGGC ATTGCCTTCT GGCATTATAT GTACATGCGT
241 GGTGTCTGGA TTGAAACGGG TGACAGCCCG ACGGTGTTCC GTTATATCGA CTGGCTTTA
301 ACCGTTCCCC TTCTGATTTG TGAGTTTAT TTAATATTGG CGGCAGCAAC GAATGTGGCC
361 GGTCACTGT TCAAGAACGCT TCTTGAGGA AGTTTAGTTA TGTTGGTTTT CGGCTACATG
421 GGAGAGGCAG GGATAATGGC GGCCTGGCCG GCGTTCATAA TTGGTTGCTT GGCTTGGGTG
481 TACATGATCT ACGAGCTGTG GGCAGGAGAA GGCAAGTCTG CGTGCAACAC AGCATGCCA
541 GCAGTTCAAT CCGCATATAA TACGATGATG TATATAATTA TCTTGGTTG GGCAATTAC
601 CCGGTCGGAT ACTTCACCGG CTATCTTATG GGCGACGGGG GCTCTGCCTT GAACTTGAAT
661 CTTATATATA ACCTGGCCGA TTTCGTGAAC AAGATTTGT TTGGACTTAT AATATGGAAC
721 GTAGCCGTGA AAGAGTCATC GAACGCATAA

```

### A.2.2 pZE-PR Plasmid Sequence

```

1 AGGCGTATCA CGAGGCCCTT TCGTCTTCAC CTCGAGAATT GTGAGCGGAT AACAAATTGAC
61 ATTGTGAGCG GATAACAAGA TACTGAGCAC ATCAGCAGGA CGCACTGACC GAATTCTATTA
121 AAGAGGAGAA AGGTACCATG AAGTTGTTGT TGATCTTGGG ATCTGTGATT GCACTTCCGA
181 CGTTCGCTGC CGGCAGCGGG GATTTGGACG CATCAGACTA CACAGGGGTT TCGTTGGC
241 TGGTCACAGC CGCGCTGTTA GCGTCCACCG TCTTTTTTT CGTTGAACGG GATAGAGTCT

```

301 CAGCTAAGTG GAAGACATCG TTGACCGTCT CAGGCTTGGT TACCGCATT GCCTTCTGGC  
361 ATTATATGTA CATCGTGGT GTCTGGATTG AAACGGGTGA CAGCCGACG GTGTTCCGTT  
421 ATATCGACTG GCTTTAACCG TTCCCCCTTC TGATTTGTGA GTTTTATTAA ATATTGGCGG  
481 CAGCAACGAA TGTGGCCGGT TCACTGTTCA AGAAGCTTCT TGTAGGAAGT TTAGTTATGT  
541 TGGTTTCGG CTACATGGGA GAGGCAGGGA TAATGGCGGC CTGGCCGGCG TTCATAATTG  
601 GTTGCTTGGC TTGGGTGTAC ATGATCTACG AGCTGTGGGC AGGAGAAGGC AAGTCTGCGT  
661 GCAACACAGC ATGCCAGCA GTTCAATCCG CATATAATAC GATGATGTAT ATAATTATCT  
721 TTGGTTGGC AATTTACCCG GTCGGATACT TCACCGGCTA TCTTATGGC GACGGGGGCT  
781 CTGCCTTGAA CTTGAATCTT ATATATAACC TGGCCGATT CGTGAACAAG ATTTGTTTG  
841 GACTTATAAT ATGGAACGTA GCCGTGAAAG AGTCATCGAA CGCATAATCT AGAGGCATCA  
901 AATAAAACGA AAGGCTCAGT CGAAAGACTG GGCCTTCGT TTTATCTGTT GTTGTCGGT  
961 GAACGCTCTC CTGAGTAGGA CAAATCCGCC GCCCTAGACC TAGGCCTCG GCTGCGGCGA  
1021 GCGGTATCAG CTCACTAAA GGCGGTAAATA CGGTTATCCA CAGAACAGG GGATAACGCA  
1081 GGAAAGAACAA TGTGAGCAAAG AGGCCAGCAA AAGGCCAGGA ACCGTAAAAA GGCCGCGTTG  
1141 CTGGCGTTT TCCATAGGCT CCGCCCCCT GACGAGCATC ACAAAATCG ACGCTCAAGT  
1201 CAGAGGTGGC GAAACCCGAC AGGACTATAA AGATACCAGG CGTTTCCCCC TGGAAGCTCC  
1261 CTCGTGCGCT CTCCTGTTCC GACCCTGCCG CTTACCGGAT ACCTGTCCGC CTTTCTCCCT  
1321 TCGGGAAGCG TGGCGTTTC TCAATGCTCA CGCTGTAGGT ATCTCAGTTC GGTGTAGGTC  
1381 GTTCGCTCCA AGCTGGCTG TGTGCACGAA CCCCCCGTTC AGCCCGACCG CTGCGCCTTA  
1441 TCCGGTAACATCGTCTTGA GTCCAACCCG GTAAGACACG ACTTATCGCC ACTGGCAGCA  
1501 GCCACTGGTA ACAGGATTAG CAGAGCGAGG TATGTAGGCG GTGCTACAGA GTTCTTGAAG  
1561 TGGTGGCCTA ACTACGGCTA CACTAGAAGG ACAGTATTTG GTATCTGCGC TCTGCTGAAG  
1621 CCAGTTACCT TCGGAAAAAG AGTTGGTAGC TCTTGATCCG GCAAACAAAC CACCGCTGGT  
1681 AGCGGTGGTT TTTTGTTTG CAAGCAGCAG ATTACGCGCA GAAAAAAAGG ATCTCAAGAA  
1741 GATCCTTGA TCTTTCTAC GGGGTCTGAC GCTCAGTGGA ACGAAAACTC ACGTTAAGGG  
1801 ATTTGGTCA TGACTAGTGC TTGGATTCTC ACCAATAAAA AACGCCGGC GGCAACCGAG

1861 CGTTCTGAAC AAATCCAGAT GGAGTTCTGA GGTCAATTACT GGATCTATCA ACAGGAGTCC  
1921 AAGCGAGCTC TCACTGCCCG CTTTCAGTC GGGAAACCTG TCGTGCCAGC TGCATTAATG  
1981 AATCGGCCAA CGCGCGGGGA GAGGCGGTTT GCGTATTGGG CGCCAGGGTG GTTTTCTTT  
2041 TCACCAGTGA GACGGGCAAC AGCTGATTGC CCTTCACCAGC CTGGCCCTGA GAGAGTTGCA  
2101 GCAAGCGGTC CACGCTGGTT TGCCCCAGCA GGCGAAAATC CTGTTGATG GTGGTTAACG  
2161 GCGGGATATA ACATGAGCTG TCTTCGGTAT CGTCGTATCC CACTACCGAG ATATCCGCAC  
2221 CAACCGCGCAG CCCGGACTCG GTAATGGCGC GCATTGCGCC CAGGCCATC TGATCGTTGG  
2281 CAACCAGCAT CGCAGTGGGA ACGATGCCCT CATTCAAGCAT TTGCATGGTT TGTTGAAAAC  
2341 CGGACATGGC ACTCCAGTCG CCTTCCCAGTT CCGCTATCGG CTGAATTGAA TTGCGAGTGA  
2401 GATATTATG CCAGCCAGCC AGACGCAGAC GCGCCGAGAC AGAACTTAAT GGGCCCGCTA  
2461 ACAGCGCGAT TTGCTGGTGA CCCAATGCGA CCAGATGCTC CACGCCAGT CGCGTACCGT  
2521 CTTCATGGGA GAAAATAATA CTGTTGATGG GTGTCTGGTC AGAGACATCA AGAAATAACG  
2581 CCGGAACATT AGTGCAGGCA GCTTCCACAG CAATGGCATC CTGGTCATCC AGCGGATAGT  
2641 TAATGATCAG CCCACTGACG CGTTGCGCGA GAAGATTGTG CACCGCCGCT TTACAGGCTT  
2701 CGACGCCGCT TCGTTCTACC ATCGACACCA CCACGCTGGC ACCCAGTTGA TCGGCGCGAG  
2761 ATTTAATCGC CGCGACAATT TGCGACGGCG CGTGCAGGGC CAGACTGGAG GTGGCAACGC  
2821 CAATCAGCAA CGACTGTTTCCC CGCCAGTT GTTGTGCCAC GCGGTTGGGA ATGTAATTCA  
2881 GCTCCGCCAT CGCCGCTTCC ACTTTTCCC GCGTTTCCG AGAAACGTGG CTGGCCTGGT  
2941 TCACCACGCG GGAAACGGTC TGATAAGAGA CACCGGCATA CTCTGCGACA TCGTATAACG  
3001 TTACTGGTTT CATGGTATAT CTCCTTCGAG CTCGTAAACT TGGTCTGACA GTTACCAATG  
3061 CTTAACAGT GAGGCACCTA TCTCAGCGAT CTGTCTATTG CGTTCATCCA TAGTTGCCTG  
3121 ACTCCCCGTC GTGTAGATAA CTACGATACG GGAGGGCTTA CCATCTGGCC CCAGTGCTGC  
3181 AATGATACCG CGAGACCCAC GCTCACCGGC TCCAGATTAA TCAGCAATAA ACCAGCCAGC  
3241 CGGAAGGGCC GAGCGCAGAA GTGGTCTGC AACTTTATCC GCCTCCATCC AGTCTATTAA  
3301 TTGTTGCCGG GAAGCTAGAG TAAGTAGTTC GCCAGTTAAT AGTTGCGCA ACGTTGTTGC  
3361 CATTGCTACA GGCATCGTGG TGTCAAGCTC GTCGTTGGT ATGGCTTCAT TCAGCTCCGG

3421 TTCCCAACGA TCAAGGCGAG TTACATGATC CCCCATGTTG TGCAAAAAAG CGGTTAGCTC  
 3481 CTTCGGTCCT CCGATCGTTG TCAGAAGTAA GTTGGCCGCA GTGTTATCAC TCATGGTTAT  
 3541 GGCAGCACTG CATAATTCTC TTACTGTCAT GCCATCCGTA AGATGCTTT CTGTGACTGG  
 3601 TGAGTACTCA ACCAAGTCAT TCTGAGAATA GTGTATGCGG CGACCGAGTT GCTCTTGCCC  
 3661 GGCGTCAATA CGGGATAATA CCGGCCACA TAGCAGAACT TTAAAAGTGC TCATCATTGG  
 3721 AAAACGTTCT TCAGGGCGAA AACTCTCAAG GATCTTACCG CTGTTGAGAT CCAGTTCGAT  
 3781 GTAACCCACT CGTGCACCCA ACTGATCTTC AGCATCTTT ACTTCACCA GCGTTCTGG  
 3841 GTGAGCAAAA ACAGGAAGGC AAAATGCCGC AAAAAAGGGA ATAAGGGCGA CACGGAAATG  
 3901 TTGAATACTC ATACTCTTCC TTTTCAATA TTATTGAAGC ATTTATCAGG GTTATTGTCT  
 3961 CATGAGCGGA TACATATTTG AATGTATTTA GAAAAATAAA CAAATAGGGG TTCCGCGCAC  
 4021 ATTTCCCCGA AAAGTGCCAC CTGACGTCTA AGAAACCATT ATTATCATGA CATTAACCTA  
 4081 TAAAAAT

### A.2.3 An Illustration of the pZE-PR Plasmid Structure

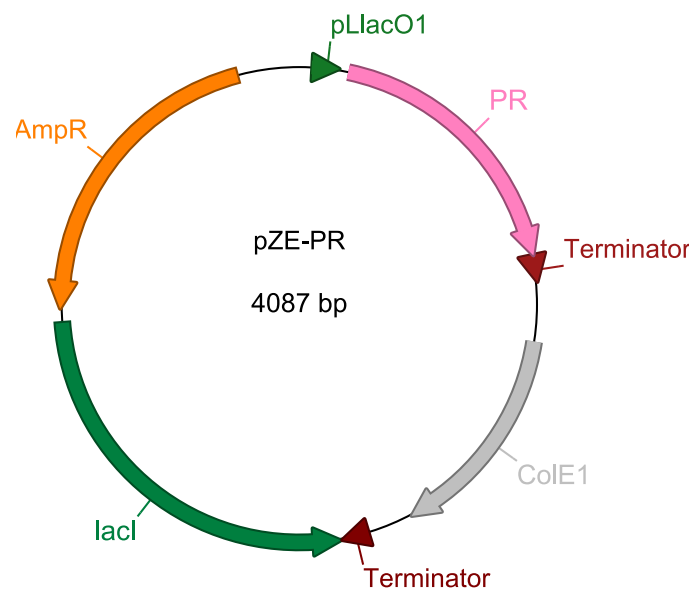


Figure A.1: An illustration of pZE-PR plasmid.

## Appendix B

# Image Analysis Code

## B.1 Code Vectorization

### B.1.1 Vectorized Code for Spatial Correlation Function

---

```
1 def corrS(X, Y, U, V):
2     row, col = X.shape
3     vsqrt = (U ** 2 + V ** 2) ** 0.5
4     U = U - U.mean()
5     V = V - V.mean()
6     Ax = U / vsqrt
7     Ay = V / vsqrt
8     CA = np.ones(X.shape)
9     CV = np.ones(X.shape)
10    for xin in range(0, col):
11        for yin in range(0, row):
12            if xin != 0 or yin != 0:
13                CA[yin, xin] = (Ax[0:row-yin, 0:col-xin] *
14                                  Ax[yin:row, xin:col] +
15                                  Ay[0:row-yin, 0:col-xin] *
16                                  Ay[yin:row, xin:col]).mean()
17                CV[yin, xin] = (U[0:row-yin, 0:col-xin] *
18                                  U[yin:row, xin:col] +
```

```

19          V[0:row-yin, 0:col-xin] *
20          V[yin:row, xin:col]).mean() /
21          (U.std()**2+V.std()**2)
22      return CA, CV

```

---

### B.1.2 Non-vectorized Code for Spatial Correlation Function

```

1 def corrS(X, Y, U, V):
2     row, col = X.shape
3     vsq = 0
4     CA = np.zeros((row, col))
5     CV = np.zeros((row, col))
6     for i in range(0, row):
7         for j in range(0, col):
8             vsq += U[i, j]**2 + V[i, j]**2
9     for xin in range(0, col):
10        for yin in range(0, row):
11            count = 0
12            CAt = 0
13            CVt = 0
14            for i in range(0, col-xin):
15                for j in range(0, row-yin):
16                    ua = U[j, i]
17                    va = V[j, i]
18                    ub = U[j+yin, i+xin]
19                    vb = V[j+yin, i+xin]
20                    CAt += (ua*ub+va*vb) / ((ua**2+va**2) *
21                                         (ub**2+vb**2))**.5
22                    CVt += ua*ub + va*vb
23                    count += 1
24            CA[yin, xin] = CAt / count
25            CV[yin, xin] = CVt / vsq
26    return CA, CV

```

---

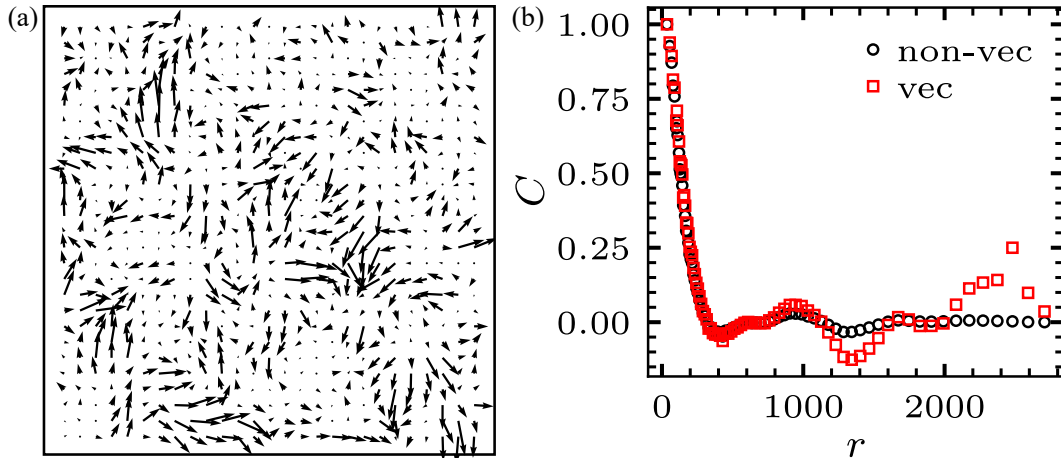


Figure B.1: **The performance of vectorized and non-vectorized code.** (a) Sample velocity field. (b) Velocity correlation functions obtained from the vectorized and non-vectorized code.

### B.1.3 Performance Comparison

We notice that the vectorized code has two less nested `for` loops compared to the non-vectorized code. As a result, the vectorized one runs much faster for the same task. To quantify this performance difference, we perform the spatial correlation function calculation using both codes on the same velocity field, shown in Fig. B.1a. The times taken for the two functions are:

- Vectorized code: 0.84 s
- Non-vectorized code: 52.06 s

The result is shown in Fig. B.1b. Although in the large  $r$  regime, two methods show discrepancies, in the meaningful small  $r$  regime, two methods give exactly the same results.

## B.2 Energy Spectrum Calculation

The following code is used for calculating the energy spectra in Chap. 5.

---

```

1  def compute_energy_density(pivData, d=25*0.33, MPP=0.33):
2      """
3          Compute kinetic energy density in k space from piv data.
4
5          Args:
6              pivData -- piv data
7              d -- sample spacing
8              MPP -- microns per pixel
9
10         Returns:
11             E -- kinetic energy field in k space
12         """
13
14     row = len(pivData.y.drop_duplicates())
15     col = len(pivData.x.drop_duplicates())
16     U = np.array(pivData.u).reshape((row, col)) * MPP
17     V = np.array(pivData.v).reshape((row, col)) * MPP
18
19     u_fft = np.fft.fft2(U) * d * d
20     v_fft = np.fft.fft2(V) * d * d
21
22     E = (u_fft * u_fft.conjugate() + v_fft * v_fft.conjugate()) / 2
23
24     return E
25
26 def compute_wavenumber_field(shape, d):
27     """
28         Compute the wave number field Kx and Ky, and magnitude field k.
29
30         Args:
31             shape -- shape of the velocity field and velocity fft field, tuple
32             d -- sample spacing.
33

```

```

34     Returns:
35     k -- wavenumber magnitude field
36     K -- wavenumber fields in given dimensions
37     """
38
39     for num, length in enumerate(shape):
40         kx = np.fft.fftfreq(length, d=d)
41         if num == 0:
42             k = (kx,)
43         else:
44             k += (kx,)
45
46     K = np.meshgrid(*k, indexing='ij')
47
48     for num, k1 in enumerate(K):
49         if num == 0:
50             ksq = k1 ** 2
51         else:
52             ksq += k1 ** 2
53
54     k_mag = ksq ** 0.5 * 2 * np.pi
55
56     return k_mag, K
57
58 def energy_spectrum(pivData, d=25*0.33):
59     """
60     Compute energy spectrum ( $E$  vs  $k$ ) from pivData.
61
62     Args:
63         pivData -- piv data
64         d -- sample spacing.
65
66     Returns:
67         es -- energy spectrum, DataFrame (k, E)
68         """
69
70     row = len(pivData.y.drop_duplicates())
71     col = len(pivData.x.drop_duplicates())

```

```

72
73     E = compute_energy_density(pivData, d) / (row * d * col * d)
74     k, K = compute_wavenumber_field(E.shape, d)
75
76     ind = np.argsort(k.flatten())
77     k_plot = k.flatten()[ind]
78     E_plot = E.real.flatten()[ind]
79
80     es = pd.DataFrame(data={'k': k_plot, 'E': E_plot})
81
82     return es

```

---

### B.3 Cross-Correlation Based Particle Detecting Method

This is designed for tracking colloidal chains. We show here the basic working principle and the code here. The advantage of this method is that it does not require the feature to be very bright or dark, like traditional particle detecting methods. As long as the features share similar characteristics, i.e. spatial patterns, this method can work well.

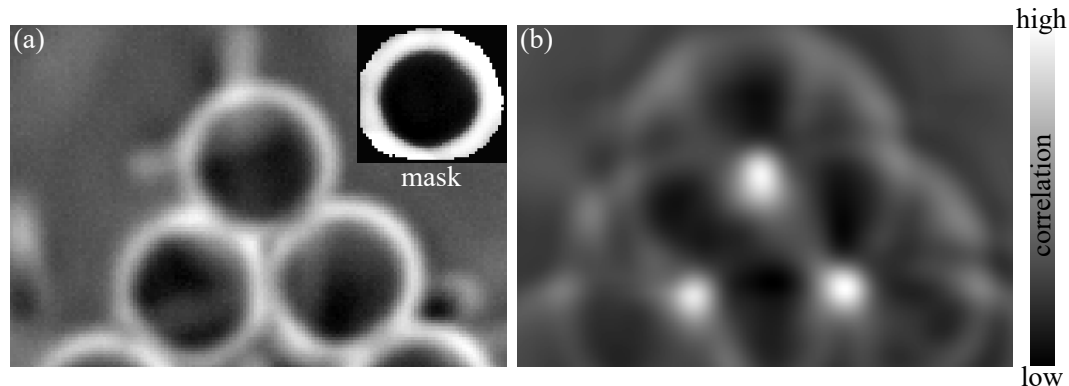


Figure B.2: **Cross-correlation based particle detecting method.** (a) A sample image of colloidal particles. Inset: a mask produced by cropping the raw image and binarize. (b) The cross-correlation map.

### B.3.1 Working Principle

From raw images, we crop out a single feature which we are looking for as a target mask, as shown in Fig. B.2a inset. Then, we do a 2D correlation between the target mask and an image (Fig. B.2a). The resulting correlation map is shown in Fig. B.2b, where bright pixels stand for high correlation and dark pixels stand for low correlation. The last step is to look for the pixel intensity peaks in the correlation map, as in traditional particle detecting methods.

### B.3.2 Code

---

```

1 import numpy as np
2 from scipy.signal import medfilt2d, convolve2d, fftconvolve
3 from math import exp
4
5 def normxcorr2(template, image, mode="full"):
6     if np.ndim(template) > np.ndim(image) or \
7         len([i for i in range(np.ndim(template))]) \
8             if template.shape[i] > image.shape[i]]) > 0:
9     template = template - np.mean(template)
10    image = image - np.mean(image)
11    a1 = np.ones(template.shape)
12    ar = np.fliplr(np.fliplr(template))
13    out = fftconvolve(image, ar.conj(), mode=mode)
14    image = fftconvolve(np.square(image), a1, mode=mode) - \
15        np.square(fftconvolve(image, a1, mode=mode)) \
16        / (np.prod(template.shape))
17    image[np.where(image < 0)] = 0
18    template = np.sum(np.square(template))
19    out = out / np.sqrt(image * template)
20    out[np.where(np.logical_not(np.isfinite(out)))] = 0
21    return -out
22
23 def matlab_style_gauss2D(shape=(3,3),sigma=0.5):
24     m,n = [(ss-1.)/2. for ss in shape]

```

```

25     y,x = np.ogrid[-m:m+1,-n:n+1]
26     h = np.exp( -(x*x + y*y) / (2.*sigma*sigma) )
27     h[ h < np.finfo(h.dtype).eps*h.max() ] = 0
28     sumh = h.sum()
29     if sumh != 0:
30         h /= sumh
31     return h
32
33 def FastPeakFind(data):
34     if str(data.dtype) != 'float32':
35         data = data.astype('float32')
36     mf = medfilt2d(data, kernel_size=3)
37     mf = mf.astype('float32')
38     thres = max(min(np.amax(mf, axis=0)), min(np.amax(mf, axis=1)))
39     filt = matlab_style_gauss2D()
40     conv = convolve2d(mf, filt, mode='same')
41     w_idx = conv > thres
42     bw = conv.copy()
43     bw[w_idx] = 1
44     bw[~w_idx] = 0
45     thresholded = np.multiply(bw, conv)
46     edg = 3
47     shape = data.shape
48     idx = np.nonzero(thresholded[edg-1: shape[0]-edg-1, \
49                           edg-1: shape[1]-edg-1])
50     idx = np.transpose(idx)
51     cent = []
52     for xy in idx:
53         x = xy[0]
54         y = xy[1]
55         if thresholded[x, y] >= thresholded[x-1, y-1] and \
56             thresholded[x, y] > thresholded[x-1, y] and \
57             thresholded[x, y] >= thresholded[x-1, y+1] and \
58             thresholded[x, y] > thresholded[x, y-1] and \
59             thresholded[x, y] > thresholded[x, y+1] and \
60             thresholded[x, y] >= thresholded[x+1, y-1] and \
61             thresholded[x, y] > thresholded[x+1, y] and \
62             thresholded[x, y] >= thresholded[x+1, y+1]:

```

```

63         cent.append(xy)
64     cent = np.asarray(cent).transpose()
65     return cent
66
67 def maxk(array, num_max):
68     array = np.asarray(array)
69     length = array.size
70     array = array.reshape((1, length))
71     idx = np.argsort(array)
72     idx2 = np.flip(idx)
73     return idx2[0, 0:num_max]
74
75 def gauss1(x,a,x0,sigma):
76     return a*exp(-(x-x0)**2/(2*sigma**2))
77
78 def track_spheres(img, mask, num_particles):
79     def gauss1(x,a,x0,sigma):
80         return a*exp(-(x-x0)**2/(2*sigma**2))
81     corr = normxcorr2(mask, img, mode='same')
82     cent = FastPeakFind(corr)
83     peaks = corr[cent[0], cent[1]]
84     ind = maxk(peaks, num_particles)
85     max_coor_tmp = cent[:, ind]
86     max_coor = max_coor_tmp.astype('float32')
87     pk_value = peaks[ind]
88     for num in range(0, num_particles):
89         x = max_coor_tmp[0, num]
90         y = max_coor_tmp[1, num]
91         fitx1 = np.asarray(range(x-7, x+8))
92         fity1 = np.asarray(corr[range(x-7, x+8), y])
93         popt, pcov = curve_fit(gauss1, fitx1, fity1, p0=[1, x, 3])
94         max_coor[0, num] = popt[1]
95         fitx2 = np.asarray(range(y-7, y+8))
96         fity2 = np.asarray(corr[x, range(y-7, y+8)])
97         popt, pcov = curve_fit(gauss1, fitx2, fity2, p0=[1, y, 3])
98         max_coor[1, num] = popt[1]
99     return max_coor, pk_value

```

---

## B.4 Fourier Transform Based Orientation Analysis

### B.4.1 Working Principle

The orientation of patterns in an image can be found by calculating the Fourier transform of the image. The idea is that in the direction of predominant pattern orientation (Fig. B.3a, the vertical direction), the signal frequency is smaller compared to the perpendicular direction. Such a feature manifests in the frequency domain as anisotropic patterns (Fig. B.3b, horizontal orientation). This method is used in the study of the emergence of active turbulence in Chap. 4.

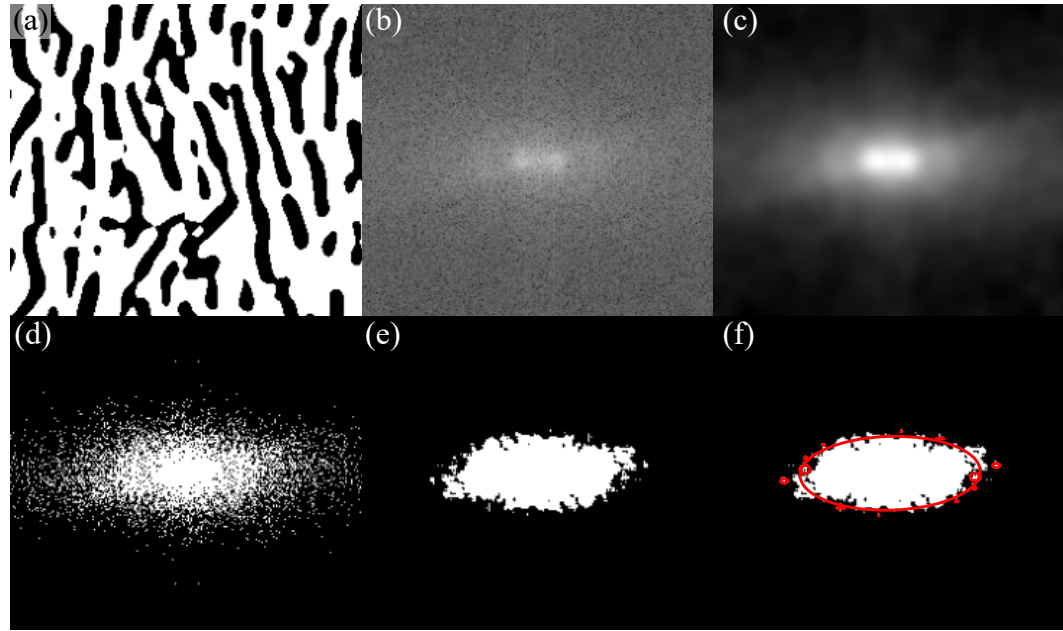


Figure B.3: **Fourier transform based orientation analysis illustration.** (a) Raw image. (b) Fourier transformed image. (c) Smoothing. (d) Binarization. (e) Despeckling. (f) Pattern detection.

The procedures are illustrated in Fig. B.3. We first perform Fourier transform on the raw image (Fig. B.3a), then smooth this transformed image (Fig. B.3b) using a

Gaussian filter to get Fig. B.3c, which is then binarized using a *isodata* threshold, yielding Fig. B.3d. A median filter is applied on the binarized image to remove small noise, known as despeckling, to obtain Fig. B.3e. Finally, we detect the anisotropic pattern in Fig. B.3e using a Python function `skimage.measure.regionprops`. Red circles in Fig. B.3f indicate all the patterns detected in the image, and we take the biggest one to examine the orientation. The Python implementation of these procedures is shown in Sec. B.4.2. Some example results are shown in Sec. B.4.3.

## B.4.2 Code

---

```

1  from skimage import measure, filters
2  import pandas as pd
3  from scipy.ndimage import gaussian_filter, median_filter
4
5  def sectionWindow(imgShape, windowShape):
6      Xnum = math.floor(imgShape[0]/windowShape[0])
7      Ynum = math.floor(imgShape[1]/windowShape[1])
8      Xrem = imgShape[0]%windowShape[0]
9      Yrem = imgShape[1]%windowShape[1]
10     Xstart = math.floor(Xrem/2)
11     Ystart = math.floor(Yrem/2)
12     Xend = imgShape[0] - Xstart + 1
13     Yend = imgShape[1] - Ystart + 1
14     X = np.asarray(range(Xstart, Xend, windowShape[0]))
15     Y = np.asarray(range(Ystart, Yend, windowShape[1]))
16     return X, Y
17
18 def getOrientation(bw_img):
19     label_img = measure.label(thres)
20     prop = measure.regionprops_table(label_img,
21                                     properties=['area', 'major_axis_length',
22                                                 'minor_axis_length', 'orientation'])
23     prop_df = pd.DataFrame(prop)
24     if len(prop_df) == 0:

```

```

25         return 0, 0
26     else:
27         main_feature = prop_df.sort_values(by='area', \
28                                         ascending=False).iloc[0]
29         return main_feature.orientation,
30                 main_feature.major_axis_length / \
31                 main_feature.minor_axis_length
32
33 # test code
34 windowShape = (50, 50)
35 img = io.imread(r'..\img\testFT_4.jpg', as_gray=True)
36 X, Y = sectionWindow(img.shape, windowShape)
37 y = X[0:X.size-1] + windowShape[0]/2
38 x = Y[0:Y.size-1] + windowShape[1]/2
39 x, y = np.meshgrid(x, y)
40 u_ori = x.copy()
41 v_ori = y.copy()
42 for i in range(0, x.shape[0]):
43     for j in range(0, y.shape[1]):
44         window = img[X[i]:X[i+1], Y[j]:Y[j+1]]
45         fft = np.log(abs(np.fft.fft2(window)))
46         fft = np.fft.fftshift(fft) ## 1
47         smooth = gaussian_filter(fft, 5) ## 2
48         thres = smooth > filters.threshold_isodata(smooth) ## 3
49         despeck = median_filter(thres, size=5) ## 4
50         ori, orim = getOrientation(despeck) ## 5
51         u_ori[i, j] = orim*math.cos(ori)
52         v_ori[i, j] = orim*math.sin(ori)
53
54 plt.figure(dpi=300)
55 plt.imshow(img, cmap='gray')
56 plt.quiver(x, y, u_ori, v_ori, color='red')
57 plt.axis('off')

```

---

#### B.4.3 Some Examples

Some example applications of this method are shown in Fig. B.4

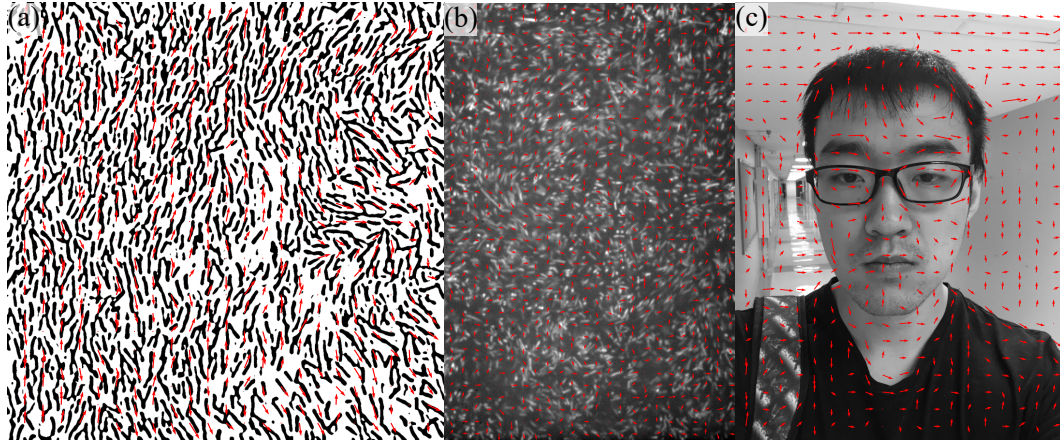


Figure B.4: **Fourier transform based orientation analysis examples.** Orientations of (a) a synthesized pattern, (b) an image of bacterial suspensions and (c) a photo of me.

## B.5 Density Fluctuation Calculations

The principles of density fluctuation calculation have already been described in Chap. 5. Here, I show the Python implementation of the calculation.

---

```

1 def df2(img_stack, boxsize=None, size_min=5, step=250):
2     """
3         Compute number fluctuations of an image stack.
4
5     Args:
6         img_stack -- a stack of image, a 3D array
7         boxsize -- the subsystem size to look at.
8         size_min -- the smallest box size
9         step -- step used when dividing image into windows
10
11    Returns:
12        df -- DataFrame of n and d,
13            where n is box area (px^2) and
14            d is total number fluctuations (box_area*dI)
15    """

```

```
16     L = min(img_stack.shape[1:3])
17     if boxsize == None:
18         boxsize = np.unique(np.floor(
19             np.logspace(np.log10(size_min), np.log10(L/2), 100)))
20
21     dI_list = []
22     for bs in boxsize:
23         I = divide_stack(img_stack, winsize=[bs, bs], step=step)
24         dI = I.std(axis=0).mean() * bs ** 2
25         dI_list.append(dI)
26
27     return pd.DataFrame({'n': np.array(boxsize)**2, 'd': dI_list})
```

---